5-2018

Evolution of Non-collinear Magnetic Structures via Material Engineering Revealed by Neutron Scattering

Ryan Patrick Rawl
University of Tennessee, wzc524@vols.utk.edu

To the Graduate Council:

I am submitting herewith a dissertation written by Ryan Patrick Rawl entitled "Evolution of Non-collinear Magnetic Structures via Material Engineering Revealed by Neutron Scattering." I have examined the final electronic copy of this dissertation for form and content and recommend that it be accepted in partial fulfillment of the requirements for the degree of Doctor of Philosophy, with a major in Physics.

Haidong Zhou, Major Professor

We have read this dissertation and recommend its acceptance:

Takeshi Egami, Steven S. Johnston, Jian Liu

Accepted for the Council:
Dixie L. Thompson

Vice Provost and Dean of the Graduate School

(Original signatures are on file with official student records.)

Evolution of Non-collinear Magnetic Structures via Material Engineering Revealed by Neutron Scattering

A Dissertation Presented for the

Doctor of Philosophy

Degree

The University of Tennessee, Knoxville

Ryan Patrick Rawl

May 2018

This dissertation is in dedication to my mother, Janet.

Acknowledgments

I would like to thank my advisor, Haidong Zhou, for his guidance and advice during my tenure. His instruction has been instrumental in my growth from a student to a published researcher. Thanks to his oversight, I have grown into a scientist capable of independent research.

The work undertaken for this dissertation involved the contributions and collaborations of many talented scientists. I would like to extend thanks to Minseong Lee, Eun Sang Choi, Kuan-Wen Chen, Ryan Baumbach, Harish Agrawal, Yoshimoto Kamiya, Nicholas P. Butch, Xuefeng Sun, Cristian Batista, Huibo Cao and Martin Mourigal for all of their contributions in both experimental and theoretical aspects of the research. I want to place special recognition of Luwei Ge for his assistance in the simulation of inelastic neutron diffraction data and Jaan Oitmaa for allowing us to use his high-temperature series expansion coefficients.

During the research performed for this dissertation, I have performed experiments at different national laboratories. I would like to recognize all of the local staff and contacts at Los Alamos National Laboratory and Oak Ridge National Laboratory. I would especially like to thank Vivien Zapf and Xiaxin Ding for their hosting at Los Alamos and Stuart Calder at Oak Ridge. For her thoughtful mentorship and hosting me during the Department of Energy Office of Science Graduate Student Research program, I thank Clarina dela Cruz.

I would like to thank Prof. Steve Johnston, Prof. Takeshi Egami, and Prof. Jian Liu from the University of Tennessee for being on my doctoral committee and their feedback. I would also like to thank Prof. Cristian Batista for his advice and collaboration.

I would like to think the other members of my research group, Ryan Sinclair, Zhiling Dun, Jie Ma, Qiang Chen, and Qing Huang. Their assistance throughout the years has been instrumental in my learning.

I would like to thank the National Science Foundation and Department of Energy Office of Science Graduate Student Research Program for funding support of my research.

Finally, I would like to thank my family for their support in all aspects of my life. I would like to thank my parents for their advice and love. I also would like to thank my brother for his contributions to my learning.

Abstract

Neutron scattering is a powerful tool for revealing magnetic structures of both single crystal and powder materials. By combining neutron scattering with other measurements such as AC and DC susceptibility, magnetization, specific heat, and resistivity, it is possible to unearth the magnetic properties of many materials. Neutron scattering is especially useful in the examination of geometrically frustrated materials, where the competition between interactions can yield a variety of interesting magnetic ground states. For complex or incommensurate structures, single crystal neutron diffraction is a powerful tool able to resolve intricacies not possible with powder measurements. Here, neutron scattering techniques are examined and used in combination with other measurements to examine two-dimensional frustrated triangular compounds and 3d-transition metal monophosphides with a double helical structure.

Table of Contents

List of Tables

List of Figures

Chapter 1

Introduction

With electron interactions governing the bulk properties of the materials we encounter, understanding their base behaviors has long been a focus of condensed matter physics. Of particular interest over the years due to unique phenomena are magnetic ordering and their subsequent behavior. Here, the magnetic properties of non-collinear magnetic structures are examined using neutron scattering and supplementary techniques. The evolution of these structures under chemical substitution is examined to probe the fundamental physics underlying both frustrated triangular and double helical magnetic structures. In this chapter, the measurement techniques, accompanying concepts used, materials examined, and sample growth by chemical vapor transport are briefly introduced.

1.1 Scattering measurements

Underlying the understanding of solids is a thorough knowledge of the crystalline structure. While imaging techniques can be an ideal measurement to identify indexed locations, the practical limits at small lengths scales make it impractical in many cases. Long-range ordering (LRO) can be observed by making use of scattering of incoming plane waves against a periodic array and observing the constructive and destructive interference produced. In the scattered beam, a path length difference of $n\lambda$ will interfere constructively and form Bragg reflections. In an ordered crystal, these Bragg reflections are used to probe interlayer distance, d, in the crystal by the relationship $2d\sin\theta = n\lambda$, where θ is the angle

of the observed Bragg reflection, n is an integer, and λ is the wavelength of the diffracting wave. As interatomic, and thus interlayer, distances in solid state materials are of the order of Ångströms, similar wavelengths are most useful for scattering measurements. X-ray, neutron, and electron diffraction are all common practices to probe long-ranged order due to their readily available comparable wavelengths.

1.2 Determining Magnetic Properties

Some of the most historically interesting and functionally useful properties of materials are their magnetic properties. From the compass to high-density information storage, magnetic properties have been both economically and scientifically prominent. The most fundamental split of materials is into paramagnetic (magnetizes along the direction of the field, no remnant magnetization), diamagnetic (magnetizes against the direction of the field, no remnant magnetization), ferro- and ferrimagnetic (magnetizes along the field, holds remnant magnetization), and antiferromagnetic (no bulk magnetization). These can be distinguished by a simple measurement of magnetization in a field sweep. For a microscopic view, magnetic properties are governed by the magnetic Hamiltonian, the operator corresponding to the total energy of the electrons in the system. From a known Hamiltonian, properties such as specific heat, susceptibility, magnetization, electronic band structure, resistivity, and fundamental excitations can be calculated. Thus, an accurate description of the magnetic Hamiltonian is the ultimate goal of magnetic property measurements. To this end, the ground state of the magnetic structure is one of the pivotal pieces of information and is the focus of much of this manuscript. Further detail on measurement techniques used to determine magnetic properties is presented in Chapters 2 and 3.

1.2.1 Neutron measurements

Neutron scattering measurements are powerful tools to examine the magnetic ground state and excitations in materials in addition to examining the structure and structural excitations in a nondestructive manner. This makes neutron scattering measurements

especially useful in revealing the material's Hamiltonian as symmetry is a fundamental determining factor in both the ground state and excitations. Neutrons have a mass of 1.6605×10^{-27} kg, meaning that the typical wavelengths for scattering of 1-10 Å correspond to an energy range of approximately 1-100 meV. Magnetic excitations tend to fall in this energy range, further reinforcing the usefulness of neutrons. Neutron scattering occurs following Bragg's Law with the neutrons scattering off of nuclei and electron spins. The scattering off of the nuclei is essentially classical, while the scattering off of electron spins involves a spin flip of both the electron's and the neutron's spin-1/2 moments. Elastic scattering techniques reveal the positions and related parameters of the nuclei and spin while inelastic scattering techniques probe the energy dependence of the excitations at different momentum transfer values. These can be used to model the Hamiltonian of the materials.

1.2.2 Other Techniques

While neutron scattering can determine magnetic structures, it is a time-consuming endeavor that requires powerful neutron sources. Due to small neutron scattering cross sections, a large flux of neutrons is imperative to get useful data on magnetic ordering and experiments tend to run on the order of hours to days. To probe magnetic behavior under changing conditions, supplementing neutron scattering measurements with other techniques can provide an understanding of the underlying magnetic phenomena. Some of the most common uses are for finding the temperatures, fields, or pressures where materials undergo a structural or magnetic phase transition. Measurements such as susceptibility, magnetization, specific heat, and resistivity can be modeled via a Hamiltonian and thus can provide both complementary and supplementary magnetic data. In this manuscript, these techniques are used in conjunction with neutron scattering to provide magnetic phase information.

1.3 Non-collinear Magnetic Orders

Both ferromagnetic (FM) and antiferromagnetic (AFM) order tends to favor collinear arrangement of the spins due to their energetic favoring of parallel and antiparallel ordering respectively. Thus, a fundamental difference in the underlying magnetic ground state is

necessarily present to produce non-collinear magnetic order. While fundamental magnetic excitations, spin waves, disturb the linear ordering of the ground state, the stabilization of a non-collinear state is only found when there is some form of frustration of the spin interactions. Frustration is the inability for all interactions to be energetically minimized simultaneously. This can occur from a balance of the interactions due to the underlying geometry or the strengths of competing interactions. A square lattice with nearest neighbor interactions of J and next nearest neighbor interactions of $-J$ will be frustrated due to their exact energy difference for any spin orientation, thus further interactions will be responsible for any stabilization of the magnetic ground state. Non-collinear order often arises from frustration, while easy-axis or easy-plane anisotropy are another source of deviation from collinear orders.

1.3.1 Geometrically Frustrated Magnets

Geometrical frustration often occurs due to the underlying structural symmetry of the interactions. For a simple case, an Ising spin system with AFM interactions is not frustrated in the bipartite square lattice Figure 1.1(a)) where all spins can align antiparallel. However, an Ising spin on a triangle with AFM interactions is inherently frustrated. For two vertices to be antiparallel, the third vertex cannot simultaneously be antiparallel to both (Figure 1.1(b)). For AFM Ising spins, geometric frustration occurs in triangular, tetrahedral, face-centered cubic, hexagonal-close-packed, pyrochlore, and Kagome lattices (examples in Figure 1.2). For easy-axis FM interactions on a tetrahedron, the competition between the FM interaction and the single ion, easy-axis anisotropy is the cause of the frustration. In this manuscript, triangular lattice antiferromagnetic materials are examined due to their frustrated nature. The result of frustration can be exotic ground states including spin liquid, spin ice, non-collinear ground states, and fractional gauge fields [1, 2, 3]. Triangular lattice magnets can have their frustration reduced by a multitude of perturbations, including interplane interactions or anisotropy. For a true two-dimensional (2D) magnet, the magnetic ordering temperature will increase logarithmically in magnitude of both the interplane interactions and anisotropy [4, 5, 6, 7, 8]. As a result, reducing both of these parameters to near zero is an essential step in isolating the two-dimensional magnetic behavior of the triangular lattice.

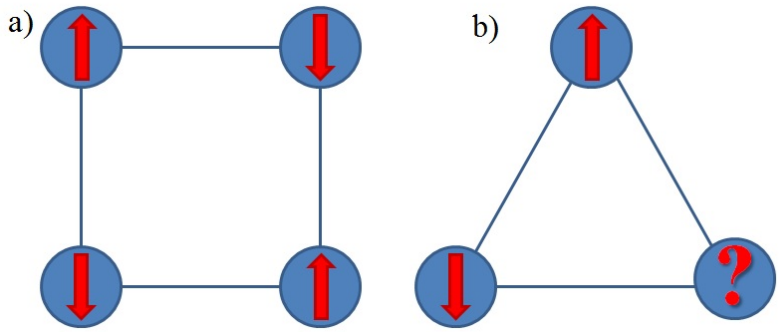

Figure 1.1: Antiferromagnetic ising nearest neighbor interactions resulting in a) Neel ordering on the unfrustrated square lattice and b) geometrical frustration on the triangular lattice.

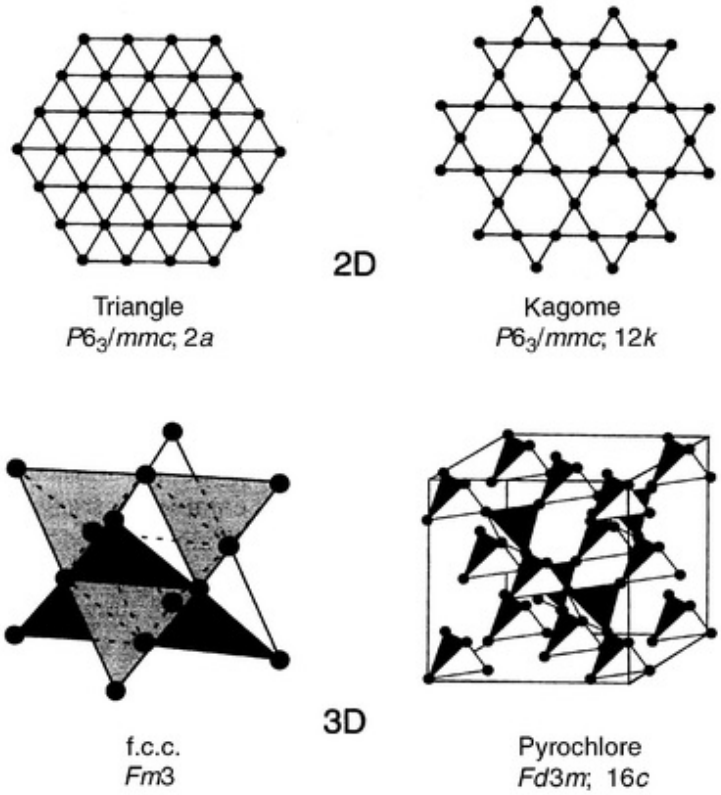

Figure 1.2: Examples of geometrically frustrated lattices. For antiferromagnetic interactions, triangular, Kagome, face-centered cubic, and pyrochlore lattices are all frustrated. Ferromagnetic interactions with single ion, easy-axis anisotropy on a lattice of tetrahedra, such as the face-centered cubic and pyrochlore lattices, also result in geometric frustration [3].

While the local anisotropy is difficult to predict and control, the reduction of interplane interactions can be more efficiently realized. To this end, we used the approach of introducing non-magnetic layers between triangular layers of magnetic ions. This led to small values in the interplane coupling of the observed materials. Anisotropy effects were seen in some materials while not in others examined. Combining these, we observed both quasi-2D and effective true-2D behavior in triangular lattice magnets.

One of the most promising and potentially fruitful areas of frustrated systems is in quantum spin liquids (QSLs). In a QSL, quantum fluctuations prevent the system's spin structure from reaching a unique ground state [3, 9, 10]. Much of the attention on QSLs centers around the exotic phenomena resulting from their degenerate ground states, such as proposed superconducting states, emergent gauge fields (monopoles), and fractional particle excitations [2]. The quantum fluctuations are of the order of the spin moment themselves in spin-1/2 systems and the various ground states can be accessed by the zero point motion. This resonating valence bond (RVB) state was coined in 1973 by Anderson [11] and has been studied extensively in the intervening years. Despite the spins being highly correlated, quantum fluctuations persist down to absolute zero and cause the ground state to form a superposition of the degenerate ground states. The resonating bonds allow for a spin flip to move fluidly by a rearrangement of the bonds into another degenerate ground state instead of maintaining a rigid order (Figure 1.3) [2].

The condensed matter community has shown much interest in 2D triangular lattice magnets (TLMs) as they host a multitude of different ground states [12, 13, 14]. In $Ba_3CoSb_2O_9$ with Co^{2+} (effective spin-1/2) ions residing on triangular lattices, the ground state is a 120 degree ordered state at zero field and an up-up-down (*uud*) phase under applied field [15, 16, 17, 18] (see Figure 1.4). The spin wave spectra for $Ba_3CoSb_2O_9$ can be reasonably described by an XXZ model with small easy-plane anisotropy. However, linear and nonlinear spin wave theories do not pick up the abnormal magnon decay and line broadening that result from the quantum spin fluctuations [19]. In isostructural $Ba_3BNb_2O_9$ (B = Co [20], Ni [21], Mn [22]) as well as $CuCrO_2$ [23, 24] and $RbFe(MoO_4)_2$ [25, 26], multiferroic properties are seen in the 120 degree ordered ground state. Alternatively, $AAg_2M(VO_4)_2$ (A = Ba, Sr; M = Co, Ni) [27, 28] possesses a FM ordering due to the

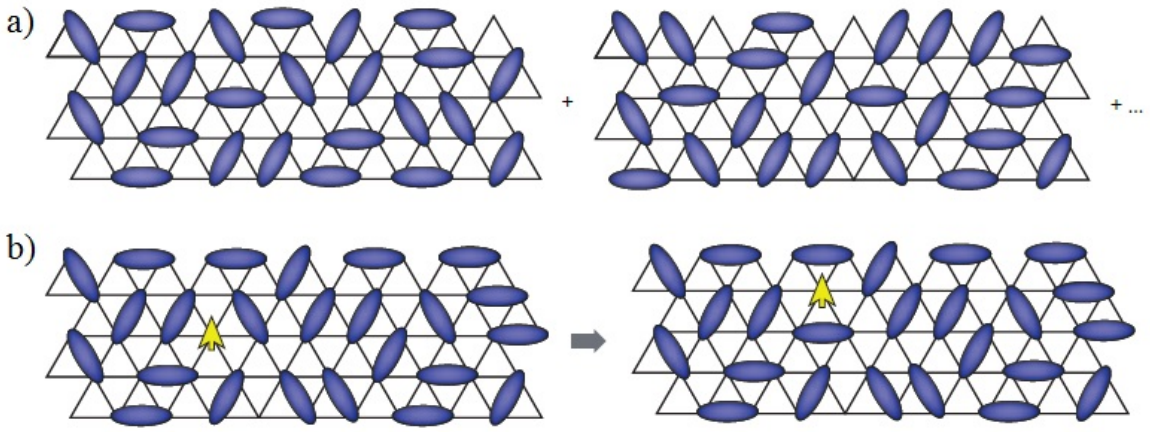

Figure 1.3: a) The ground state of a quantum spin liquid as a superposition of possible orientation of the short ranged singlet bonds. b) A spin flip excitation is able to move without energy cost in a spin liquid. This is accomplished by rearranging the valence bonds in a ground state configuration [2].

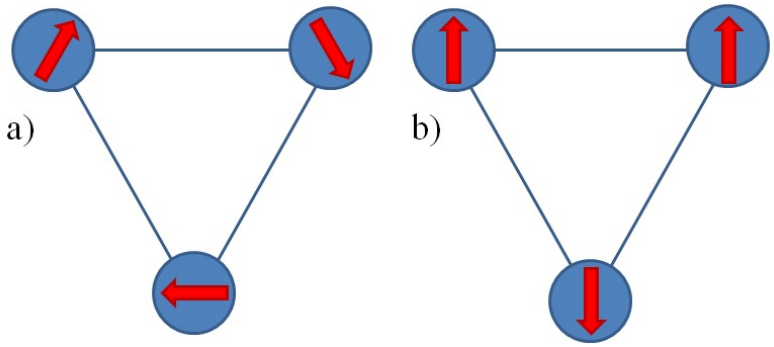

Figure 1.4: a) 120 degree ground state for triangular lattice antiferromagnets and b) up-up-down phase of a purely quantum nature. The up up down state is often manifest as a magnetization plateau under increasing fields for low spin, triangular compounds.

superexchange via the bridging vanadates on the triangular lattice. A collinear alternating striped AFM state related to strong easy axis anisotropy is manifest in this family of $AAg_2M(VO_4)_2$. In $NaVO_2$ [29, 30], rare ordering of the V^{3+} orbitals is seen. LRO occurs as a consequence of the ordering of the V^{3+} orbitals relieving the geometrical frustration. More recently, and holding much promise, the exotic QSL ground state was realized in $YbMgGaO_4$ [31, 32, 33, 34]. The effective spin-1/2 Yb^{3+} ions reside on a triangular lattice and both the spin anisotropy and next-nearest neighbor interactions are vital.

1.3.2 Double Helical Structures

While geometrically frustrated systems have an obvious cause for the non-collinear ordering, in the 3d-transition metal pnictides (3dTMPs) it is common to observe a double helical magnetic structure. Double helical magnetic structures have been reported in MnP, CrAs, FeP, and FeAs [35] with modulation of the magnetic structure varying between the samples. FeP has been shown to be a bunched helix [36], MnP and CrAs are reported as circular helixes [37, 38], and FeAs is a non-collinear spin-density wave [39]. The relation between the chemical composition and the magnetic structure has not been thoroughly examined and doping between end members is a natural progression to explore the evolution of the magnetic ordering of the double helical structure. Making use of FeP and MnP both having a double helical structure while MnP has an additional FM transition, a complete magnetic phase diagram of the $Fe_{1-x}Mn_xP$ is examined in this manuscript.

1.4 Chemical Vapor Transport

One of the primary driving forces for improvement in experimental condensed matter physics is the improvement in sample quality resulting from improved growth methods. While there are a variety of ways to grow single crystals, some methods have been almost entirely replaced. The well-known growth of single crystals by supersaturation posses many problems in controlling the crystal growth and has been superseded by methods such as flux, floating zone, thin film vapor deposition, and chemical vapor transport (CVT). Each method has both benefits and limitations. Flux reactions generally require little supervision, but the

compounds able to be grown by flux are limited by an appropriate phase diagram and a method to extract the grown crystals from the surrounding flux. Floating zone growths is a rapid way to grow very large crystals, but growth requires careful monitoring and the selection of compounds that can be grown this way are limited. Thin film vapor deposition allows for fine control over layer thickness to examine finite sized effects but is not practical for production of bulk samples. CVT is robust in that it is resistant to impurities, whether chemical or phase, but is limited due to the interconnected processes involved. All elements must be transported in gaseous form, whether as elements or part of a compound, by the same transport agent and temperature gradient. While the somewhat limited scope caused by these limitations prevents CVT from being used in all cases, the sample quality produced is arguably unsurpassed by any other bulk methods. This is especially useful in the growth of doped compounds where high crystal purity is imperative, as in doped superconductors.

The high crystal quality produced by CVT is a result of the robust mechanisms underpinning the growth. In CVT, all of the crystal's elements are required to be converted into a gaseous phase such that these elements can deposit over time to create bulk single crystals. By controlling the growth rate, it is possible to grow large, single domain crystals. The simplest example of such a method would be sublimation and deposition. Picking the endothermic case, a solid is placed under a temperature gradient where the source is sublimated at the hot end, translates down the tube, and deposits the seed at the cold end. Crystal growth then occurs when the partial pressures of the constituent elements are sufficient and the temperature is low enough (high enough for exothermic reactions) for the reverse process. After the seeding of nanoparticles, it is energetically favorable for deposition to occur on these nanoparticles over the vessel walls. A slightly more involved example is decomposition, where a compound breaks down into elements or simpler compounds that are then deposited as separate single crystals.

Transport methods of growth are generally referred to as those in which the solvent is involved in the creation of the gaseous phase(s) of the constituent elements. Generically, the provided heat will sublimate the transport into a gaseous phase that will then dissolve part or all of the elements and compounds found in the source material. If there are remaining elements or compounds after the removal of this solute, they then are heated into the gaseous

phase as well. After sufficient partial pressures have developed at the seed end, there is a reversal of this process in which single crystals of the desired composition are deposited and the remaining solvent, and any unwanted source elements if any, are separately deposited. This process is summarized in Figure 1.5. While the crystal quality is robust, there are various factors that must be considered for successful growth. Once such consideration is the transport agent for the investigated system must be sufficient to transport all required elements to the seed end. In the 3dTMPs, FeP, CoP, and MnP, are all readily transported by iodine. The second consideration is the endothermic or exothermic nature of the reaction and the accompanying temperature gradient. For the mentioned 3dTMPs, FeP and CoP dissolution is endothermic while MnP dissolution is exothermic. As a result, only $Fe_{1-x}Co_xP$ doped single crystals have been successfully synthesized by us. A third consideration is that the deposition process must be able to occur faster than the sublimation process. Once these factors are considered, CVT is a method that offers the potential for very pure crystal quality.

With this in mind, CVT reactions have been very successful in our research. We have successfully synthesized a variety of different structure compounds both for our own research and in collaboration with other researchers (Figure 1.6). Of the crystals we have grown, pure and single domain crystals have been obtained for the following:10 mm^3 FeP and MnP, 1 mm^3 CoP, $Fe_{1-x}Co_xP$, and FeS, 15 mm^3 iron-yttrium garnet, 10 mm^3 Ni_2InSbO_6, and both 10 mm^2 monolayers and 1 mm^3 bulk $MnPS_3$.

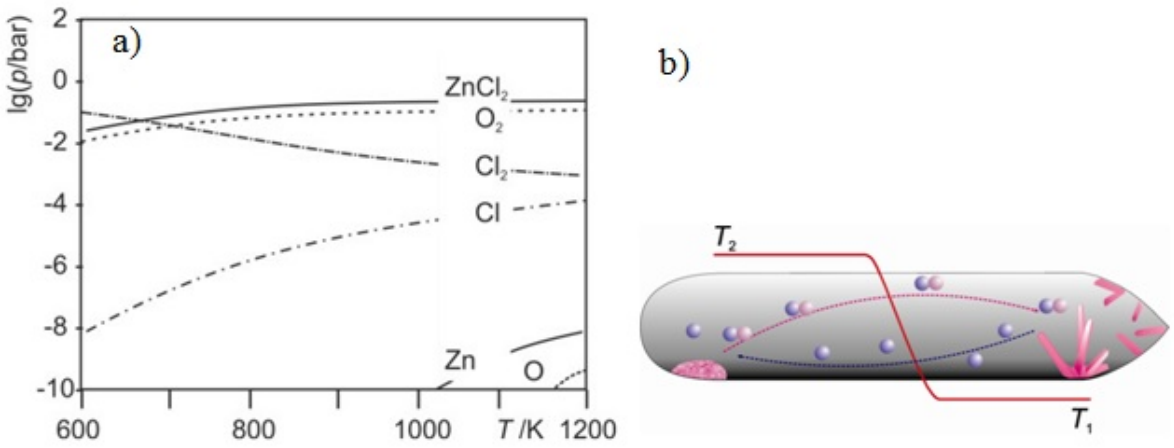

Figure 1.5: Here [40], a) the partial pressures as a function of temperature for ZnO transport by Cl_2 is shown. The partial pressures for Zn and O elemental gas by simple sublimation decomposition is insufficient for reasonable crystal growth. By introducing Cl_2 gas, Zn is dissolved as $ZnCl_2$ will gaseous O_2 is also released. The partial pressures remain sufficient to lower temperature gradients, where the endothermic nature of forming $ZnCl_2$ will cause the process to reverse, producing single domain crystals of ZnO. B) A simplified model of transport and deposition is shown.

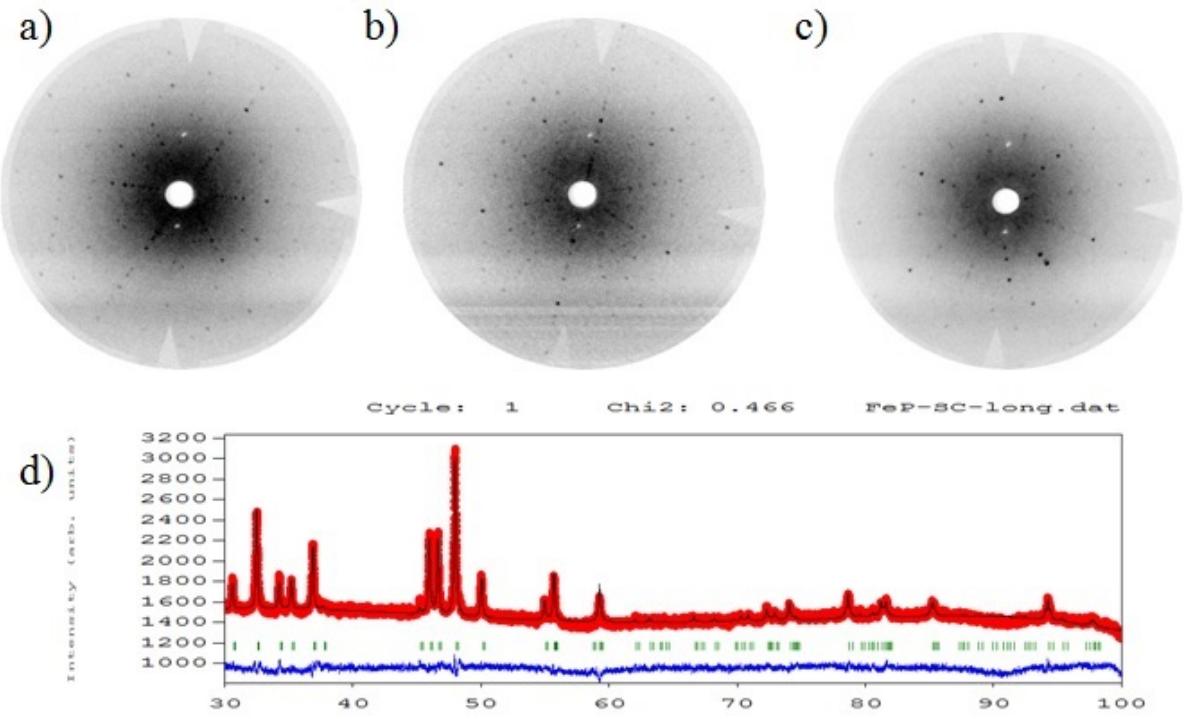

Figure 1.6: Laue diffraction images of a) FeP, b) MnP, and c) $MnPS_3$. d) X-ray diffraction refinement of samples grown using chemical vapor transport.

Chapter 2

Neutron Diffraction

Explanation of macroscopic properties of materials via theoretical condensed matter physics relies on an understanding of the structure of the underlying atoms. Due to the Ångström scale interatomic distances, a comparable wavelength is needed to probe these distances with accuracy. X-ray diffraction is a powerful tool for such measurements, but has some fundamental limitations. X-rays interact with the relatively large electron cloud and thus have limited penetrating power, limiting sample environments. Additionally, X-ray scattering cross sections are determined by the size of the electron cloud and do not vary strongly for most similar atomic number atoms. In contrast, neutrons interact via nuclear forces and are deeply penetrating (Figure 2.1) and thus able to probe samples through a variety of containers. This also results in a differing cross section for atomic isotopes and also a strongly varying cross section with atomic number. This is very useful for resolving the atomic orderings of materials. Some neutron scattering cross sections, such as hydrogen, are negative. This allows for such methods as contrast matching in certain samples by doping hydrogen containing samples with deuterium to examine only certain components of a system. As a trade-off, the low intensity of scattering of incoming neutrons limits resolution as does available neutron flux, as even the most powerful neutron sources are orders of magnitude weaker in flux than common X-ray sources. However, the presence of a magnetic moment on the neutron allows it to interact with unpaired spins and scatter off of them in addition to the nuclei. This is useful in determining the magnetic structure of these spins. The spin of the neutron allows it to undergo spin flip interactions, allowing for the

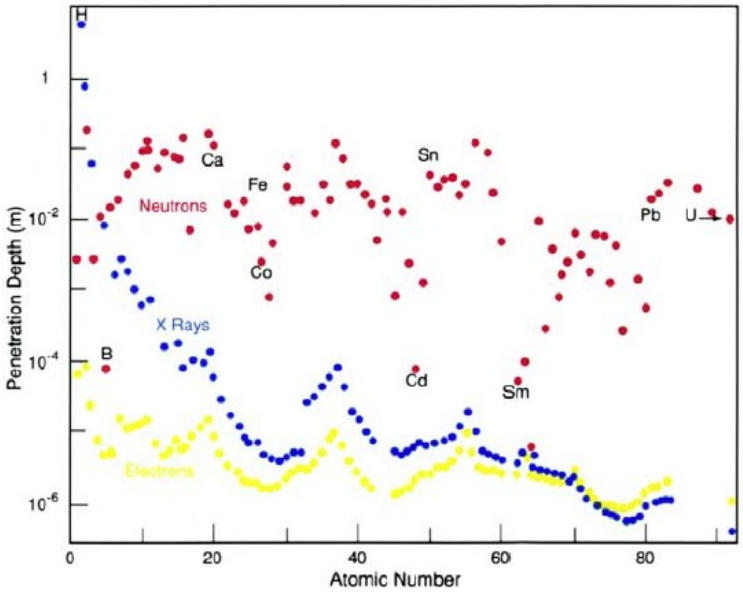

Figure 2.1: Penetration depth of neutrons (red), X-rays (blue) and electrons (yellow) before the intensity has decreased by a factor of $1/e$ for various elements. [41]

distinction between interactions such as magnetization of the sample being perpendicular or parallel to the neutron moment.

Neutron scattering makes use of interference between scattered neutrons based off of the location of the scattering nucleus. For a periodic array of nuclei, maxima will be located at path length differences of $n2\pi$. For a distance between planes of d and a scattering angle of θ, this leads to Braggs Law of $n\lambda = d\sin\theta$ as diagramed in Figure 2.2.

For neutrons, it is more helpful to think in terms of momentum $\boldsymbol{k}$ with $\boldsymbol{k} = 2\pi m\boldsymbol{v}/h$, where m is the neutron mass, $\boldsymbol{v}$ the velocity, and h is Planck's constant. During a collision, it is easy to be seen from Figure 2.2 that the momentum transfer is equal to $h\boldsymbol{Q}/2\pi = h(\boldsymbol{k} - \boldsymbol{k'})/2\pi$ where $\boldsymbol{Q}$ is known as the scattering vector. For elastic scattering, with no energy transfer and thus $|\boldsymbol{k}| = |\boldsymbol{k'}|$, this yields $|\boldsymbol{Q}| = 4\pi\sin(\theta/\lambda)$. Including possible energy transfer complicates the calculations, but, by making use of the Born approximation, Van Hove was able to show that the intensity of scattering as a function of $\boldsymbol{Q}$ and energy, E, could be given by

$$I(\boldsymbol{Q}.E) = \frac{1}{h}\frac{k'}{k}\sum_{i,j} b_i b_j \int_{-\infty}^{\infty} \left\langle e^{-i\boldsymbol{Q}\cdot\boldsymbol{r_i}(0)} e^{-i\boldsymbol{Q}\cdot\boldsymbol{r_j}(t)} \right\rangle e^{i-(E/\hbar)t} dt, \tag{2.1}$$

where b is the scattering length of the nuclei, i and j are position labels such that nucleus j is at r_j at time t, and the angled brackets indicate a thermodynamic average over the thermal fluctuations of the sample. Since the nuclear spin is generally decoupled from the position of the nucleus, Equation 2.1 can be written more generally as

$$I(\boldsymbol{Q}.E) = \sum_{i,j} \langle b_i b_j \rangle A_{ij} = \sum_{i,j} \langle b \rangle^2 A_{ij} + \sum_i \left(\langle b^2 \rangle - \langle b \rangle^2 \right) A_{ii}, \tag{2.2}$$

where A_{ij} represents the integral in Equation 2.1. In this representation, the first term represents coherent scattering of neutrons off of separate nuclei and interfere as shown in Figure 2.2. The second term represents incoherent scattering, where the scattering results as a sum of events from non-interfering scattered neutrons. For elastic scattering, the coherent scattering provides information about the atomic structure while the inelastic scattering provides information about excitations of the nuclei or unpaired spin.

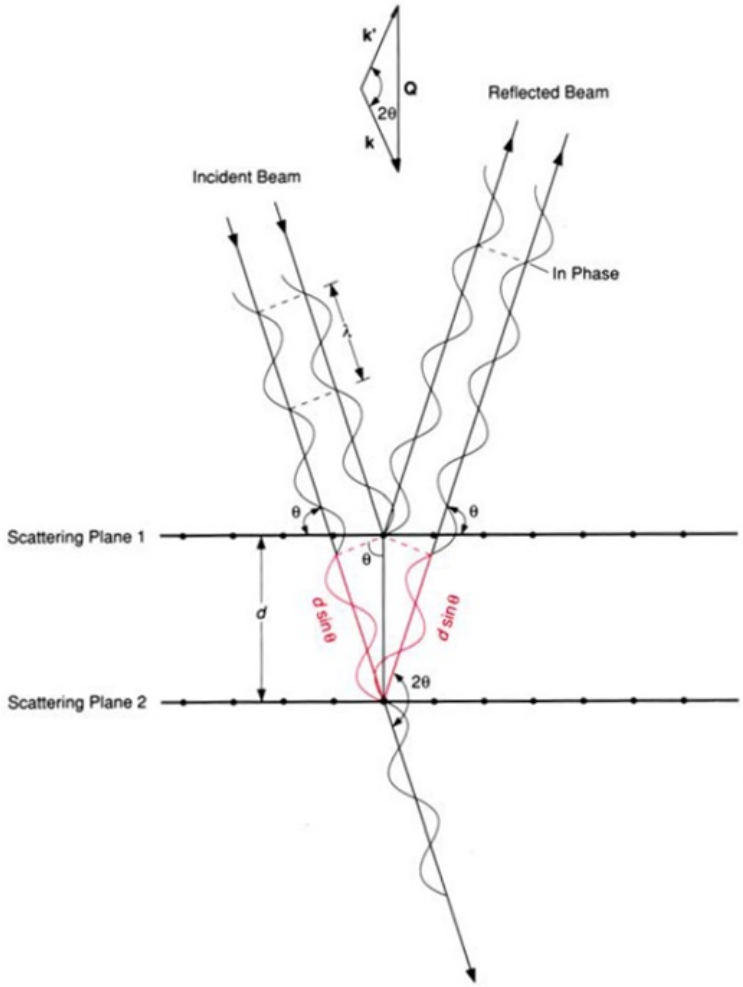

Figure 2.2: Diagram of Bragg diffraction [41]. The wavelength, λ, separation between scattering planes, d, and scattering angle, θ, determine the difference in path length between scattering events. When this difference is a multiple of 2π, constructive interference occurs and a Bragg reflection is seen. This is Bragg's Law of $n\lambda = d\sin\theta$.

2.1 Single Crystal Diffraction

Perhaps the most straightforward, yet one of the most useful for determining atomic structure, forms of coherent scattering is single crystal (SC) diffraction. As the nuclei form a three dimensional (3D) periodic array, the resulting diffraction pattern will produce diffraction spots as described originally by Laue [42]. These equations are given as $\boldsymbol{a} \cdot \Delta\boldsymbol{k} = 2\pi h, \boldsymbol{b} \cdot \Delta\boldsymbol{k} = 2\pi k, \boldsymbol{c} \cdot \Delta\boldsymbol{k} = 2\pi l$, where $\boldsymbol{a}, \boldsymbol{b}, \boldsymbol{c}$ are primitive lattice vectors and h, k, l are Miller indices that must take integer values. For elastic scattering, the possible scattering nuclei are those that intersect what is known as the Ewald Sphere. This is a trace of length $|\boldsymbol{k}| = |\boldsymbol{k'}|$ in reciprocal space. It follows that for a reciprocal lattice vector $\boldsymbol{G}$, where $\boldsymbol{G} \cdot (\boldsymbol{a} + \boldsymbol{b} + \boldsymbol{c}) = 2\pi(h + k + l)$, then $\Delta\boldsymbol{k} = \boldsymbol{G}$. This rearranges into $2\boldsymbol{k_i} \cdot \boldsymbol{G} = G^2$ and consequently back to Bragg's Law of $n\lambda = 2d\sin\theta$. The resulting pattern provides information on the symmetry and cell parameters of the sample.

2.1.1 Background

While the majority of the scattering process is elastic, many neutron detectors measure scattered neutrons of all energies. Including this energy integral in the Van Hove formalism results in evaluating the correlation function at time equal to zero. For a single isotope system, this results in

$$I(\boldsymbol{Q}.E) = b_{coh}^2 \sum_{i,j} \left\langle e^{-i\boldsymbol{Q}\cdot(\boldsymbol{r_i}-\boldsymbol{r_j})} \right\rangle, \tag{2.3}$$

For samples at zero temperature, nuclear positions would be stationary and the thermodynamic average could be discarded. If the atoms are instead allowed to oscillate about their equilibrium position, the scattering intensity becomes

$$I(\boldsymbol{Q}.E) = b_{coh}^2 \sum_{i,j} e^{-i\boldsymbol{Q}\cdot(\boldsymbol{r_i}-\boldsymbol{r_j})} e^{-Q^2\langle u^2\rangle/2} = \left| b_{coh} \sum_{i} e^{i\boldsymbol{Q}\cdot\boldsymbol{r_i}} \right|^2 e^{-Q^2\langle u^2\rangle/2} \equiv S(\boldsymbol{Q}), \tag{2.4}$$

where S($\boldsymbol{Q}$) is the structure factor and $e^{-Q^2\langle u^2\rangle/2}$ is the Debye-Waller factor in which $\langle u^2\rangle$ is the average of the squared displacements of the atomic nuclei. For non-zero values of $S(\boldsymbol{Q}), \boldsymbol{Q}\cdot(\boldsymbol{r_i}-\boldsymbol{r_j})$ must be multiples of 2π, indicating that $\boldsymbol{Q}$ is also a reciprocal lattice vector. This represents parallel planes of atoms, recovering neatly Bragg's Law from before, despite no longer requiring only elastic scattering.

2.1.2 Data and Refinement

Single crystal data used in this thesis was taken at the HB-3A four-circle diffractometer (schematic shown in Figure 2.3) located at the High Flux Isotope Reactor (HFIR) at the Oak Ridge National Laboratory (ORNL). This diffractometer can examine scattering angles for $-27^\circ < 2\theta < 160^\circ$ with a neutron flux of up to 2.2×10^7 n/cm^2/s. A monochromator of silicon creates reflections of 1.005, 1.546, and 2.541 Å using the (011), (022), and (111) planes. Using a 2D scintillator-based detector, 2D images of each diffraction peak are taken. By rotating the sample and camera location, scans in h, k, and l are easily obtained. The data is converted into an integrated intensity file using a fitting of a Gaussian function ($\exp(-\frac{4\ln 2}{\mathrm{FWHM}^2}x^2)$) and a linear background via a python script in MantidPlot [43]. This provides a list of relative intensities for each reflection that can then be used to refine the magnetic structure using the Rietveld method in Fullprof [44].

Rietveld refinement is a powerful tool for determining magnetic and atomic structures of various diffraction patterns. Rietveld refinement works by minimizing the function

$$M = \sum_i W_i \Big\{ y_i^{obs} - \frac{1}{c} y_i^{calc} \Big\}^2, \tag{2.5}$$

where W_i is a statistical weight, y_i is the intensity of peak i, and c is an overall scale factor. Due to the integration of the peak intensities for the data taken at HB-3A, this means that the shape of the peak does not have to be matched and factors such as asymmetry do not affect the refinement. The nuclear structure can be refined from these integrated intensities using an established symmetry group. The magnetic structure can be refined by subtracting the integrated intensities in the paramagnetic phase from those in the ordered phase, leaving only the intensities of the magnetic structure. These can be solved with a magnetic propagation

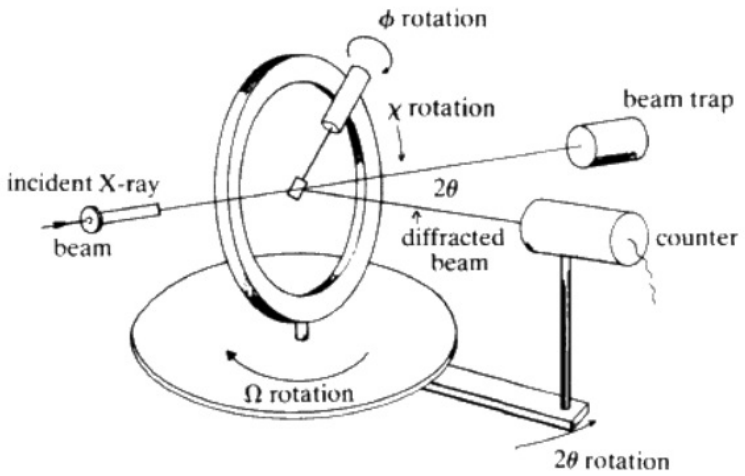

Figure 2.3: Schematic diagram of a four-circle diffractometer, such as the HB-3A, showing that by rotating the sample and detector a scan of reciprocal space is possible. Image courtesy of the International Union of Crystallography [45].

vector, often called the k-vector due to being defined in reciprocal space but is distinct from the momentum of the incoming and outgoing neutrons. This represents how the magnetic structure is modulated and, when converted back into real space, will describe over how many unit cells in each direction the magnetic structure repeats. The magnetic propagation vector can be found by locating the magnetic reflections in relation to nuclear reflections. Magnetic reflections will be located at allowed values of $(h + \delta h, k + \delta k, l + \delta l)$ where the h, k, and l are integers along the a-, b-, and c-axes respectively and the k-vector is defined as $(\delta h, \delta k, \delta l)$. Magnetic reflections for FM ordering will have a k-vector of (0, 0, 0) and occur at the same location as the nuclear peaks while AFM ordering will produce magnetic reflections shifted off of the nuclear peak. By scanning the appropriate hkl space, the AFM peaks will be included in the integration of the intensities so that any overlap with nuclear peaks can be subtracted out.

Our refinements in this thesis were performed using the FullPROF software suite [44], which allows for modeling of the magnetic structure using either basis vectors determined from the space group and k-vector or by controlling the magnetic moments individually. This allows for control of the magnetic structure using the space group from the k-vector as well as the freedom to refine individual magnetic moments separately. Due to measuring the reflections with respect to the sample orientation, anisotropic effects can be examined and complex magnetic structures can be resolved, such as bunched helical versus elliptical helical versus spin-density wave structures.

2.2 Powder Diffraction

The nature of crystal growth is not always amenable to growing single crystals of all structures. While advances in growth techniques such as optical floating zone, molten flux, and chemical vapor transport have increased the availability of pure samples in the recent years, some samples may only be successfully prepared as polycrystalline samples. These samples, instead of possessing a single domain, are made up of randomly oriented, nano-sized grains. As a result, there is no single direction for each of the crystallographic planes in the sample to produce distinct diffraction spots. Instead, there is a powder average of

the diffraction. While this makes the data more convoluted and difficult to analyze, powder diffraction does have its advantages. As it is generally easier to prepare large amounts of polycrystalline samples, larger sample volumes can be used in diffraction experiments. For such weakly interacting particles as neutrons, this is especially important as many measurements are limited by the flux of scattered neutrons. Additionally, this improves the signal to noise ratio that can become an issue with complex sample environments. The time required for powder diffraction is also generally much shorter than for SC diffraction. This is due to SC diffraction requiring a reorientation of the sample and detector in two dimensions, while for powder diffraction only one dimension must be scanned (as discussed in Subsection 2.2.1). Taking into account these factors, neutron powder diffraction is a powerful and affordable tool for determining magnetic structures.

2.2.1 Theory

While SC samples have the atomic planes in well-defined directions, powder samples are composed of small, generally nano-sized, grains that are randomly oriented. The Laue equations still hold true, but now for all orientations of the grains. Any reflection obeying Bragg's Law of $n\lambda = 2d\sin\theta$ will be seen, thus changing from individual points into diffraction rings of equal angles. For this, a one-dimensional (1D) detector is sufficient to capture the accessible Bragg reflections. However, for complex structures where there are multiple planes of various atoms, this can lead to the convolution of diffraction peaks as the angles of diffraction are not separated enough from each other. This shows how essential monochromated incident neutrons are to improve resolution, as any uncertainty in neutron wavelength will increase the full-width half-max parameters and further convolute the diffraction peaks. As each peak will provide a distance of separation for atomic planes, it is possible to model the diffraction pattern from symmetry, lattice parameters, and atomic positions.

2.2.2 Setup

Neutron powder diffraction (NPD) data used in this thesis was taken at HB-2A powder diffractometer (Figure 2.4) at HFIR at ORNL that makes use of Debye-Scherrer geometry. HB-2A has a range of $2 < 2\theta < 155$ covered by 44 ^{3}He detectors. Each detector is separated by approximately three degrees in 2θ so the detector bank is moved to scan the desired 2θ range. The neutrons are reflected off of a germanium wafer-stack monochromator to provide wavelengths of 1.54 and 2.41 Å. Collimation is provided by a 12' pre-sample collimator, a removable 21' post-sample collimator, and 12' collimators for each detector tube. Samples are loaded into aluminum, copper, or vanadium cans and can be mounted inside of a variety of sample environments. Due to the low background of HB-2A, measurements can be performed in cryofurnaces (4-800 K), ^{3}He cryostat ($>$ 300 mK), dilute refrigeration cryostat ($>$ 30 mK), or furnace ($<$ 1800 K). In addition, magnetic fields up to 7 T can be applied and high-pressure cells including diamond anvils.

2.2.3 Refinement of Data

As with the refinement of SC data, powder data can be refined using the Rietveld method and the Fullprof suite [44]. However, as the powder diffraction does not have the spatial resolution found in four-circle diffractometers due to powder averaging, Bragg reflections are often convoluted and multiple reflections will often be located at the same position in 2θ. As a result, individual peaks can often not be sufficiently isolated to be integrated individually. Instead, the geometry of the peaks (determined by the configuration and geometry of the scattering instrument) must also be modeled. For X-ray diffraction, a simple Gaussian profile is generally sufficient. However, it is common for there to be a Lorentzian ($\frac{2/\pi H}{1+4/H^2x^2}$) component present or instead of the Gaussian. To accommodate this range of weighting, a pseudo-Voigt profile function is used of the following form

$$\Sigma(x) = \eta L'(x) + (1-\eta)G'(x), \tag{2.6}$$

Figure 2.4: Image of HB-2A powder diffractometer located at Oak Ridge National Laboratory. The pre-sample collimator, detector bank of 44 He ^{3}He detector tubes, goniometer for mounting sample environments, and the beam stop are labeled [46].

where $L'(x)$ and $G'(x)$ are the Lorentzian and Gaussian contributions respectively. For data collected at HB-2A, the peak shape is determined by a Thompson-Cox-Hastings pseudo-Voigt convoluted with axial divergence asymetry function modeled with Gaussian and Lorentzian halfwidth components (H_G and H_L respectively) of

$$H_G^2 = (U + D_{ST}^2)\tan^2\theta + V\tan\theta + W + \frac{I_G}{\cos^2\theta}, \tag{2.7}$$

$$H_L = X\tan\theta + \frac{[Y + F(S_Z)]}{\cos\theta}, \tag{2.8}$$

where U, V, and W are halfwidth parameters, D_{ST} is a strain paramter, I_G is an isotropic size effect, X is the Lorentzian isotropic strain parameter, Y is the Lorentzian isotropic size paramter, and $F(S_Z)$ is an isotropic size parameter [47]. Similar to SC refinement, a minimization of the variance between the peak intensities of the observed y_i and calculated patterns $y_{c,i}(\boldsymbol{\alpha})$ at each step given as

$$\chi^2 = \sum_i W_i \Big\{ y_i - y_{c,i}(\boldsymbol{\alpha}) \Big\}^2, \tag{2.9}$$

In powder diffraction, the calculated pattern is a function of the parameter vector $\boldsymbol{\alpha}$ and contains the refined variables mentioned above. For a single phase, this can be more explicitly represented at the ith step by

$$y_{c,i} = \sum_h \{LACF^2\}_h \Omega(T_i - T_h) + b_i, \tag{2.10}$$

where h labels the Bragg reflection, L_h contains Lorentzian factors, A_h is the absorption correction, F_h is the structural form factor, C_h contains further parameters such as preferred orientation and extinction, and Ω is the profile function including sample and instrumental effects described above.

The Fullprof software suite includes a tool, k-search, for the determination of the magnetic propagation vector. Reasonable candidate propagation vectors are then inputted into SARAh-Representational Analysis [48] to calculate magnetic structures allowed by the crystalline space group and the magnetic propagation vector. SARAh-Refine [48] then allows for selection of the irreducible basis of the magnetic symmetry. The corresponding basis

vectors of the magnetic structure are used to produce a magnetic phase to be refined in Fullprof. After the crystalline structure and all of the shape parameters have been refined from a diffraction pattern taken above the magnetic transition temperature, refinement is performed including one of the magnetic phases with a diffraction pattern taken below the magnetic transition. The magnetic phase will take a form factor of

$$F_h^2 = |\boldsymbol{F}_\perp(\boldsymbol{h})|^2 - (\boldsymbol{e} \cdot \boldsymbol{F_m}(\boldsymbol{h}))^2, \tag{2.11}$$

where $\boldsymbol{F_m}(\boldsymbol{h})$ is the magnetic structure factor and $\boldsymbol{e}$ is the unit vector along $\boldsymbol{h}$. By fixing the refined parameters from the crystalline structure, the magnetic profile will retain the same profile parameters and the magnetic structure can be refined as a coefficient for each of the magnetic basis vectors. The statistical fit is taken into consideration with other experimental results as well as theoretical justification or modeling to determine the magnetic ground state of the sample.

2.3 Inelastic neutron diffraction

Elastic neutron scattering can provide magnetic and atomic structures, but it provides no insight into energy transfers and therefore does not probe the electron, phonon, nor magnon energy dispersions of the material. As mentioned in Subsection 2.1.1, integration over all energies of scattered neutrons results in evaluating the correlation function at time equal to zero. However, by measuring the energy of the scattered neutrons, it is possible to determine the energy transfer during the collision. Combining this with the scattering vector provides a dispersion relation that probes the excitations of both the atomic and magnetic structures. The physical excitations from the atomic structure manifest in phonons and the excitations can be classified as acoustic or optical. The excitations of the magnetic structure revolve around exciting the spins in the ordered structure. The most simple case would be in an FM chain where the most fundamental excitation would be a single spin flip. However, as phonons spread the physical excitation over the atomic lattice, so too do magnons spread the

magnetic excitations. Describing these excitations with a Hamiltonian gives further insight into the mechanisms of magnetic behavior of the studied materials.

2.3.1 Background

While elastic neutron diffraction measures the cross section's angular derivative, inelastic neutron scattering (INS) measures both angular and energetic derivatives. This means that for along $dE = 0$, inelastic measurements will coincide with elastic measurements. Inelastic scattering provides the dynamical structure factor $S(\boldsymbol{q}, \omega)$. The coherent signal measures collective phenomena such as phonons and spin waves, while the incoherent signal measures individual phenomena like atomic diffusion. The intensity limits on inelastic scattering and the requirement of being able to measure the energy of outgoing neutrons mean that inelastic scattering is more time consuming and costly than elastic scattering. Two approaches to acquiring INS spectra are using time of flight (TOF) or a triple-axis setup. For TOF methods, incident neutrons are monochromated and the scattered neutrons are measured for their time of flight and their scatter position. By measuring TOF, it is straightforward to calculate the energy shift of the neutrons. For the data in Chapter 4, INS measurements were taken at the Disk Chopper Spectrometer (DCS) at the National Institute of Standards and Technology. DCS utilizes seven disk choppers to monochromate and pulse the incoming neutrons. The discrete pulses allow for measuring of TOF. The other primary method for INS is triple-axis spectrometers. Triple-axis spectrometers use an analyzer to measure the energy of the scattered neutrons.

INS measurements probe both magnetic and structural excitations. Structural excitations can be understood from the frame of coupled harmonic oscillators where $E = (n + \frac{1}{2})\hbar\omega$ for each oscillator. Quantizing the phonons reveals that the total energy of phonon excitations can be described by

$$E_{phonons} = \sum_{\boldsymbol{q},b} E_{\boldsymbol{q},b} = \sum_{\boldsymbol{q},b} (n_{\boldsymbol{q},b} + \frac{1}{2})\hbar\omega_b(\boldsymbol{q}), \tag{2.12}$$

where $\boldsymbol{q}$ is the wave vector and b is the phonon branch. As powder INS will average over the domain orientations, the directional dependence of $\boldsymbol{q}$ convolutes similar to in diffraction. For atoms with more than a single atom per primitive cell, there will exist both acoustic

and optical branches of phonons. The extra branches are a result of the degrees of freedom resulting from the atoms in each primitive cell. The acoustic branches are lower in energy while the optical branches are higher in energy. At the boundary of the first Brillouin zone, there is a frequency gap between the optical and acoustic branches where there are no wavelike solutions for the equations of motion.

For magnetic excitations, the spectrum depends extensively upon the Hamiltonian description. One of the strengths of INS is the ability to test model Hamiltonians against the neutron dispersion. This becomes of particular importance in small spin systems where quantum fluctuations often cause deviations from the classical models. Limits on theoretical models often require for certain assumptions and estimations, and experimental data to support or contradict these simplifications.

For the case of spin-1/2 1D chain with FM interactions, the simplest excitation is a single spin flip at a single site, a change in spin of 1 indicating a boson. This bosonic excitation is referred to as a magnon. This resulting state, with all atoms aligned except on-site anti-aligned, is not an eigenstate of the Hamiltonian. However, using a plane wave to diagonalize the Hamiltonian gives

$$E(q) = -2NS^2J + 4JS(1 - \cos qa), \tag{2.13}$$

where N is the number of sites, S is the spin size (here 1/2), J is the nearest neighbor interaction strength, and a is the interatomic spacing. This shows how the single spin flip is not localized to a single site, but is spread over the lattice with a dispersion relation of $\hbar\omega = 4JS(1 - \cos qa)$. This is similar to how a singular atomic displacement results in an excitation that also extends over the lattice as a phonon. Thus magnon excitations are expected to follow a similar function and not result in a continuous dispersion.

One magnetic excitation that has attracted much attention is the spinon. The spinon is a fermion, spin-1/2, excitation that occurs as a splitting of a magnon excitation. One well-studied example is the 1D spin-1/2 AFM chain. As seen in Figure 2.5, a single spin flip into an uuu section can be separated into two spin-1/2 uu sections (a). These domain walls can propagate freely in an unperturbed chain (b)-(c). In a strictly isotropic 1D Heisenberg chain, there is no binding of the spinon excitations. However, the presence of a staggered

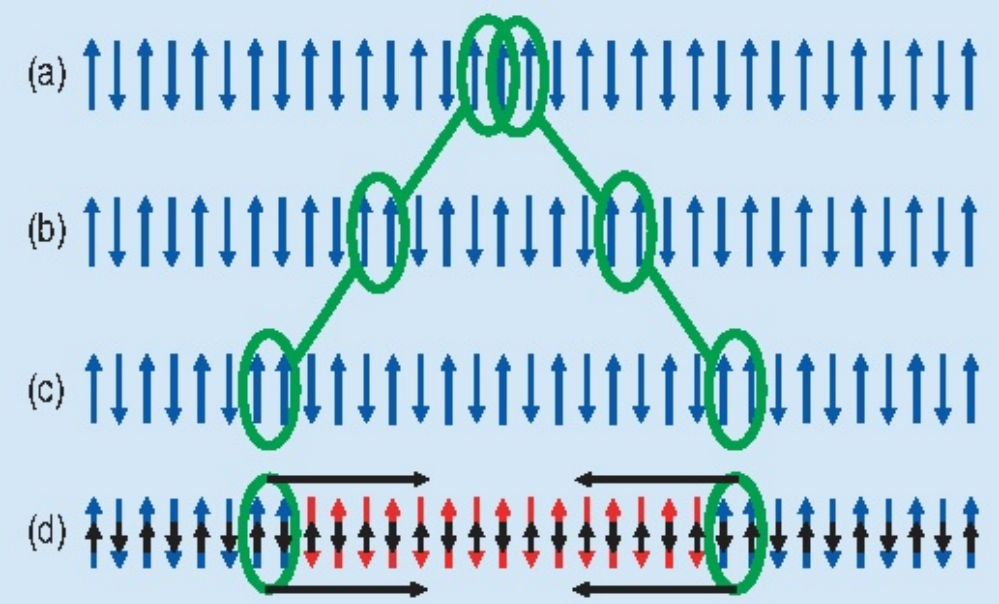

Figure 2.5: (a) A single, localized spin flip along a one-dimensional, spin-1/2 AFM chain. (b)-(c) Separation of spin-1/2 domain walls, spinons. (d) In the presence of a staggered field, thus breaking the symmetry between odd and even sites, the attraction of spinons creates a bound pair [49].

field breaking the symmetry between odd and even sites creates a binding energy between the pair (d) [49]. Instead of the singular values of the dispersion relation seen in magnons, the bound pairs form a spectrum of possible energies for a given $\boldsymbol{q}$ as seen in Figure 2.6. This continuum in the dispersion is one of the indicators for fractional spin excitations and such excitations have attracted much attention for the exotic behaviors seen in such systems. The novel behavior is of particular interest due to the ability to compare quantum theoretical models with experimental data. Experimental INS data is crucial to test the limitations of these theoretical models and offers an ideal route to investigate the fundamental magnetic interactions of complex materials.

2.3.2 Data analysis

Data reported in Chapter 4 was examined using the data analysis software Dave [51]. Due to the complex nature of $S(\boldsymbol{q}, \omega)$, it is generally not possible to refine data in the same way as for elastic scattering. Instead, simulations using the appropriate Hamiltonian are matched to the data and parameters are accordingly adjusted. The nature of the excitations can often be determined from the qualitative behavior of the form factor. Experimental inelastic data provides a testing ground for theory as well as reveals the shortcomings in current theoretical models (like linear SWT). Modeling of INS data in Chapter 4 was performed by Luwei Ge from Georgia Tech.

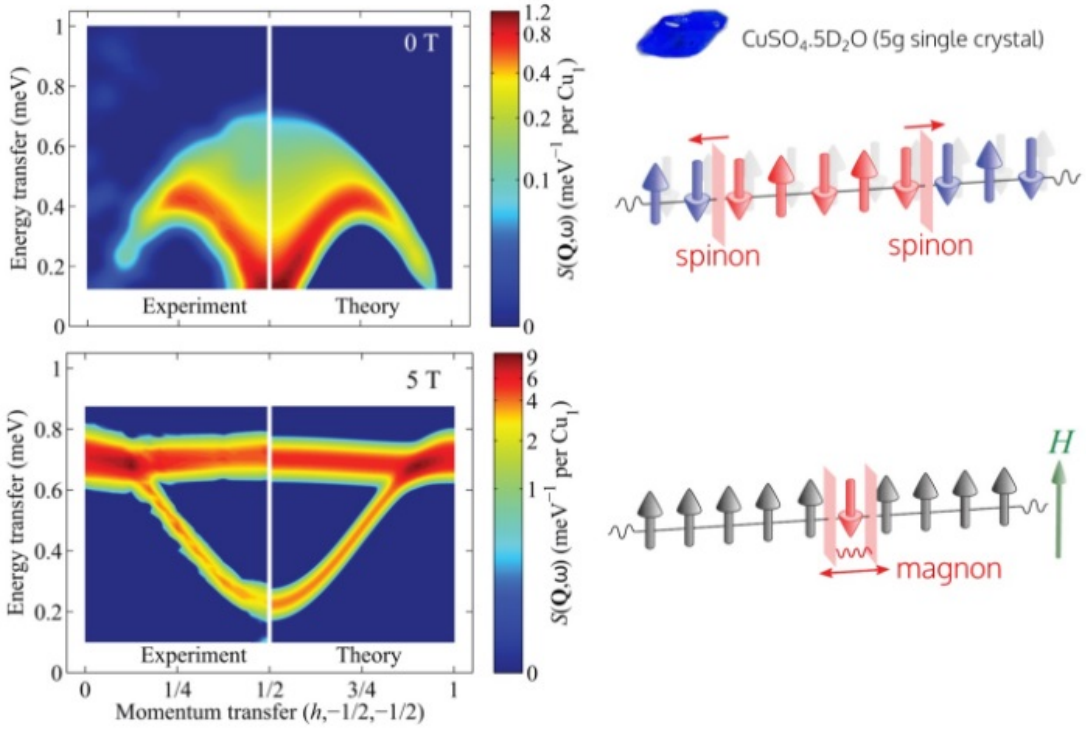

Figure 2.6: Examples of both the spinon continuous spectrum and magnon dispersion revealed in $CuSO_4{\cdot}5D_2O$ by Martin Mourigal et al [50].

Chapter 3

Non-scattering Measurements

While neutrons are one of the most efficient and developed methods for revealing the magnetic structure of materials, additional techniques are key to provide a more complete understanding of material properties. Practical limitations on neutron measurements include both cost and time. Due to the weak interaction of neutrons with matter, an advantageous property in many ways, large neutron sources are required to make scattering measurements feasible. Additionally, depending on the instrument capabilities, the temperature resolution that can be obtained is limited. To explore material properties further, measurement techniques that provide different information than scattering include transport property, thermal, density of states, susceptibility, and localized microscopy. There also exist complementary techniques to probe elementary excitations such as resonant inelastic X-ray scattering. A prudent selection of measurement techniques is necessary to provide the greatest return of useful information.

In this dissertation, complementary and supplementary techniques were used to examine structural, magnetic, and transport properties of the materials presented. X-ray diffraction (XRD) was used to determine the purity of the synthesized samples, measure lattice parameters and atomic positions, and measure the temperature dependence of lattice parameters. Specific heat measurements were used to corroborate transition temperatures and for the fitting of interaction strengths using high-temperature series expansion. Magnetization measurements probe the FM or AFM nature of the dominant interactions, the magnetic moment at saturation, and transition field strengths. DC and AC susceptibility

measurements were used to determine magnetic ordering temperatures and for fitting with high-temperature series expansion. By applying DC fields during susceptibility measurements, field dependence of the transitions helps reveal the FM or AFM nature of the transitions and can be used to produce magnetic phase diagrams. Resistivity measurements were used to supplement susceptibility measurements to determine transition temperatures.

3.1 X-ray Diffraction

One of the most pervasive difficulties facing condensed matter physics is sample quality. To address this, X-ray diffraction is an important step in providing a check of sample quality by providing structural information on the sample via an affordable and quick measurement. Returning to $n\lambda = 2d\sin\theta$, photons of $\sim$1-2Å are useful to probe interatomic distances on that order. This is provided by photons of $\sim 10^4$eV. One of the primary advantages of XRD is the availability, affordability, and small size of X-ray sources. X-ray diffraction techniques are non-destructive and exposed samples do not pose a radiation hazard as may be the case from neutron measurements. Limitations for XRD include a strong $\sin\theta/\lambda$ dependence and, as a result, data quality at high Q values may suffer. X-rays also interact with the valence electron cloud and not the nucleus, as in neutron techniques. This makes neutron scattering preferable for precise measurement of the atomic positions and Debye-Waller factor. The Debye-Waller factor provides the average of the squared displacements of the atomic nuclei. The large, established databases of structural parameters for many materials allows for comparison to isostructural materials. Databases allow for quick searching of phases including constituent atoms. Impurity phases can also be indexed and weighted.

All materials presented in this dissertation were analyzed by XRD prior to further measurements to ensure that only high-quality samples were used. Each sample was annealed under increasing temperatures with intermediate grindings and the temperature profile with the best XRD was used to produce the remaining sample. Diffraction was performed on polycrystalline or single crystal samples that were ground with an agate mortar and pestle into nano-sized, randomly distributed powder. The powder was placed between Teflon foil in a thin layer to reduce multiple scattering events. A fixed anode X-ray tube is reflected and

focused using a monochromator to select the Cu Kα1 radiation of 1.54059 Å (9.048 keV). A HUBER imaging-plate Guinier camera 670 is used to record the diffraction pattern (Figure 3.1). Structural refinements are performed using FullProf [44] as described in Subsection 2.2.3. For temperature dependent measurements, a closed cycle refrigeration unit is used to reach as low as 5 K.

3.2 Specific Heat

Specific heat measures the change in average kinetic energy of particles with the addition of heat energy. For purposes of this dissertation, isobaric specific heat of $C_P = \left(\frac{\delta Q}{\delta T}\right)$. For a purely classical and magnetically isolated system, upon cooling to absolute zero, C_P would drop to $\frac{3}{2}Nk_B$ where N is the number of atoms in the gas. However, in certain quantum systems with discrete energy levels, such as an electron gas in a magnetic field, the specific heat at zero temperature drops to zero. In these quantum systems, there will be a low-temperature maximum around $\sim k_bT$ arising from thermal excitations between two states called the Schottky anomaly [52]. However, in reality, degrees of freedom can remain down to zero temperature including magnetic degrees of freedom that are of interest in condensed matter. One example would be in a spin liquid, where a spin flip could freely propagate and thus continue to contribute to the specific heat. Triangular magnetic structures of the Heisenberg model were also shown to approach nonzero values at zero temperature [53], a result that is used in the fitting of specific heat data taken to ultra-low temperatures ($\sim$ 50K) to examine anisotropy in this dissertation.

Specific heat measurements performed in this dissertation were carried out using a Quantum Designs physical properties measurement system. A thermometer and heater are attached to a thermally conducting platform upon which the sample is mounted. Apiezon grease is used to provide a thermal contact. The platform is also connected to a thermal bath with a sufficient time constant to allow both the platform and sample to reach thermal equilibrium during measurements. Prior to measuring the sample, the puck and grease are measured to determine the addenda specific heat. While measuring the sample, a recording of the heat provided by the heater and the temperature of the sample allows a thorough

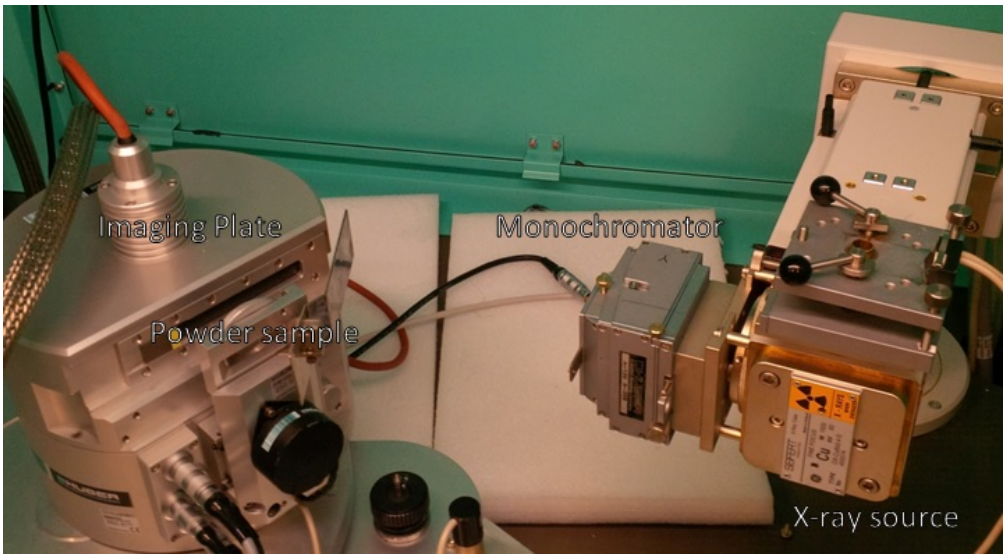

Figure 3.1: Labeled image of Huber X-ray Diffractometer showing the X-ray source tube with a copper anode, a monochromator to select the Cu Kα1 wavelength, sample holder for the crushed powder sample, and imaging plate where the diffraction pattern is recorded.

mapping of specific heat as a function of temperature. Subtraction of the addenda isolates the sample contribution to specific heat. A dilute refrigeration insert allows for temperatures as low as 50 mK to be reached and a heater allows measurement of up to 350 K.

3.3 DC Susceptibility and Magnetization

One of the most straightforward measurements of magnetic properties is the bulk magnetization ($\boldsymbol{M}$). By using $\boldsymbol{B} = \mu_0(\boldsymbol{H} + \boldsymbol{M})$, measurement of magnetic flux density ($\boldsymbol{B}$) as a function of magnetic field strength ($\boldsymbol{H}$) provides magnetization. Magnetic susceptibility (χ) measures the change in magnetization with an applied magnetic field strength by $\boldsymbol{M} = \chi(\boldsymbol{H})$ or $\boldsymbol{B} = \mu_0(1 + \chi)\boldsymbol{H}$. Diamagnetism is a magnetic repulsion that arises in all materials due to the rearrangement of electron pairs in an external field and corresponds with a negative susceptibility. Due to the weak nature of diamagnetism, it is overcome by other magnetic orderings. For a paramagnetic materials, unpaired electrons will align under application of external field and will provide a positive susceptibility that increases with lowering temperatures as $1/T$. FM materials with spontaneous domain magnetization will show a large positive value of the magnitude of the susceptibility. This is due to the ability to align the magnetic domains along the direction of the applied field. Upon transitioning from paramagnetic to ferromagnetic ordering, complex magnetic behavior is seen. AFM materials will have a small positive susceptibility relating to the ability to excite spins out of the magnetic ground state. Due to the LRO into a state with a net magnetization of zero, there is less of a response from an applied field as any alignment along with the field requires breaking this LRO. Ordering into the antiferromagnetic state from a paramagnetic state is usually accompanied by a peak and a reduction in susceptibility upon decreasing temperatures. For the paramagnetic phase of materials, the magnetic susceptibility behaves as

$$\chi = \frac{C}{T - T_{CW}}, \tag{3.1}$$

where C is the Curie constant and T_{CW} is the Curie-Weiss constant in Kelvin. This predicts a singularity at a temperature of $|T_{CW}|$ and T_{CW} will be positive for ferromagnetic ordering, zero for a purely paramagnetic material, and negative for antiferromagnetic ordering.

DC susceptibility (χ_{DC}) and magnetization measurements included in this dissertation were performed using a Quantum Design superconducting quantum interference device magnetometer. For this design, the sample is suspended in a coil of superconducting loops containing two similar Josephson junctions in each loop. In the absence of any magnetic flux in the loops, when a current is applied across the loop, it should pass through each Josephson junction equally. However, in the presence of a magnetic flux (Φ), an electromotive force will produce unequal currents across each junction. Due to the quantized nature of the magnetic flux, if the magnetic flux were to increase from zero beyond one-half quanta, the current in the loop would energetically favor increasing to yield one quantum. To avoid this, a critical current is used to keep the SQUID in resistive mode so that there is no sign change in current flow. For measuring χ_{DC}, Φ is measured to provide the magnetic flux density of $\boldsymbol{B} = \mu_0(1+\chi)\boldsymbol{H}$. By maintaining a constant field and varying the temperature of the sample, the temperature dependence of χ_{DC} can be mapped. By maintaining a constant temperature and varying the magnetic field strength $\boldsymbol{H}$ then $\boldsymbol{B} = \mu_0(\boldsymbol{H}+\boldsymbol{M})$ yields the bulk magnetization. DC susceptibility can be measured from 2 - 350 K with this setup.

3.4 AC Susceptibility

AC susceptibility (χ_{AC}) mirrors χ_{DC} in many ways. However, it is often possible to reach lower temperatures with χ_{AC} measurements, down to 300mK as opposed to 2K for most available χ_{DC} measurements. While frequency dependence requires consideration and can provide additional information about the magnetic behavior of the sample, low-frequency measurements capture effective DC behavior and can be scaled with DC measurements to provide a full susceptibility curve down to very low temperatures.

The AC susceptibility measurement is obtained using an AC-DC current calibrator (Valhalla Scientific, model 2700) and three lock-in amplifiers (Stanford Research, SR 830) [54]. The phases of the lock-in amplifiers are set to measure each harmonics signal, which is shifted from the oscillating magnetic field according to

$$E = A\{\chi_0^t h_0 \mathrm{cos}\omega t + \chi_1^t h_0^2 \mathrm{sin}2\omega t - 3/4\chi_2^t h_0^3 \mathrm{cos}3\omega t - ...\}, \tag{3.2}$$

where χ_0^t, $\chi_1^t h_0$, and $3/4\chi_2^t h_0^2$ are the first harmonic, second harmonic, and third harmonic components of χ_{AC}. The lock-in amplifiers are also set to read the linear component (first harmonic response) and the nonlinear components (second and third harmonic responses) with respect to the oscillating AC field frequency. The root mean square amplitude of the AC excitation field (h_0) varies from 0.43 to 4.3 Oe with frequency (f) ranging from 40 to 1000 Hz. The applied external DC magnetic field (H_{DC}) varies from 0 to 1000 Oe. The data were taken while warming up the sample from the base temperature with a rate of 7.6 mK/min with the zero-field-cooling process. Using small excitation fields, $\chi_0^t \approx \chi_{DC}$ Thus, in our analysis the linear AC susceptibility values have been scaled to the linear DC susceptibility measurements and are used to normalize both linear and nonlinear χ_{AC} components.

3.5 Resistivity

With magnetism stemming from the order of electron spins, it is natural that other electronic properties would provide insight into magnetic ordering. Electron mobility can be measured in bulk via resistivity, ρ, measurements and can distinguish between metals, insulators, semiconductors, and semimetals. For free electrons in an electric field, the force, F, is related to velocity, $\boldsymbol{v}$, and wavevector, $\boldsymbol{k}$, $\boldsymbol{F} = m\frac{d\boldsymbol{v}}{dt} = \hbar\frac{d\boldsymbol{k}}{dt}$ and in a constant electric field $\boldsymbol{E}$ yields $\boldsymbol{j} = nq\boldsymbol{v} = \boldsymbol{E}/\rho = ne^2\tau\boldsymbol{E}/m$ where $\boldsymbol{j}$ is the electron current density, n is electron density, and τ is the average time between collisions. Resistivity is defined by these parameters as $m/ne^2\tau$. For metallic samples, the resistivity will be small in magnitude and increase in magnitude with increasing temperature. This increase is due to the increased scattering from thermally excited ions. Semiconductors will have intermediate magnitudes of resistivity while insulators will have high magnitude values. Both semiconductors and insulators have decreasing resistivity with increasing temperatures due to the thermal excitation of the charge carriers into more mobile states. The exact nature of the resistivity behavior is based on the electronic band structure. As long-range magnetic ordering will alter the electronic band structure, a feature in resistivity may occur when the band structure is sufficiently changed near the Fermi surface. For this reason, resistivity measurements

were used to look for possible magnetic ordering and to provide concurring results with susceptibility measurements to create magnetic phase diagrams.

Resistivity measurements carried out in this dissertation were performed using a Quantum Design Physical Properties Measurement System. ρ was measured using the four-wire resistance method, where two wires measure the voltage, V, difference across a sample and two separate wires provide the current, I, across the sample. Combining this with Ohm's Law of $V = IR$, resistance (R) can be easily found by a simple V/I calculation. In order to extract the resistivity, the relation of $\rho = R\frac{A}{l}$, where A is the cross-sectional area and l is the length of the measured sample, is required to isolate the resistivity. To assist in the accuracy of this relationship, samples were pressed into pellets and cut using a rotating diamond saw into rectangular plates. The distance between the voltage leads on the sample are used to record l and the cross-sectional area was measured with calipers.

Chapter 4

Two Dimensional Frustrated Triangular Lattice Compounds

2D triangular lattice magnets (TLMs) have attracted much attention for their exotic magnetic properties. 2D structures such as the triangular lattice have been studied extensively theoretically, but experimental measurements have revealed previously unpredicted behaviors. Here, select triangular lattice materials have been examined to further the understanding of the lattice as well as to search for novel behaviors. In this chapter, we present the results of our research into 2D TLMS. Many of the results presented in this chapter have been published in Physical Review B in "Magnetic properties of the triangular lattice magnets $A_4B'B_2O_{12}$ (A = Ba, Sr, La; B' = Co, Ni, Mn; B = W)" (2017) [55] and "$Ba_8CoNb_6O_{24}$: A spin-$\frac{1}{2}$ triangular-lattice Heisenberg antiferromagnet in the two-dimensional limit" (2017) [56]. I would like to extend thanks to Haidong Zhou, Clarina dela Cruz, Jie Ma, Jaan Oitmaa, Minseong Lee, Eun Sang Choi, Kuan-Wen Chen, Ryan Baumbach, Harish Agrawal, Yoshimoto Kamiya, Nicholas P. Butch, Xuefeng Sun, Cristian Batista, Huibo Cao and Martin Mourigal for all of their contributions in both experimental and theoretical aspects of this research.

4.1 $A_4B'B_2O_{12}$ Transition Metal Compounds

To fully probe the intriguing ground states seen, as well as to provide experimental realizations of theoretical predictions, new TLMs must be discovered and explored. One of the most straightforward methods to engineer a 2D triangular lattice is by using a stacked layer model, such as that in the perovskite structure [57, 58]. The basic perovskite structure (ABO_3) can be considered as a stacking of three layers of AO_3 intercalated with layers of B ions. Both A and B site ions consist of corner-sharing octahedra formed with the surrounding oxygens. Other stacking mechanisms can be explored by possessing layers in which the alternating layers are instead edge sharing oxygen octahedra [57]. This can result in multilayered stacking structures with complex stacking orders. This is of particular interest from a materials engineering standpoint, as the introduction of non-magnetic and even vacant layers can reduce the interplane interactions and manifest a truer 2D behavior. The presence of vacant layers is promising to help ensure the interlayer interactions are sufficiently small compared to the intralayer interactions.

As an extension of this approach, we use close-packed stacking of perovskite layers to examine new 2D TLMs. One such promising structure is $A_4B'B_2O_{12}$ (A = Ba, Sr, La; B' = Co, Ni, Mn; B = W, Re). In this family of compounds, using $Ba_2La_2NiW_2O_{12}$ as the example shown in Figure 4.1, the magnetic transition metal (TM, here Ni^{2+}) and nonmagnetic W^{6+}/Re^{7+} ions reside at the center of the oxygen octahedra from the perovskite close-packed stacking. The magnetic and nonmagnetic ions occupy the ($3a$) and ($6c$) positions, respectively. This results in the TM octahedra that are corner sharing with the adjoining W/Re octahedra. The TMO_6 octahedral layer forms a TM^{2+}-triangular lattice in the ab plane. The TM layers are between two adjacent W/Re layers with a sequence of W/Re, vacant, W/Re layers between each TM layer. The vacant layer results from the strong electric repulsion between the W^{6+}/Re^{7+} ions. As desired, this significantly reduces the interplane interactions between the TM ions and enhances the 2D nature of the structure over the base perovskite structure. Of especial boon is the flexible chemistry of this structure, allowing for tuning of the magnetic properties. This can be accomplished by two means, applying chemical pressure or changing spin magnitude. To introduce chemical pressure in $A_4B'B_2O_{12}$,

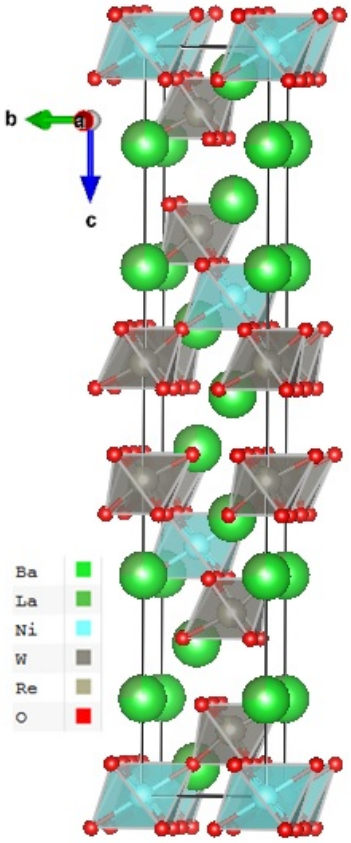

Figure 4.1: Crystal structure of $Ba_2La_2NiW_2O_{12}$, member of isostructural $A_4B'B_2O_{12}$ family [55].

the A site ions can be chosen from barium, strontium, and lanthanum with the appropriate choice of tungsten and rhenium on B′ to preserve charge. With the significant difference in ionic size between Ba^{2+}, smaller La^{2+}, and even smaller Sr^{2+}, there is a coinciding increase in chemical pressure. For the cobalt-containing family, this allows for the set of $Sr_4CoRe_2O_{12}$, $Sr_2La_2CoW_2O_{12}$, $Ba_2La_2CoW_2O_{12}$, $Ba_3LaCoReWO_{12}$, and $Ba_4CoRe_2O_{12}$. Additionally, the spin numbers in the system can be varied by selection of the B′ ion. Here, in the family of $Ba_2La_2TMW_2O_{12}$, the selected TMs possess spins numbers of effective spin-1/2 (Co^{2+}) to spin-1 (Ni^{2+}), and spin-5/2 (Mn^{2+}). Combining these, the magnetic properties of new TLMs can be studied in $A_4B'B_2O_{12}$ along with how the perturbations of chemical pressure and spin numbers affect them. Several members of the $A_4B'B_2O_{12}$ have been previously reported [59, 60, 61] and the susceptibility of $Ba_2La_2MnW_2O_{12}$ [62] has been measured down to 2 K. No detailed studies of the magnetic properties of this family have been carried out.

We have examined a total of seven members of $A_4B'B_2O_{12}$ for their structural and magnetic properties by means of X-ray diffraction, DC and AC susceptibility (χ_{AC}, χ_{DC}), neutron powder diffraction (NPD), and specific heat (C_P) measurements. The ground state is shown to be determined by the spin size of the B′ ions. For low spin compounds, FM interactions dominate with B′ = Ni yielding FM LRO and B′ = Co yielding FM behavior. Alternatively, for high spin, B′ = Mn, the ground state adopts an AFM LRO. Due to the competing superexchange interactions present in the $A_4B'B_2O_{12}$, we propose the dominant interaction is selected by moment size.

The samples examined in this dissertation are $Sr_4CoRe_2O_{12}$, $Sr_2La_2CoW_2O_{12}$, $Ba_2La_2CoW_2O_{12}$, $Ba_3LaCoReWO_{12}$, $Ba_4CoRe_2O_{12}$, $Ba_2La_2NiW_2O_{12}$ and $Ba_2La_2MnW_2O_{12}$. The polycrystalline samples were prepared via the standard solid state reaction method. Stoichiometric amounts of $BaCO_3/SrCO_3$, La_2O_3 (pre-dried at 980 C overnight), $CoCO_3$/ NiO/MnO, and WO_3/Re metal were mixed in agate mortars and compressed into pellets. The pressed pellets were annealed at temperatures of 1000 C for $Ba_4CoRe_2O_{12}$, 1050 C for $Ba_3LaCoReWO_{12}$, 1100 C for $Sr_4CoRe_2O_{12}$, and 1250 C for $Ba_2La_2CoW_2O_{12}$, $Sr_2La_2CoW_2O_{12}$, $Ba_2La_2MnW_2O_{12}$, and $Ba_2La_2NiW_2O_{12}$ for a duration of 20 hours each.

4.1.1 Cobalt Containing Compounds

All five Co containing compounds are pure single phase with the space group *R-3mH*. Rietveld refinement of the XRD patterns are presented in Figure 4.2. For ease of reference, $Sr_4CoRe_2O_{12}$ will be used as a continuing example throughout this section. $Sr_4CoRe_2O_{12}$ has lattice constants of $a = b = 5.5446(3)$ Å and $c = 26.7382(13)$ Å with refined structural parameters for all compounds presented in Table 4.1. The A site ion governs the lattice parameters, with increasing radii from strontium to lanthanum to barium resulting in increased lattice parameters. Site mixing betwen Co ions on the B site and W/Re ions on the B′ site were also tested. There was no improvement in the refinements from the fully ordered structure, indicating there is not significant disorder in these compounds. The XRD resolution incidates the disorder is likely below 5%.

DC susceptibility measurements were performed on all five Co-containing members and show no order down to 2 K. The inverse χ_{DC} data is shown in Figure 4.3. All compounds show a slope change in these $1/\chi_{DC}$ versus T curves around 80 K, indicating the spin state transition of the Co^{2+} ions from high spin (S = 3/2) to low spin (S = 1/2). This spin transition occurs due to the octahedral environment created by the surrounding oxygens. The crystal field and spin-orbital coupling combine to create a low-temperature ground state with effective S = 1/2 Kramers doublet, as described by Low [63] and further examined by Lloret *et al.* [64]. Linear fitting of the high temperature regime of 150 K to 300 K, continuing use of $Sr_4CoRe_2O_{12}$ as an example, yields a Curie-Weiss constant of θ_{CW} = -17 K and μ_{eff} = 4.72 μ_B while the linear fitting in the low temperature regime from 4.0 K to 15 K yields θ_{CW} = 1.0 K and μ_{eff} = 3.91 μ_B. The positive θ_{CW} at low temperatures indicate the effective spin-1/2 Co^{2+} ions interact via FM exchange interactions. Both the spin state transition and the positive θ_{CW} at low temperatures were observed in the other four Co-containing compounds. DC magnetization data was taken at 1.8 K and is presented in the insets of Figure 4.3. In order to calculate the saturation magnetization (M_S), a linear fit of high field data was used to account for the Van Vleck paramagnetism. The magnetization data shows a consistent tendency to saturate at around $\mu_0 H_s \approx 3$ T. The extrapolated value of M_S = 1.52 μ_B/Co^{2+} and a powder-averaged gyromagnetic ratio g = 3.04 were found in $Sr_4CoRe_2O_{12}$.

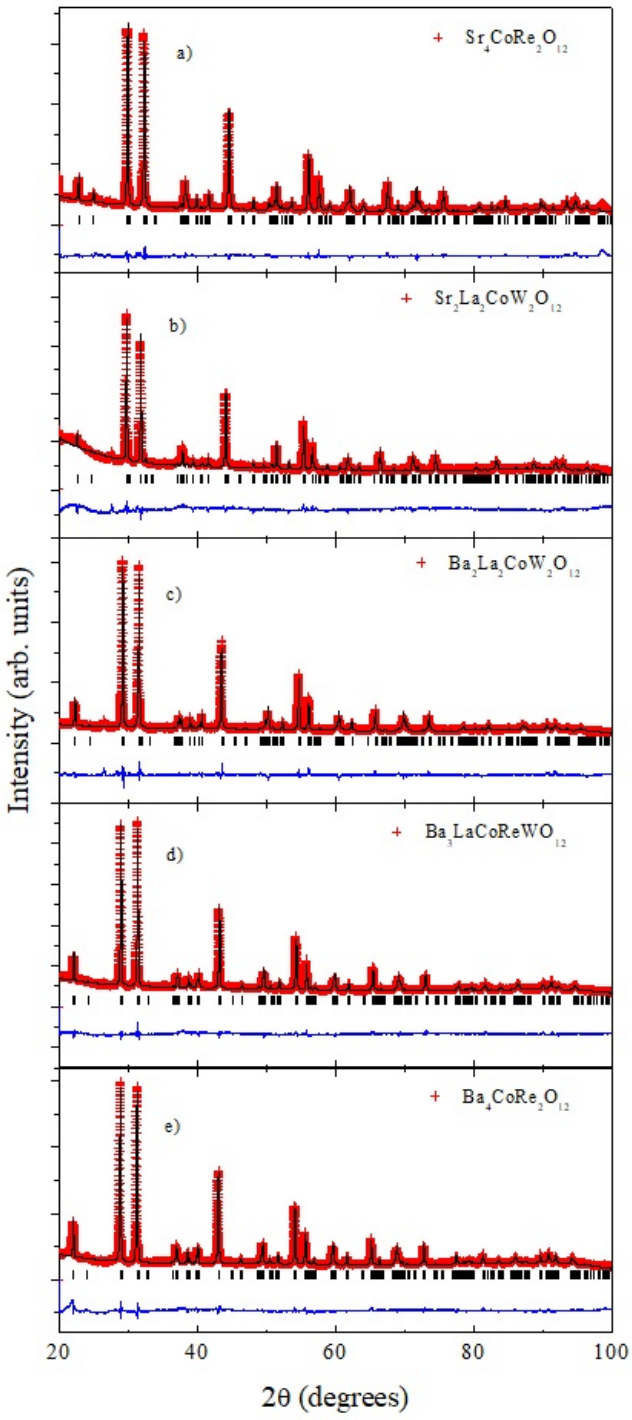

Figure 4.2: Refinement of X-ray diffraction data for cobalt containing members of $A_4B'B_2O_{12}$ [55].

Table 4.1: Structural parameters for the Co containing compounds at room temperature (space group *R-3mH*) determined from refined XRD measurements [55].

Refinement	Atom	Site	x	y	z	Occupancy
$Sr_4CoRe_2O_{12}$ $\chi^2 = 2.29$ (a)	Sr1	6c	0	0	0.12982(5)	0.16666
	Sr2	6c	0	0	0.29351(6)	0.16666
	Co	3a	0	0	0	0.08333
	Re	6c	0	0	0.42186(3)	0.16667
	O1	18h	0.50289(50)	0.49711(50)	0.12312(14)	0.50
	O2	18h	0.49249(53)	0.50751(53)	0.29174(19)	0.50
			$a = b = 5.54464(26)$ (Å), $c = 26.73815(126)$ (Å)			
			Overall B-factor = 1.332 (Å^2)			
$Sr_2La_2CoW_2O_{12}$ $\chi^2 = 5.41$ (b)	Sr	6c	0	0	0.13664(13)	0.16667
	La	6c	0	0	0.28914(8)	0.16667
	Co	3a	0	0	0	0.08333
	W	6c	0	0	0.42105(8)	0.16667
	O1	18h	0.50728(82)	0.49272(82)	0.12425(22)	0.50
	O2	18h	0.48772(73)	0.51228(73)	0.29016(28)	0.50
			$a = b = 5.60493(41)$ (Å), $c = 26.58453(197)$ (Å)			
			Overall B-factor = 2.211 (Å^2)			
$Ba_2La_2CoW_2O_{12}$ $\chi^2 = 3.45$ (c)	Ba	6c	0	0	0.13467(8)	0.16667
	La	6c	0	0	0.29032(7)	0.16667
	Co	3a	0	0	0	0.08333
	W	6c	0	0	0.41635(7)	0.16667
	O1	18h	0.50913(77)	0.49087(77)	0.11994(23)	0.50
	O2	18h	0.48361(62)	0.51639(62)	0.29662(28)	0.50
			$a = b = 5.68043(12)$ (Å), $c = 27.37418(60)$ (Å)			
			Overall B-factor = 2.671 (Å^2)			
$Ba_3LaCoWReO_{12}$ $\chi^2 = 1.43$ (d)	Ba1	6c	0	0	0.12939(6)	0.12500
	La1	6c	0	0	0.12944(6)	0.04167
	Ba2	6c	0	0	0.29533(6)	0.12500
	La2	6c	0	0	0.29533(6)	0.04167
	Co	3a	0	0	0	0.08333
	W	6c	0	0	0.42185(6)	0.08333
	Re	6c	0	0	0.42185(6)	0.08333
	O1	18h	0.51068(82)	0.48932(82)	0.12143(23)	0.50
	O2	18h	0.48365(80)	0.51635(80)	0.29260(32)	0.50
			$a = b = 5.70429(9)$ (Å), $c = 27.675722(54)$ (Å)			
			Overall B-factor = 1.757 (Å^2)			
$Ba_4CoRe_2O_{12}$ $\chi^2 = 4.51$ (e)	Ba1	6c	0	0	0.12911(8)	0.16666
	Ba2	6c	0	0	0.29435(9)	0.16666
	Co	3a	0	0	0	0.08333
	Re	6c	0	0	0.42089(8)	0.16667
	O1	18h	0.50262(108)	0.49738(108)	0.12325(29)	0.50
	O2	18h	0.47513(97)	0.52487(97)	0.28794(41)	0.50
			$a = b = 5.72455(33)$ (Å), $c = 27.76966(161)$ (Å)			
			Overall B-factor = 1.694 (Å^2)			

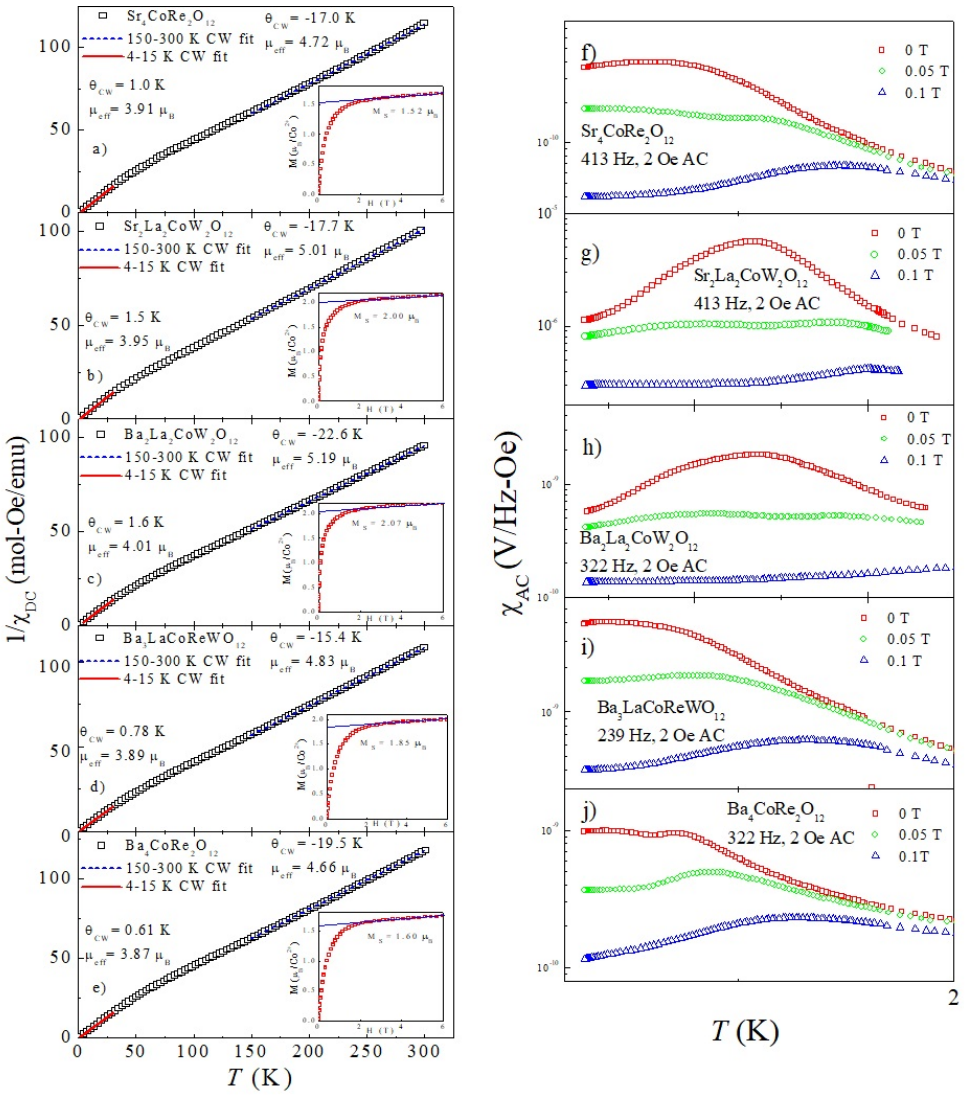

Figure 4.3: (a-e) $A_4CoB_2O_{12}$ compound DC susceptibilities [55]. The solid red and dashed blue lines are the Curie-Weiss fittings of the low-temperature (4 - 15 K) and high-temperature (150 - 300 K) regimes, respectively. Insets: The DC magnetization taken at 1.8 K with the saturation magnetization of the Co^{2+} ion extrapolated using a linear fit to account for the Van Vleck paramagnetic contribution. (f-j) The real part of the AC susceptibility χ_{AC} for $A_4CoB_2O_{12}$ compounds measured from 0.3 to 2.0 K under applied DC magnetic fields. Excitation fields of 2 Oe at low AC frequencies were used to help comparison to DC susceptibility behavior.

For the four other compounds, the obtained g is around $3 \sim 4.2$. The magnetic parameters for all compounds are summarized in Table 4.2.

AC susceptibility measurements were taken on all five Co-containing compounds under different DC fields down to 300 mK and are shown in Figure 4.3. For $Sr_4CoRe_2O_{12}$, χ_{AC} shows a swift increase upon decreasing temperature below 1.5 K and a subsequent broad peak. While this is not necessarily indicative of FM LRO in and of itself, it is evidence for FM behavior such as FM correlations or the formation of FM clusters. To this end, we define T_{FM} to be the FM behavior temperature based on a local minimum in the first derivative of χ_{AC}. For $Sr_4CoRe_2O_{12}$, $T_{FM} = 1.0$ K. The broad peak shifts to higher temperatures while simultaneously decreasing in magnitude with the increasing strength of the applied DC field. This increase of T_{FM} under applied field is consistent with the FM nature described by χ_{DC}. All Co-containing compounds show similar overall behavior for χ_{AC} yet distinct T_{FM}. These results are summarized in Table 4.2 with all Co compounds showing FM behavior near 1 K. Two compounds, $Sr_2La_2CoW_2O_{12}$ and $Ba_2La_2CoW_2O_{12}$, have an additional second peak in χ_{AC} at lower temperatures with the application of a 0.05 T DC field. The nature of this peak and if it represents further magnetic behavior remain to be explored.

4.1.2 $Ba_2La_2NiW_2O_{12}$

$Ba_2La_2NiW_2O_{12}$ was examined by NPD and shown to be pure phase of the space group *R-3mH*, as are the other members of $A_4B'B_2O_{12}$. Rietveld refinement of the NPD pattern is presented in Figure 4.4 (a). Refined structural parameters for $Ba_2La_2NiW_2O_{12}$ are $a = b = 5.6622(4)$ Å and $c = 27.3661(22)$ Å. Detailed structural parameters are reported in Table 4.3. Specific heat data taken at zero field shows a sharp peak at 6.2 K as shown in Figure 4.4 (b). On applying fields, the peak broadens out and shifts to higher temperatures. The transition temperatures increase linearly with increasing field as shown in the insert of Figure 4.4 (b). Measuring with a 50 Oe field, χ_{DC} shows a sharp rise under cooling with $T_C = 6.2$ K as shown in Figure 4.4 (c), in agreement with C_P. Similar to the behavior in C_P, increasing applied fields shift the transition to higher temperatures while becoming broader. Linear fitting of the inverse DC susceptibility from 150 to 300 K give positive $\theta_{CW} = 25.5$ K and μ_{eff}

Table 4.2: Summary of magnetic properties (FM behavior, FM transition, and AFM transition temperatures T_{FM}, T_{C}, T_{N}, Curie-Weiss constant θ_{CW}, effective magnetic moment μ_{eff}, saturation magnetization $\mathrm{M_S}$, and gyromagnetic ratio g) of $\mathrm{A_4B'B_2O_{12}}$ compounds [55].

Compound	$T_{\mathrm{FM}}/T_{\mathrm{C}}/T_{\mathrm{N}}$ (K)	θ_{CW} (K)	μ_{eff} (μ_{B})	$\mathrm{M_S}$ (μ_{B})	g
$\mathrm{Sr_4CoRe_2O_{12}}$	1.0	1.0	3.91	1.5	3.0
$\mathrm{Sr_2La_2CoW_2O_{12}}$	1.26	1.5	3.95	2.0	4.0
$\mathrm{Ba_2La_2CoW_2O_{12}}$	1.28	1.6	4.01	2.1	4.2
$\mathrm{Ba_3LaCoReWO_{12}}$	0.83	0.78	3.89	1.9	3.8
$\mathrm{Ba_4CoRe_2O_{12}}$	0.87	0.61	3.87	1.6	3.2
$\mathrm{Ba_2La_2NiW_2O_{12}}$	6.2	25.5	3.19	≈ 2	≈ 2
$\mathrm{Ba_2La_2MnW_2O_{12}}$	1.7	-10.7	5.73	–	–

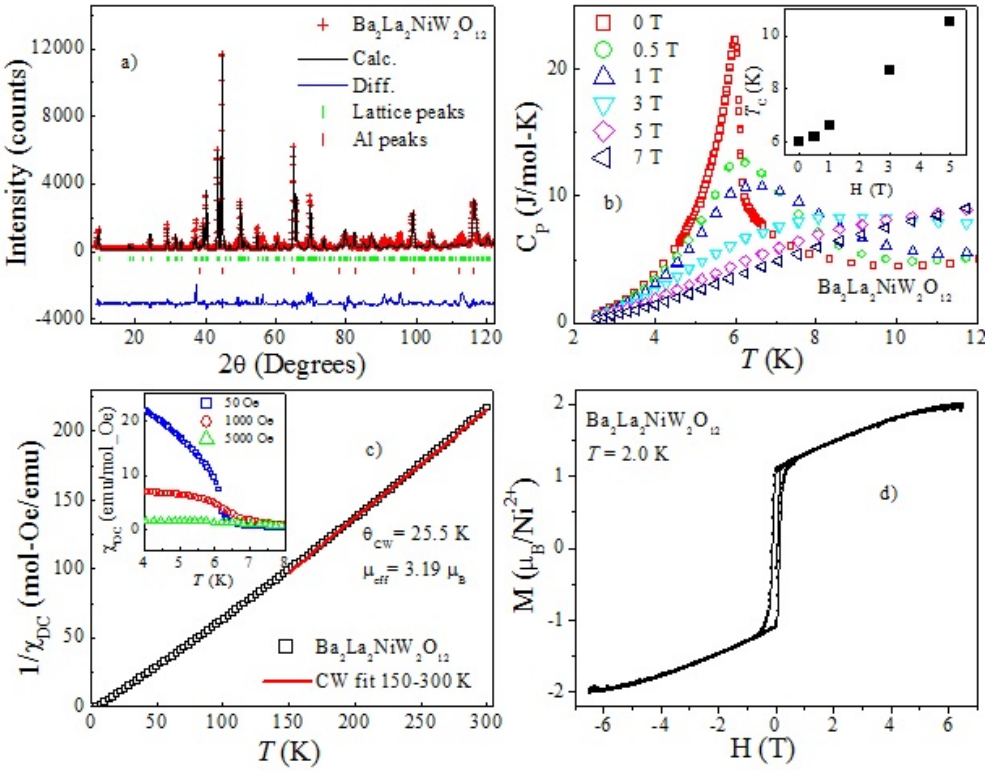

Figure 4.4: For $Ba_2La_2NiW_2O_{12}$ [55], (a) the Rietveld refinement of the neutron powder diffraction pattern measured using a neutron wavelength of $\lambda = 1.5405$Å at room temperature. (b) The temperature dependence of specific heat measured under different strength DC fields. Inset: the field dependence of the Curie temperature found from the peak in specific heat. (c) The inverse DC susceptibility with the solid line being the Curie-Weiss linear fitting. Inset: the temperature dependence of DC susceptibility measured under different strength DC fields. (d) The DC magnetization curve measured at 2 K showing hysteresis loop.

Table 4.3: Structural parameters for $Ba_2La_2NiW_2O_{12}$ and $Ba_2La_2MnW_2O_{12}$ at room temperature (space group *R-3mH*) determined from refined neutron powder diffraction measurements [55].

Refinement	Atom	Site	x	y	z	Occupancy
	Ba	6c	0	0	0.13324(60)	0.16667
	La	6c	0	0	0.29309(44)	0.16667
$Ba_2La_2NiW_2O_{12}$	Ni	3a	0	0	0	0.08333
(a)	W	6c	0	0	0.41881(68)	0.16667
	O1	18h	0.49760(81)	0.50240(81)	0.11707(27)	0.50
	O2	18h	0.47868(74)	0.52132(74)	0.29302(37)	0.50
			$a = b = 5.66221(40)$ (Å), $c = 27.36606(224)$ (Å)			
			Overall B-factor = 1.401 (Å^2)			
Refinement	Atom	Site	x	y	z	Occupancy
	Ba	6c	0	0	0.13551(85)	0.16667
	La	6c	0	0	0.29341(47)	0.16667
$Ba_2La_2MnW_2O_{12}$	Mn	3a	0	0	0	0.08333
(b)	W	6c	0	0	0.41653(86)	0.16667
	O1	18h	0.49847(95)	0.50153 (95)	0.11839(30)	0.50
	O2	18h	0.47415(88)	0.52586(88)	0.29343(38)	0.50
			$a = b = 5.72804(74)$ (Å), $c = 27.38715(384)$ (Å)			
			Overall B-factor = 1.558 (Å^2)			

= 3.19 μ_B, Figure 4.4 (c), indicating FM interactions. Magnetization data taken at 2.0 K and reported in Figure 4.4 (d) shows clear hysteresis and a magnetic saturation value of $M_S \approx 2$ μ_B. NPD measurements performed at 2 K and 20 K show definitive magnetic Bragg peaks that overlap the lattice Bragg peaks (Figure 4.5). This is clear evidence for the onset of FM LRO. Rietveld refinement of the ferromagnetic component reveals a magnetic moment of $\approx$ 2 μ_B, consistent with the value from DC magnetization. Spin orientation cannot be resolved due to the powder nature of the sample. All of the above data, including the increase of T_C under fields of C_P and χ_{DC}, the sharp peak in C_P and rapid increase χ_{DC} at 6.2 K, the positive θ_{CW}, the magnetization hysteresis, and magnetic Bragg peaks from NPD indicate that $Ba_2La_2NiW_2O_{12}$ is a spin-1 system with long range FM ordering onset at 6.2 K at zero field.

4.1.3 $Ba_2La_2MnW_2O_{12}$

$Ba_2La_2MnW_2O_{12}$ is shown to be pure phase with the space group *R-3mH* from the Rietveld refinement of the NPD pattern measured at room temperature. The refined lattice parameters are $a = b = 5.7280(4)$ Å and $c = 27.3872(38)$ Å. Detailed structural parameters are reported in Table 4.3. In Figure 4.6 (b), specific heat shows a sharp peak at $T_N = 1.7$ K, indicating the onset of LRO. Figure 4.6 (c) shows that a linear fitting of the inverse χ_{DC} from 150 to 300 K gives a negative θ_{CW} = -10.7 K and $\mu_{eff} = 5.73$ μ_B, indicating that AFM interactions are dominant.

χ_{AC} was measured both as a function of temperature under varying applied DC fields (Figure 4.6 (a)) and as a function of DC field under varying applied temperatures (Figure 4.6 (b)). Transitions were again determined from local minima in $d\chi_{AC}/dT$ and $d\chi_{AC}/d$H. Under zero field, Figure 4.6 (a) χ_{AC} as a function of temperature has no significant features, however there is a weak slope change around $T_N = 1.7$ K, consistent with the peak in C_P. Upon applying a DC field of H = 2 T, a peak appears at 1.5K and shifts to higher temperatures upon increasing DC fields before inflecting and shifting to lower temperatures with further increase, as indicated by the curved arrow in Figure 4.6 (a). Field scans at 300 mK show two slope changes around 4 T and 11 T that are accompanied by two sharp valleys in the $d\chi_{AC}/d$H curve (Figure 4.6 (c)). The minima positions at 300 mK are defined

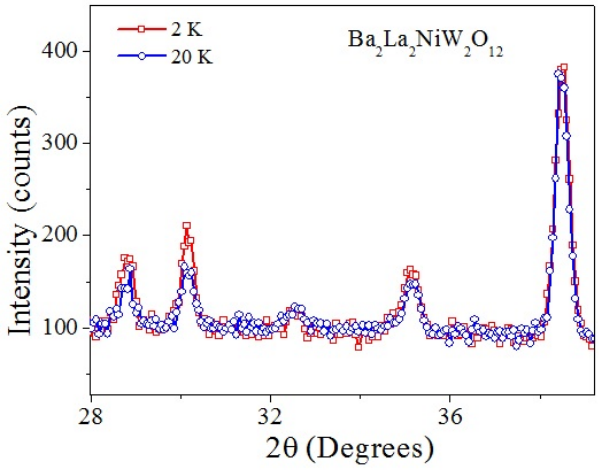

Figure 4.5: Neutron powder diffraction of $Ba_2La_2NiW_2O_{12}$ taken at 2 and 20 K [55] on HB-2A powder diffractometer. The overlap of magnetic Bragg peaks with lattice Bragg peaks is indicative of ferromagnetic long range ordering.

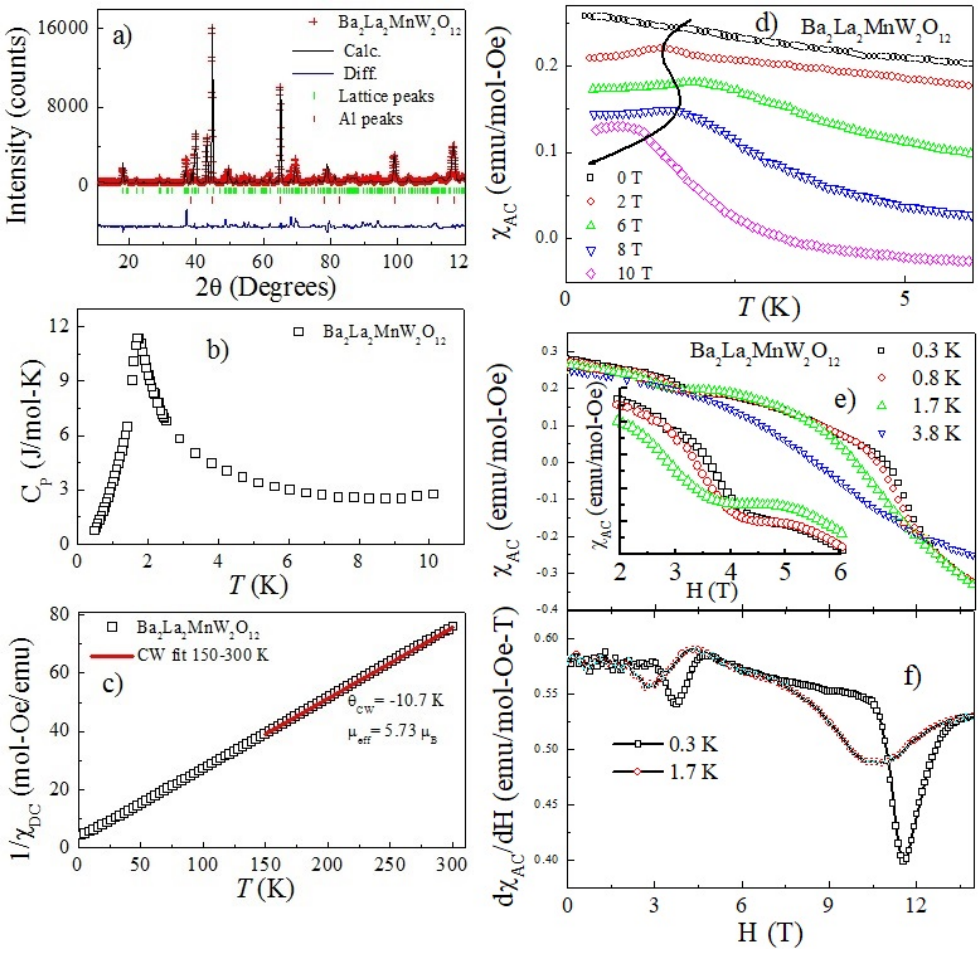

Figure 4.6: For $Ba_2La_2MnW_2O_{12}$ sample [55], (a) the Rietveld refinement of the neutron powder diffraction pattern taken at room temperature on HB-2A neutron powder diffractometer. (b) The temperature dependence of specific heat measured at zero field. (c) The inverse DC susceptibility with the solid line representing the Curie-Weiss fitting. (d) The temperature dependence of χ_{AC} under applied DC fields. (e) The DC field dependence of χ_{AC} at various temperatures. Inset: the enlargement of the data around 4 T for clarity. (f) The derivative of the field dependence of χ_{AC} at different temperatures. The local minima are used to determine transition temperatures.

as the critical fields at H_{c1} = 3.75 T and H_{c2} = 11.6 T. Upon increasing temperature, these valleys become broader and shift to lower fields before disappearing above T_N. The transition temperatures from C_P and χ_{AC} and the critical field values from χ_{AC} are combined to present the magnetic phase diagram of $Ba_2La_2MnW_2O_{12}$ shown in Figure 4.7.

4.1.4 $Ba_3LaCuReWO_{12}$

The work by our group in Subsection 4.1.1 shows that in other members of $A_4B'B_2O_{12}$, five cobalt containing compounds show FM behavior with the temperature of behavior ranging from 0.8-1.3K. $Ba_2La_2NiW_2O_{12}$ shows FM ordering at 6.2 K, and $Ba_2La_2MnW_2O_{12}$ shows AFM ordering at 1.7 K. NPD was performed on $Ba_2La_2NiW_2O_{12}$ and $Ba_2La_2MnW_2O_{12}$ and confirmed the FM ordering and 120 degree AFM ordering respectively. The FM ordering of the lower spin Co and Ni compounds and AFM ordering of the Mn compound is attributed to the competition between FM and AFM superexchange pathways. With this in mind, we look to examine another spin-1/2 isostructural compound to further our understanding of the low spin triangular lattice. While the Co and Ni compounds showed peaks in AC susceptibility at the ordering temperature, no such peak has been observed in $Ba_3LaCuReWO_{12}$ by our group, indicating a lack of long ranged ordering and possible spin liquid behavior. There have not been any previous reports on the ordering or magnetic structure of $Ba_3LaCuReWO_{12}$.

We carried out the successful synthesis of polycrystalline $Ba_3LaCuReWO_{12}$ by the standard solid-state reaction method. XRD was performed and shows a single phase of space group *R-3mH* with a = 5.6655 Å and c = 27.4685 Å (Figure 4.8 (a)). There was no resolvable site disorder evident in the XRD refinements. The Cu^{2+} ions reside on a triangular lattice that is separated from other Cu^{2+} layers by two non-magnetic (W^{6+}/Re^{7+}) and one vacant layer (Figure 4.8 (b)). DC susceptibility was taken down to 2 K and Curie-Weiss fitting from 200-300 K yields a FM θ_{CW}= 28.7 K and μ_{eff}=1.58 μ_B. No transition is visible down to 2K. Specific heat measurements taken down to 20 mK show a very broad peak with a slope change around 300 mK (Figure 4.8 (c)). This peak becomes sharper and occurs at higher temperatures under applied fields. AC susceptibility did not reveal any peak, unlike in similar Ni-containing compounds. The improved resolution from NPD is essential for reliable extraction of the bond angles to compare between FM and AFM

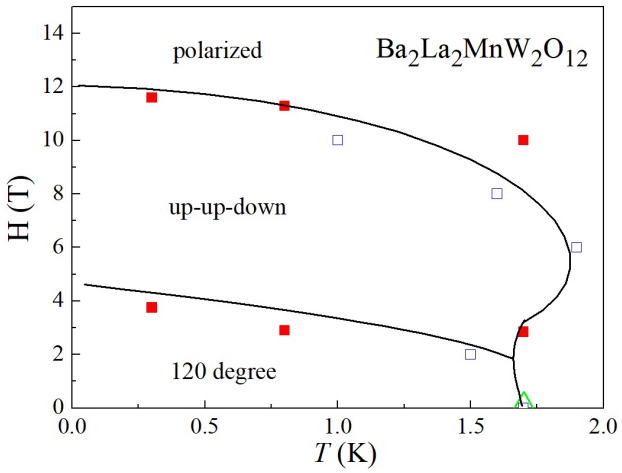

Figure 4.7: Magnetic phase diagram of $Ba_2La_2MnW_2O_{12}$ [55]. Transition temperatures were found from the temperature derivative (red solid squares), the field derivative (blue open squares) of AC, and zero-field CP measurements (green triangle). The 120 degree ordered ground state, up-up-down state, and fully polarized state are labeled. Lines are provided as a guide for the eye.

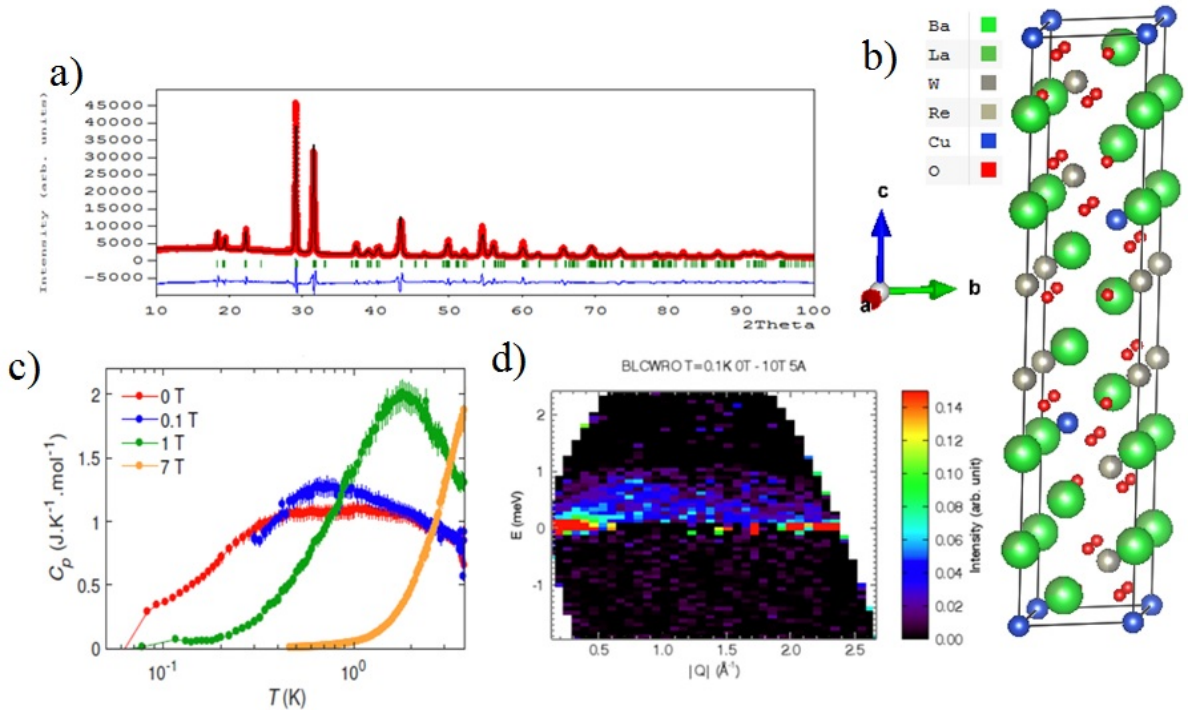

Figure 4.8: a) X-ray diffraction refinement of $Ba_3LaCuReWO_{12}$. b) Unit cell of $Ba_3LaCuReWO_{12}$ with Cu^{2+} (blue) ions residing on staggered triangular lattices. c) Specific heat showing a very broad peak with a slope change at 300 mK. d) Disk chopper time-of-flight spectroscopy data of $Ba_3LaCuReWO_{12}$ taken at National Institute of Standards and Technology using $\lambda = 5.0$ Å and subtracting the data with an applied field of 10 T from the 0 T data to isolate the coherent scattering.

members of the $A_4B'B_2O_{12}$ family. Disk chopper time-of-flight spectroscopy (DCS) inelastic scattering was taken on $Ba_3LaCuReWO_{12}$ on DCS at National Institute of Standards and Technology, but the overpowering background and strong elastic signal made it impossible to perform useful simulations with the data (Figure 4.8 (d)). In the triangular compound $Ba_8CoNb_6O_{24}$ (Section 4.2), lacking LRO possessed a similar broad peak in specific heat as seen in $Ba_3LaCuReWO_{12}$ and revealed the need for $1/S$ correction to linear spin wave theory to describe the excitations.

Four days of beam time has been allocated at the cold neutron triple-axis spectrometer (CTAX) and ORNL. This experiment is vital in answering the following questions: What are the excitations of Ba3LaCuReWO12? Does it show spin liquid behavior such as fractional excitations? Is linear spin wave theory sufficient to describe any observed excitations?

4.1.5 Discussion

The spin size of the magnetic B′ ions is a significant factor in the magnetic ground states of the studied $A_4B'B_2O_{12}$ compounds. The low spin Co^{2+} (S = 1/2) and Ni^{2+} (S = 1) containing compounds show FM behavior and ordering respectively, while the Mn^{2+} (S = 5/2) compound possesses AFM LRO. To explore this alteration of the ground state, we turn to the superexchange interactions of the B'^{2+} ions in the structure. Qualitative description of the superexchange interaction between magnetic cations is determined using the theoretical framework presented by Anderson, Goodenough, and Kanamori [65, 66, 67, 68]. For magnetic ions in an octahedral environment, the FM or AFM nature of the superexchange can be determined from the orbital configurations of the magnetic cations and the nonmagnetic, bridging anions. For the $B'O_6$ octahedra in $A_4B'B_2O_{12}$, corner sharing with BO_6 octahedra via an oxygen allows two pathways for intralayer superexchange, shown in Figure 4.9 (a). One path utilizing only the adjoining oxygens is B'^{2+}-O^{2-}-O^{2-}-B'^{2+} while the other path uses the nonmagnetic B site ions along B'^{2+}-O^{2-}-W^{6+}-O^{2-}-B'^{2+} or B'^{2+}-O^{2-}-Re^{7+}-O^{2-}-B'^{2+}. The B'^{2+}-O^{2-}-O^{2-}-B'^{2+} superexchange interaction is commonly found in other magnetic oxides where it is AFM.

To understand the superexchange interaction along the B'^{2+}-O^{2-}-B'^{7+}-O^{2-}-B'^{2+}, it is necessary to look at the nonmagnetic W^{6+} and Re^{7+} ions. These B′ ions reside on octahedral

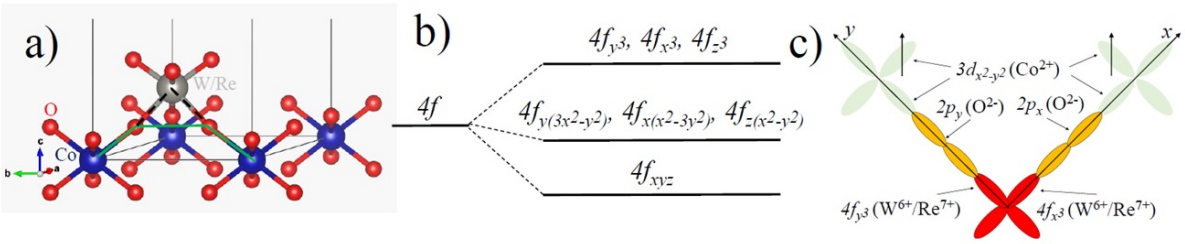

Figure 4.9: a) Pathways for ferromagnetic B′-O-B-O-B′ (black dashed line) and antiferromagnetic B′-O-O-B′ (green solid line) superexchange interactions. b) The splitting of the energy levels of $4f$ orbitals in cubic symmetry, with the highest energy levels having the same sign changes under reflection as p orbitals. c) Orbital diagram of ferromagnetic B′-O-B-O-B′ interaction with the f orbitals represented by symmetrically similar p orbitals for clarity [55].

sites where their degenerate $4f$ orbitals (the filled outermost orbitals) are split by the cubic crystal field into three groups, seen in Figure 4.9 (b). Due to the overlap of orbitals from the geometry, the orbitals with t_{1g} symmetry, f_{x^3}, f_{y^3}, and f_{z^3}, are the main contributors to the superexchange interaction. In Figure 4.9 (c), one configuration for the B'^{2+}-O^{2-}-W^{6+}-O^{2-}-B'^{2+} is shown and the case for Re is similar. We assume in this configuration that B'^{2+}, O^{2-} and W^{6+} are on the same line and there is a 90 degree bond angle for O^{2-}-W^{6+}-O^{2-}. Examining the superexchange interaction between the $d_{x^2-y^2}$ orbitals of the spins of the B'^{2+} ions, we consider spin 1 on the left B'^{2+} ion and spin 2 on the right B'^{2+} ion from Figure 4.9 (c). Here, spin 1 is transferred to the molecular orbital comprised of the p_y orbitals of the O^{2-} $2p$ orbitals and the f_{y^3} orbitals of the W^{6+} $4f$ orbitals. A coinciding transfer of the spin 2 to the molecular orbital composed of the p_x orbitals of O^{2-} and the f_{x^3} orbitals of W^{6+} ions also occurs. According to Hund's rules, the two spins residing on the f_{y^3} and f_{x^3} orbitals must be parallel. After this process, the two spins are transferred back to their respective B'^{2+} ion and form an FM superexchange interaction between the B'^{2+} ions. These two differing superexchange interactions being present in this system provides support for the ground state change being due to the competition between these interactions. For the Co- and Ni-containing ($S = 1/2$, $S = 1$ respectively), low spin compounds, the FM interactions are stronger than the AFM interaction, while for the Mn-containing (S = 3/2), high spin compound, the AFM interaction is stronger.

In order to further discuss the superexchange processes in the $A_4B'B_2O_{12}$ compounds, we look to compounds with similar symmetries. The t_{1g} symmetry of the $4f$ orbitals possesses a similar symmetry to $4p$ or $3p$ orbitals, with orientation along the corresponding x, y or z axis. Both the $4f$ and $4p$ or $3p$ change sign under reflection across the plane perpendicular to the orientation of the orbital. Thus, it is expected that similar superexchange interactions for $3d$-$2p$-$4p$ (or $3p$)-$2p$-$3d$ paths will also be FM. A similar competition between FM and AFM superexchange interactions is observed in $Ba_3CoNb_2O_9$ [20]. Along a similar path, there is a superexchange along the Co^{2+}-O^{2-}-Nb^{5+}-O^{2-}-Co^{2+} superexchange path involving the Nb^{5+} $4p$ orbitals that is FM, while the superexchange interaction along Co^{2+}-O^{2-}-O^{2-}-Co^{2+} is AFM. The FM superexchange reduces the AFM interaction, as seen by a low AFM transition temperature and a low saturation magnetic field. The reverse case is seen in

$AAg_2M(VO_4)_2$ (A=Ba, Sr; M=Co, Ni) [27], where the FM superexchange along Co^{2+}-O^{2-}-V^{5+}-O^{2-}-Co^{2+} exceeds the AFM superexchange along Co^{2+}-O^{2-}-O^{2-}-Co^{2+} and results in a FM transition.

Now we look into the effects of chemical pressure among the Co-containing samples. An increase in lattice parameters should generically decrease the exchange interactions of the system and lower the temperature at which FM behavior is seen, T_{FM}. In contrast, there is no such straightforward relation in this system. What instead occurs is that T_{FM} first increases under increased lattice parameters from the Sr_4 to Sr_2La_2 and then to the Ba_2La_2 compound (Table 4.2). After this, the trend reverses and the expected decrease of T_{FM} is seen in the Ba_3La and subsequently Ba_4 compound. It is shown in Figure 4.10 that there is no structural distortion between the high spin (S = 3/2) and low spin (S = 1/2) states of the Co^{2+} ion, indicating that there should be isostructural chemical pressure on A site substitution, even at low temperatures. Unfortunately, the available XRD resolution is unable to resolve the angle of the O-B-O bond, a key piece of information in further examination of the superexchange pathways. Neutron diffraction is the next step to pursue in order to explain the nuanced behavior of T_{FM}.

To conclude the examination of $A_4B'B_2O_{12}$ compounds, we turn to the phase diagram of $Ba_2La_2MnW_2O_{12}$. As discussed in Subection 1.3.1, a common ground state of the triangular lattice antiferromagnets (TLAFs) at zero field is the 120 degree ordered state such as in $Ba_3CoSb_2O_9$ [15] and $Ba_3BNb_2O_9$ (B = Co [20, 69], Ni [21], Mn [22]). Upon application of a magnetic field, these TLAFs consistently show a progression to a canted 120 degree, *uud*, oblique, and polarized phase. For $Ba_2La_2MnW_2O_{12}$, there is a similar trend to the magnetic phase diagram and we ascribe the 120 degree zero field ground state progressing into the canted 120 degree phase below H_{c1}, up up down phase above H_{c1}, and then polarized phase above H_{c2}. The difference compared to the general phase diagram is a lack of boundary observed between the *uud* and polarized phases, where the expected ordering into the oblique phase is expected. Due to the polycrystalline nature of the $Ba_2La_2MnW_2O_{12}$ sample, the AC measurements may lack the resolution necessary to detect this phase boundary.

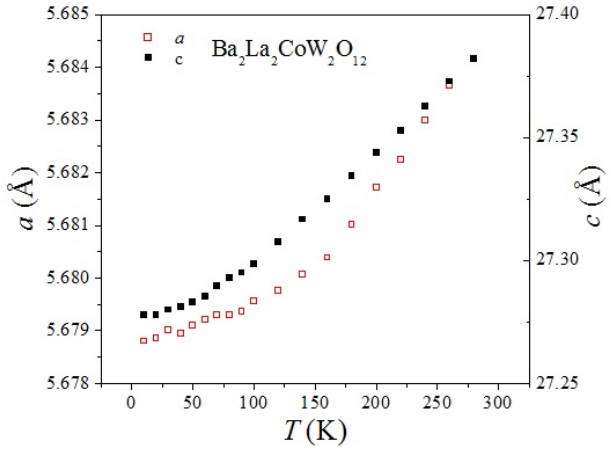

Figure 4.10: Temperature dependence of lattice parameters a and c for $Ba_2La_2CoW_2O_{12}$ [55]. No structural distortion is seen upon the transition from high spin (S = 3/2) to low spin (S = 1/2) of the Co2+ ions.

4.2 $Ba_8CoNb_6O_{24}$

Mermin and Wagner demonstrated that thermal fluctuations prevent 2D magnets from establishing long ranger ordering in their seminal 1966 paper [70], given that the interactions decay sufficiently with the distance between spins. This is an important result for condensed matter, as most interactions do decay sufficiently quickly over distance, and the breaking of the continuous spin-rotation symmetry is the focus of much research. In 1D systems the role of thermal fluctuations is instead replaced by quantum fluctuations down to $T = 0$. The Heisenberg AFM chain is one such case where LRO is instead replaced by quasi-long-range correlations [71] and fractional spin excitations [50, 72, 73]. Even with increasing dimensionality to 2D and 3D systems, Mott insulators are expected to have strong quantum fluctuation effects on the magnetic ground state. This is of particular relevance to the realization of quantum spin liquids [74, 75], as previously discussed in Subsection 1.3.1. While the QSL is an extreme case, quantum fluctuations can still have strong modification from semi-classical behavior in 2D systems that are ordered at $T = 0$. Evidence for proximity to a QSL can be seen by the elementary magnon excitations becoming weakly bonded pairs of fractional excitations. The crossover into a QSL regime is referred to as the quantum melting point (QMP), and its approach is indicated by such fractional excitations and a strong suppression of the magnitude of the ordered moment relative to its full moment.

To this end, it is natural to choose a model for studying quantum fluctuations by choosing a system with a significant reduction in the ordered moment. One such case is in spin-1/2 2D TLAF, where the non-collinear 120 degree ground state has a relative suppression of the ordered moment of more than 50% [76, 77, 78, 79, 80, 81]. In practice, TLAF materials often suffer from spin or spatial anisotropies and/or weak interlayer interactions. The lack of LRO from fluctuations of 2D Heisenberg materials is fragile in that extremely small perturbations are sufficient to introduce LRO at appreciable Néel temperature T_N due to the logarithmic relation between T_N and interlayer-coupling or exchange anisotropy [4, 5, 6, 7, 8]. This has been reported in many transition metal 2D TLAF compounds such as Cs_2CuCl_4 ($T_N = 0.62$ K [82]), $Ba_3CoSb_2O_9$ ($T_N = 3.8$ K [83]), and the $A_4B'B_2O_{12}$ compounds summarized in Table 4.2. The importance of quantum effects even below T_N is evident in

the one third magnetization plateau of the up-up-down phase under applied magnetic field [9, 18, 84]. Recent analysis of neutron scattering obtained from $Ba_3CoSb_2O_9$ [19] shows that even using sizable perturbations from the pure Heisenberg 2D TLAF [16, 83, 85, 86], the correct dispersions are not described by linear spin-wave theory (SWT). This suggests the need for novel theoretical approaches to describe both the QSL state and the qualitative properties seen in magnets with LRO near the QMP [15, 87].

Following the reasoning put forward in Section 4.1, we again look to the close-packed perovskite stacking method. The quasi-2D triple perovskite structure magnets of $A_3B'B_2O_9$ consist of triangular layers of B′ ions separated by two triangular layers of B ions. These two non-magnetic layers provide a reduction of the interlayer interactions similar to the effect of the non-magnetic and vacant layers in $A_4B'B_2O_{12}$. As a result, compounds of the $A_3B'B_2O_9$ structure have attracted much attention for their quasi-2D properties and the possibility for exotic magnetic properties. Of those studied, including $Ba_3B'Sb_2O_9$ [83, 88, 89, 90, 91, 92] and $Ba_3B'Nb_2O_9$ [69, 93, 94, 95] ($B'^{2+} = Co^{2+}$, Ni^{2+}, and Mn^{2+} with spin number 1/2, 1, and 5/2, respectively), most show the 120 degree non-collinear ordered structure. As discussed in relation to $Ba_2La_2MnW_2O_{12}$ in Subsection 4.1.5, under applied magnetic fields the 120-degree structure undergoes canting, followed by the quantum *uud* state, the oblique phase, and finally the fully polarized state. While the $Ba_3B'Nb_2O_9$ compounds exhibit multiferroic properties, of particular interest is $Ba_3CoSb_2O_9$ due to the strong quantum fluctuations occurring from the effective spin-1/2 Co^{2+} ions. Despite a large ordering temperature of $T_N = 3.8$ K [83], quantum effects remain prominent in the ordered state of $Ba_3CoSb_2O_9$ and produces the one third magnetization plateau of the *uud* phase by the order by disorder phenomena [18, 88, 89, 90, 96]. Inelastic neutron scattering (INS) on $Ba_3CoSb_2O_9$ shows spin dynamics that are not captured by SWT and suggests the approach of a QMP.

In an attempt to engineer the interactions and tune the QMP present in $Ba_3CoSb_2O_9$, we look to introduce further non-magnetic and vacant layers between the layers of $S = 1/2$ Co^{2+}. The reduced ordering temperatures in the Co-containing members of $A_4B'B_2O_{12}$ (Table 4.2) relative to $Ba_3CoSb_2O_9$ lend credence to this approach. To this end, $Ba_8CoNb_6O_{24}$ possesses similar triangular layers of magnetic CoO_6 octahedral stacked along the hexagonal c axis yet have six non-magnetic layers and one vacant layer between Co layers. The structure and

stacking are shown in Figure 4.11 (a). The intralayer Co–Co distance is 5.86 Å and the interlayer Co–Co distance is 7.23 Å of $Ba_3CoSb_2O_9$ [83] and yields an interlayer magnetic exchange interaction, J', that is ∼5% in the intralayer exchange J [16]. In $Ba_8CoNb_6O_{24}$ the intralayer Co–Co distance of 5.79 Å and interlayer Co–Co distance of 18.90 Å [97] shows comparable intralayer Co–Co distance but dramatically increased interlayer Co–Co distances. While the spin anisotropy is difficult to predict, this structure with a chosen stacking sequence is expected to enhance the 2D nature of the magnetic properties of $Ba_8CoNb_6O_{24}$.

We synthesized polycrystalline samples of $Ba_8CoNb_6O_{24}$ via the standard solid state synthesis method. Stoichiometric amounts of $BaCO_3$, $CoCO_3$, and Nb_2O_5 were combined and ground with an agate mortar and pestle, pressed into pellets, and annealed at 1500 C for 48 hours with one intermediate grinding. NPD measured at $T = 0.3$ K with $\lambda = 1.54$ Å (Figure 4.11 (b)) was analyzed by Rietveld refinement yielding $a = 5.7902(2)$ Å and $c = 18.9026(3)$ Å, in agreement with previous work [97]. Detailed structural parameters are summarized and Table 4.4 and show limited disorder (< 2 %) between the Co and Nb sites, confirming the success of the intercalation approach. There is no significant difference between NPD patterns taken at $T = 0.3$ K and 2.0 K, with no additional Bragg peaks or broadening of or change in intensity of the existing Bragg peaks [98]. This suggests the lack of any structural transition or LRO down to $T = 0.3$ K.

Shown in Figure 4.11 (c), measured χ_{DC} on $Ba_8CoNb_6O_{24}$ shows no significant feature indicating the onset of LRO nor evidence for spin freezing, such as strong field dependence, down to $T = 1.8$ K. As in the Co containing $A_4CoB_2O_{12}$ compounds, there is a slope change in $1/\chi_{DC}$ indicative of the transition from a high-spin state ($S = 3/2$) to a low-spin state ($S = 1/2$). This is seen in other compounds containing Co^{2+} ions in an octahedral environment such as $ACoB_3$ (A = Cs, Rb, B = Cl, Br) [12]. Linear Curie-Weiss fitting of the high temperature range from 200 to 350 K yields $\mu_{eff} = 5.01(2)$ μ_B and $\theta_{CW} = -25.2(3)$ K while fitting of the low temperature range from 1.8 to 30 K yields $\mu_{eff} = 3.89(2)$ μ_B and $\theta_{CW} = -4.23(1)$ K. DC magnetization taken at $T = 1.8$ K shows the saturation of the spins above $\mu_0 H_s \approx 4$ T and is presented in Figure 4.11 (d). Linear fitting of the magnetization between $\mu_0 H = 5$ T to 7 T to reveals a Van Vleck paramagnetic contribution of 0.023 $\mu_B.T^{-1}$ per Co^{2+} and a saturation magnetization $M_s = 1.87$ μ_B. This saturation value is comparable to

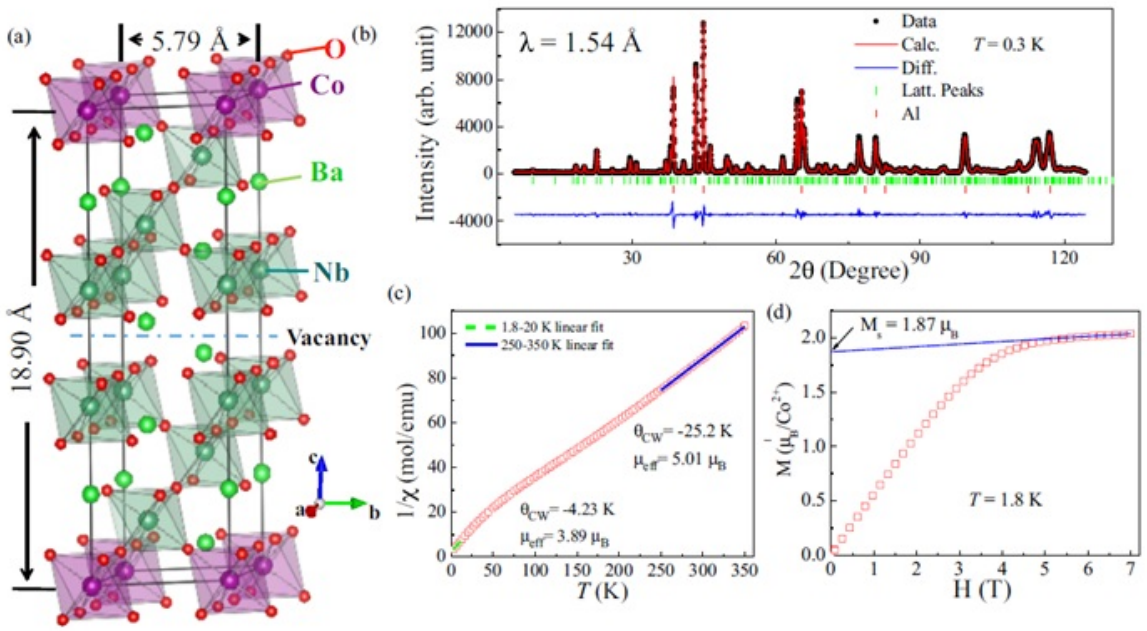

Figure 4.11: (a) The stacked layer structure of $Ba_8CoNb_6O_{24}$ with Co2+ ions sitting on a triangular lattice. (b) Rietveld refinement of the neutron powder diffraction pattern measured with $\lambda = 1.54$ Å at $T = 0.3$ K at HB-2A. (c) Temperature dependence of the inverse DC magnetic susceptibility and linear Curie-Weiss fits. (d) DC magnetization measured at $T = 1.8$ K. Linear fitting extrapolation of the magnetization above the saturation field to extrapolate saturation moment (blue solid line) [56].

Table 4.4: Structural parameters for $Ba_8CoNb_6O_{24}$ at 0.3 K [56].

Refinement	Atom	Site	x	y	z	Occupancy
$\lambda = 1.5404$ Å	Ba(1)	2c	0	0	0.18771(36)	1/6
RF-factor = 2.44	Ba(2)	2d	1/3	2/3	0.06126(52)	1/6
Bragg R-fct = 3.21	Ba(3)	2d	1/3	2/3	0.45478(41)	1/6
P-3m1	Ba(4)	2d	1/3	2/3	0.68149(32)	1/6
	Co	1a	0	0	0	0.084(2)
	Nb(1)	2c	0	0	0.38677(30)	0.166(1)
	Nb(2)	2d	1/3	2/3	0.25272(33)	0.166(1)
	Nb(3)	2d	1/3	2/3	0.87707(33)	0.166(1)
	O(1)	6i	0.16937(49)	0.30685(19)	0.30685(19)	1/2
	O(2)	6i	0.16413(38)	0.83577(38)	0.56995(19)	1/2
	O(3)	6i	0.17068(57)	0.82922(57)	0.93424(26)	1/2
	O(4)	6i	0.49774(61)	0.50216(61)	0.18738(14)	1/2
			$a = 5.7902(2)$ (Å), $c = 18.9026(3)$ (Å)			
			Overall B-factor = 0.093(8) (Å^2)			

that found in $Ba_3CoSb_2O_9$ and corresponds to a powder-averaged gyromagnetic ratio $g = 3.84$ for the effective S = 1/2 ground state.

Examination of AC magnetic susceptibility to lower temperatures of $T = 0.3$ K reveals no sharp features down to 0.3 K, displayed in Figure 4.12 (b), and similar behavior to χ_{DC}. There is instead a broad peak centered at $T = 0.6$ K. We ascribe this peak to the onset of short-ranged magnetic correlations and not LRO. Heat capacity measurements shown in Figure 4.12 (c) confirm the presence of magnetic correlations below $T \approx 1$ K. To isolate the magnetic contribution, C_m, the lattice contribution , C_L, was subtracted using the iso-structural but non-magnetic compound $Ba_8ZnTa_6O_{24}$ [98]. The plot of $C_m(T)$ reveals a broad peak centered around $T = 0.8$ K and no sharp feature down to $T = 0.06$ K. The small increase in C_m at extremely low temperatures is attributed to the nuclear spins. This suggest there is no magnetic phase transition down to $T \leq 0.06$ K. The change in magnetic entropy, $\Delta S_m = S_m(T) - S_m(T_{min})$, was calculated by integrating $C_m(T)/T$ from $T_{min} = 0.06$ K to $T \leq 8$ K [98]. By $T = 8$ K the release of entropy reaches 5.32 $J\,mol^{-1}\,K^{-1}$, a value similar to that expected from a Kramers doublet ground-state, $R \ln 2 = 5.76$ $J\,mol^{-1}\,K^{-1}$.

Now we look to explain the origin of the broad peak observed in $C_m(T)$. It is useful to turn to theoretical modeling of the quasi-2D antiferromagnetic Heisenberg model. Quantum Monte Carlo studies on the quasi-2D AFM Heisenberg model have shown that small interlayer exchange interactions, as low as $J'/J = 2\times10^{-4}$ [99], produce a sharp peak in $C_m(T)$. Further reduction in the interlayer coupling causes the sharp peak to disappear, leaving behind a broad peak as the one observed here in $Ba_8CoNb_6O_{24}$. This is indicative of the practically ideal 2D nature of the magnetism present. Comparing to the previously reported $Ba_3CoNb_2O_9$ [69] in Figure 4.13 (b), the increase in separation of the magnetic layers from two non-magnetic to six non-magnetic and one vacant layer removes the sharp peaks in $C_m(T)$. The two sharp peaks in $Ba_3CoNb_2O_9$ at $T_{N1} = 1.10$ K and $T_{N2} = 1.36$ K indicate two subsequent phase transitions resulting from easy-axis anisotropy [69]. At similar energy scales at ≈ 1 K, there is only the single broad peak in $Ba_8CoNb_6O_{24}$ indicating no features due to interlayer coupling nor anisotropy.

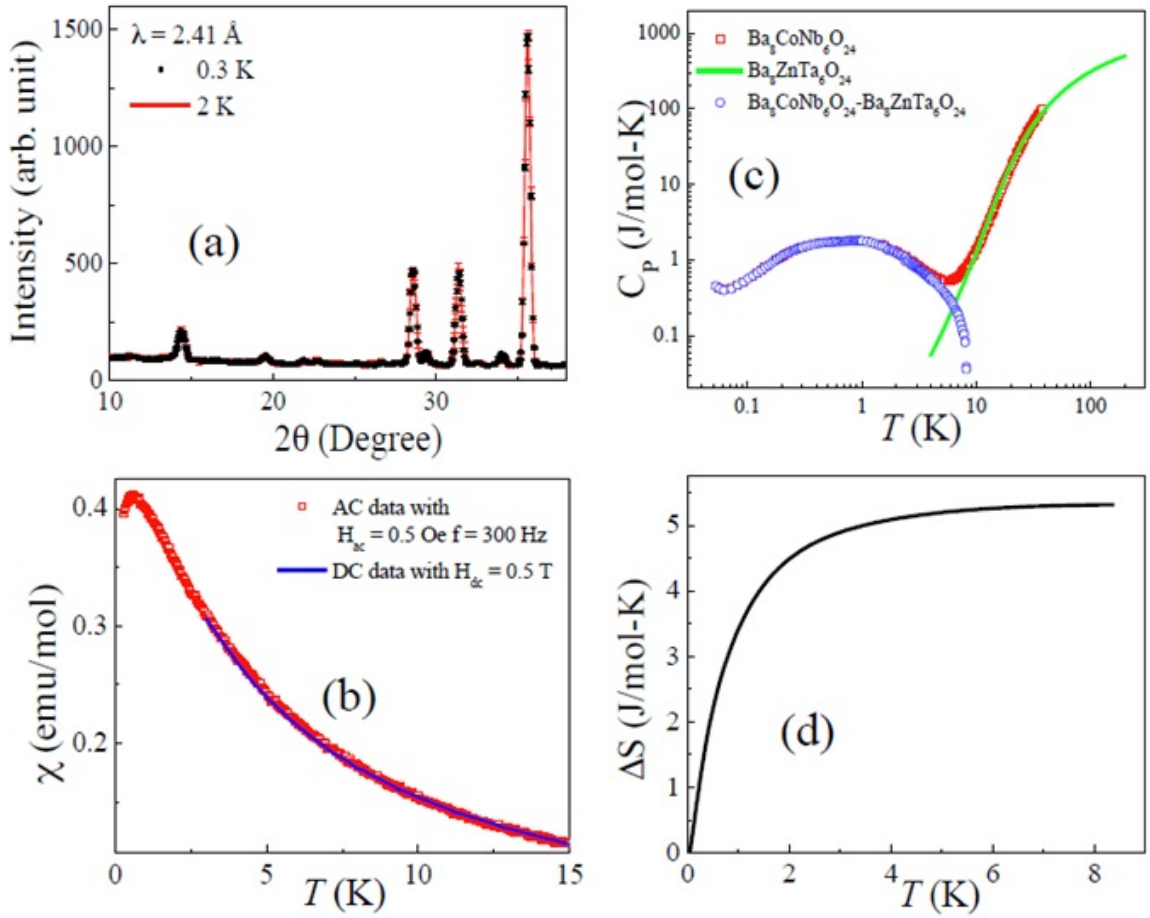

Figure 4.12: (a) The neutron powder diffraction patterns for $Ba_8CoNb_6O_{24}$ taken with $\lambda = 2.4111$ Å at 0.3 and 2 K at HB-2A. (b) The magnetic susceptibility for $Ba_8CoNb_6O_{24}$. Both DC and scaled AC data are shown. (c) The specific heat for $Ba_8CoNb_6O_{24}$, isostructural yet non-magnetic $Ba_8ZnNb_6O_{24}$, and the difference taken to isolate the magnetic contribution. (d) The magnetic entropy calculated from integration of the magnetic contribution C_P/T [56].

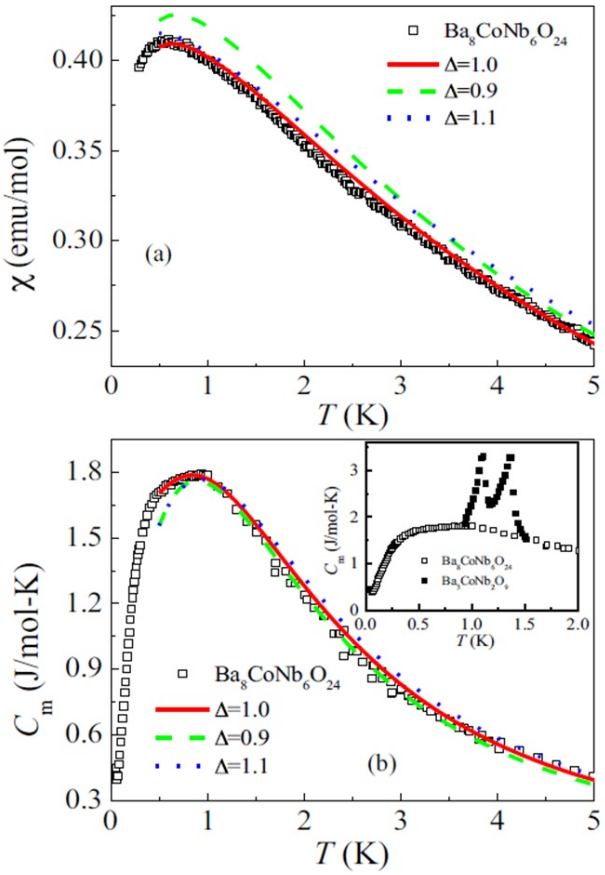

Figure 4.13: For $Ba_8CoNb_6O_{24}$ [56], (a) the temperature dependence of the magnetic AC susceptibility and corresponding high-temperature series expansion simulations using the two-dimensional spin-1/2 triangular-lattice antiferromagnet with XXZ exchange anisotropy. Anisotropy parameter values of $\Delta = 0.9$, 1.0, and 1.1 are used and simulations run down to a temperature of 0.5 K using Padé approximants of order [6,6]. The measurements are obtained with an AC excitation field of amplitude 0.5 Oe and frequency 300 Hz, and matched to the DC susceptibility below $T = 15$ K by an overall T-independent rescaling factor (Figure 4.12 (b)). (b) The temperature dependence of the magnetic contribution to the specific heat and high-temperature series expansion simulations as described in part (a). Inset: Comparison to the magnetic specific heat of $Ba_3CoNb_2O_9$ [69] to indicate lack of similar long-range ordering behavior.

4.2.1 High Temperature Series Expansion

In order to probe to lower temperatures than those available by χ_{DC}, we turn to AC susceptibility measurements. Our choice of low frequency and small field values yield the same temperature trends in χ_{AC} as those of χ_{DC}. To this end, χ_{AC} measurements were performed using an AC field of 0.5 Oe with frequency 300 Hz to measure down to 0.3 K. A simple scaling factor allowed for easy matching of high temperature χ_{DC} data taken down to 1.8 K with low temperature χ_{AC} data as shown in Figure 4.12 (b). As there is essentially identical behavior seen in the overlap of these data sets, scaled χ_{AC} was used in all simulations and fittings to allow for examinations down to 0.3 K. Scaled χ_{AC} was assigned units of emu/mol as to maintain continuity with χ_{DC}.

To examine the magnetic contribution of specific heat in $Ba_8CoNb_6O_{24}$, a non-magnetic lattice standard of $Ba_8ZnTa_6O_{24}$ was used to remove the lattice contribution (Figure 4.12 (c)). This is particularly useful as high temperature series expansion (HTSE) only provides the magnetic contribution of C_{P}. To this end, C_{m} data with the lattice subtracted is used in fitting and comparisons. The magnetic entropy calculated by integrating C_{P}/T between 0.06 and 8 K of the magnetic C_{m} saturates at $\Delta \mathrm{S} = 5.32$ J/mol-K. This is close to the expected value of Rln(2)= 5.76 J/mol-K for a spin-1/2 system.

For 2D Heisenberg triangular lattice antiferromagnets (TLAFs), the temperature dependence of both $\chi(T)$ and $C_{\mathrm{m}}(T)$ has been well examined using high temperature series expansion [100, 101, 102, 103] up to 12th order [53]. In order to examine anisotropy in $Ba_8CoNb_6O_{24}$, we look to extend current HTSE work to the XXZ Hamiltonian,

$$\mathcal{H} = J \sum_{\langle i,j \rangle} (S_i^x S_j^x + S_i^y S_j^y + \Delta\, S_i^z S_j^z), \tag{4.1}$$

where $\langle i, j \rangle$ denotes the nearest-neighbor spins. We have examined HTSE for isotropic ($\Delta = 1.0$), easy-plane ($\Delta = 0.9$), and easy-axis ($\Delta = 1.1$) models [98]. HTSE was used to calculate exchange constants and exchange anisotropy for $Ba_8CoNb_6O_{24}$. Coefficients a_n and c_n of the following equations

$$\frac{\ln Z}{N} = \sum_{n=0} a_n x^n \tag{4.2}$$

$$\frac{k_B T\chi}{(g\mu_B)^2} = \sum_{n=0} c_n x^n \tag{4.3}$$

have been previously reported up to 12th order [53] for the spin-1/2 isotropic Heisenberg TLAF, so we have computed the coefficients for the anisotropic spin-1/2 Heisenberg TLAF for $\Delta = 0.9$, 1.1 (see Table 4.5). This allows for the calculation of $\chi(T)$ directly and $C_{\rm m}(T)$ from the temperature derivative of the total energy of the system calculated from partition functon Z. For fitting of $C_{\rm P}$, the relation was calculated from the T-derivative of the free energy given in Equation 4.2 while χ was calculated directly from Equation 4.3. As shown in Figure 4.13, all of these cases were fitted to (a) $\chi(T)$ and (b) $C_{\rm m}(T)$. The fitting for the isotropic case yields the best fit. For both $\chi(T)$ and $C_{\rm m}(T)$ below $T = 5$ K, the fitting yields $J = 0.144$ meV for $\Delta = 1.0$ with a fitting error-bar on J smaller than 10^{-3} meV. Using a fixed value of J, the fitting quality deteriorates as Δ deviates from 1.0. The peak for $\chi(T)$ moves to a higher magnitude while the peak in $C_{\rm m}(T)$ moves to a lower magnitude.

Fittings to low temperatures using the bare coefficients a_n from Equations 4.2 lead to low-temperature divergence. This can be avoided by using approaches such as the ratio method, integrated differential approximants, or Padé approximants [99]. For our studies, we used the Padé approximant approach as originally used by Elstner *et al.* [53]. Similar to Elstner *et al.*, we chose order $[m = 6, n = 6]$ as given by Equation 4.4. The reasoning is two-fold, first using some off-diagonal approximants such as [7, 5] and [5, 7] produces non-physical divergences at $T = J/k_{\rm B}$. Second, choosing diagonal orders of [n, n] results in a low-temperature convergence to a non-zero, finite value. After examining multiple approximants, Padé approximants of order [6,6] as used by Elster *et al.* produced the most physically meaningful results below $T = J/k_{\rm B}$.

$$R(x) = \frac{\sum_{j=0}^{m} a_j x^j}{1 + \sum_{k=1}^{n} a_k x^k} \tag{4.4}$$

4.2.2 Inelastic Scattering

Now that we have provided strong evidence for the purely 2D nature and adherence to the isotropic spin-1/2 Heisenberg model in $Ba_8CoNb_6O_{24}$, we examine the fundamental spin

Table 4.5: High temperature series expansion coefficients for anisotropy coefficients $\Delta = 0.9, 1.1$ [56]

n	$\Delta = 0.9$		$\Delta = 1.1$	
	$\ln Z$	χ	$\ln Z$	χ
0	0.693147180560E+00	0.250000000000E+00	0.693147180560E+00	0.250000000000E+00
1	0.000000000000E+00	-0.135000000000E+01	0.000000000000E+00	-0.165000000000E+01
2	0.421500000000E+01	0.457500000000E+01	0.481500000000E+01	0.757500000000E+01
3	-0.275800000000E+01	-0.928600000000E+01	-0.336200000000E+01	-0.267540000000E+02
4	-0.110157250000E+02	0.735865000000E+01	-0.143937250000E+02	0.833306500000E+02
5	0.227150400000E+02	0.813502200000E+01	0.316609600000E+02	-0.274087222000E+03
6	0.555289564000E+02	-0.432566133333E+01	0.830983377333E+02	0.971839778667E+03
7	-0.230309437387E+03	0.309929443029E+02	-0.367686192480E+03	-0.315219402327E+04
8	-0.251495874650E+03	-0.905870806367E+03	-0.428893232275E+03	0.868118706817E+04
9	0.237935023053E+04	0.359542189692E+04	0.433229044400E+04	-0.243590877456E+05
10	-0.490854208087E+02	-0.374861931449E+02	-0.625397496451E+02	0.877627224099E+05
11	-0.239243887884E+05	-0.309077579057E+05	-0.498804497089E+05	-0.317811658164E+06
12	0.262699694109E+05	0.180327243359E+05	0.582734814011E+05	0.840953315702E+06

excitations. Inelastic neutron scattering provides a powerful tool to this end, as described in Section 2.3, due to the ability to probe the momentum transfer Q and energy transfer E of magnetic correlations. The powder-averaged intensity at $T = 0.3\,\mathrm{K}$ is presented in Figure 4.14 (a) with additional temperatures of $0.05\ \mathrm{K} \leq T \leq 5\ \mathrm{K}$ presented in Figure 4.15. There is no significant change in the INS upon further cooling below 0.3 K. Looking at the momentum dependence, strong ridges in intensity appear $Q \approx 0.7\ \mathrm{\AA}^{-1}$ with additional, but weaker, ridges appearing at 1.5 $\mathrm{\AA}^{-1}$ and 2.0 $\mathrm{\AA}^{-1}$. The low-energy signal at $E \leq 0.1$ meV is broader than the instrumental resolution of the data taken at National Institute of Standards at Technology using the disk chopper spectrometer (DCS). This suggests the lack of true static order and that, instead, spin correlations are short-ranged. Turning to energy dependence, the main signal reveals that the excitations are gapless and extend up to 0.35 meV. A weaker signal extends up to $E = 0.45$ meV.

In order to examine the dynamic magnetic correlations, we turn to modeling using SWT at $T = 0$. The addition of the $1/S$ correction [104] is shown in 4.14 (b) while the linear spin wave theory (LSWT) results [105] are shown in 4.14 (c). Based off of the similarities to $Ba_3CoNb_2O_9$ and other spin-1/2 TLAF compounds, the ground state at $T = 0$ is assumed to be the 120 degree magnetic structure. The E-integrated scans, Figure 4.14 (d), and Q-integrated scans, Figure 4.14 (e), show good agreement between the INS measurements and the powder-average of $1/S$-SWT predictions. It is clear that SWT with $1/S$ correction model provides better agreement with the data than the LSWT model. The most significant improvement results from the inclusion of longitudinal spin fluctuations using the $1/S$ correction. Both a high-energy continuum known as two-magnon scattering and a reduction in the ordered moment due to quantum fluctuations are reflections of these excitations. The strong quantum fluctuations are supported by the lack of significant temperature dependence for the low energy $E \geq 0.1$ meV magnetic scattering below $T = 0.5$ K, as shown in Figure 4.14 (f).

Using the results of the fitting from HTSE presented in Subsection 4.2.1, the nearest neighbor exchange interaction of $J = 0.144$ meV was used with the isotropic Hamiltonian for both SWT with $1/S$ correction and LWST simulations. The LSWT simulation was carried out using SpinW program [105]. In order to powder average the resulting spectrum,

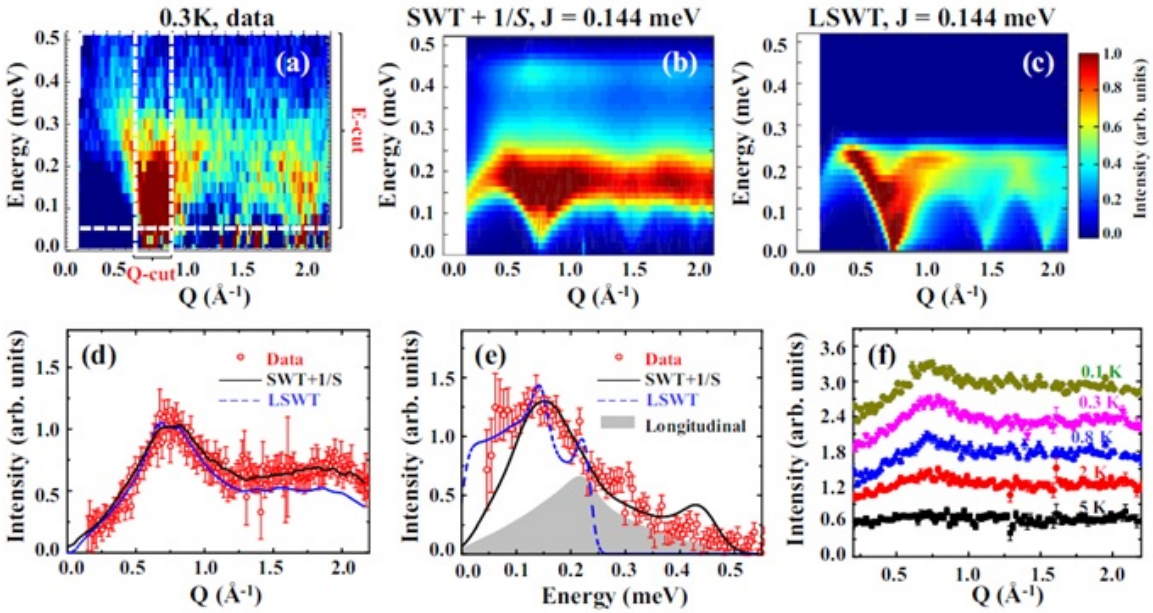

Figure 4.14: For $Ba_8CoNb_6O_{24}$ [56], (a) the powder-averaged inelastic neutron scattering spectra collected at $T = 0.3$ K. Data collected at $T = 10$ K was subtracted as background. Calculated neutron scattering intensity using $J = 0.144$ meV and (b) nonlinear spin wave theory with $1/S$ correction and (c) linear spin wave theory. The calculated intensities were convoluted by Gaussian profiles using full width at half maximum parameters of $E = 0.025$ meV and $Q = 0.015$ Å as an approximation of instrumental resolution. Comparison between experiment (red dots), $1/S$-spin wave theory (solid black line), and linear spin wave theory (dashed blue line) as (d) energy-integrated ($0.05 \leq E \leq 0.52$ meV) and (e) momentum-integrated ($0.6 \leq Q \leq 0.9$ Å) cuts. The longitudinal (two-magnon) contribution to the scattering intensity using nonlinear spin wave theory with $1/S$ correction is shown in the shaded (gray) region. The high-energy bump around $E = 0.45$ meV in (e) is an artifact of our $1/S$ approximation [104]. (f) The temperature dependence of the energy-integrated intensity of (d). The graphs at each temperature have been displaced by an intensity of 0.6 each time for clarity. The error bars correspond to one standard error.

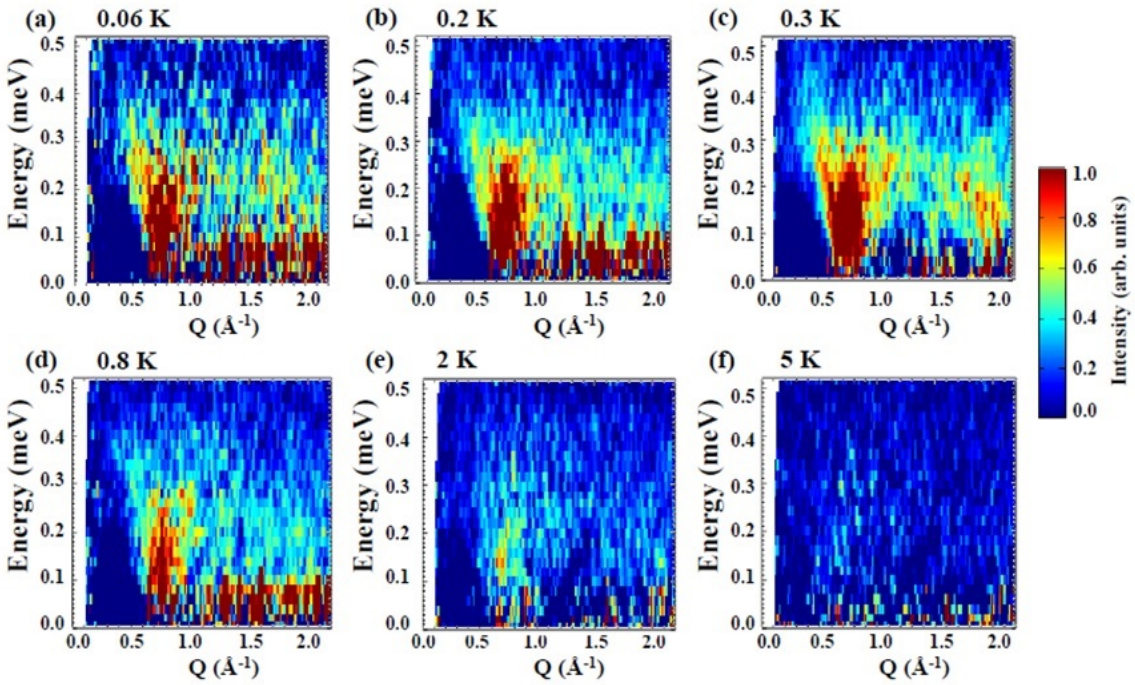

Figure 4.15: Inelastic neutron scattering spectra for $Ba_8CoNb_6O_{24}$ at various temperatures. The spectra collected at $T = 10$ K was used as the background and has been subtracted from each data set to isolate magnetic contributions [98].

a simple Monte Carlo integration was employed with sampling size for each Q-E point set to 10^5. SWT with $1/S$ correction was calculated based on the previous work by Mourigal *et al.* [104]. All numerical integrations, including the powder average, were carried out using the adaptive multidimensional integration (cubature) algorithm with the maximum number of integrated points set to 2×10^3. Results for LWST and SWT with $1/S$ correction were both convoluted with the estimated instrumental energy resolution of $\Delta E = 0.025$ meV and Q resolution of $\Delta Q = 0.015$ Å^{-1}. These resolution parameters were approximated with a fitting of the nuclear peak widths in the INS data. Additional spline interpolation was used to reduce the simulated results to the same Q-E grid as the measured spectra. This allows for easier comparison between the datasets. All LWST and SWT with $1/S$ correction simulations presented here were carried out by Luwei Ge.

4.2.3 Discussion

For the practically ideal 2D compound $Ba_8CoNb_6O_{24}$, it is beneficial to compare the excitations present with those in the quasi-2D compound $Ba_3CoSb_2O_9$ [88, 89, 90]. In $Ba_3CoSb_2O_9$, there is a interlayer interaction strength of $J' = 0.05\ J$ and anisotropy of $\Delta \approx 0.9$ where Δ is the anisotropy parameter of the XXZ model described in Equation 4.1. In both compounds, structurally similar triangular layers of magnetic Co^{2+} possess comparable Co–Co bond lengths. However, $Ba_3CoSb_2O_9$ posseses an ~ 2.0 meV in-plane excitation bandwidth that is an order of magnitude larger than that observed in $Ba_8CoNb_6O_{24}$ of ~ 0.18 meV. Put in units of the interaction strength J, the bandwidths of $W \approx 1.18\ J$ and $W \approx 1.24\ J$ in $Ba_3CoSb_2O_9$ and $Ba_8CoNb_6O_{24}$ respectively are comparable, as seen in Figure 4.14 (b). There is significant difference in that $Ba_3CoSb_2O_9$ possesses LRO below $T_N = 3.7$ K $\sim 0.19J$ while $Ba_8CoNb_6O_{24}$ shows no magnetic LRO down to $T = 0.06$ K $\sim 0.04J$. The suppression of T_N/J by a factor of at least four between the compounds indicates the reduction of both inter-plane and anisotropic exchange interactions. This suppression is especially pronounced due to the logarithmic relation between T_N and the magnitude of both J' and Δ [4, 5, 6, 7, 8].

All of the data collected consistently supports that $Ba_8CoNb_6O_{24}$ is a practically ideal 2D isotropic Heisenberg TLAF. This is a unique realization of the lack of ordering predicted by the Mermin and Wagner theorem for 2D triangular compounds. While recent studies showing

the non-perturbative effects of quantum fluctuations on magnetic excitations [19], the strong 2D behavior of $Ba_8CoNb_6O_{24}$ presents a particularly suited candidate to study these effects. This allows for the testing of theoretical predictions that can challenge the existing semi-classical approaches to the dynamic responses in frustrated quantum AFMs. Looking forward, this successful realization of materials engineering by intercalating non-magnetic and vacant layers between magnetic layers provides a method for reducing dimensionality. Further examination of layered systems using a similar approach presents may reveal new physical phenomena.

4.3 $Ba_8MnNb_6O_{24}$

With the success in synthesizing a practically ideal 2D triangular lattice magnet in $Ba_8CoNb_6O_{24}$ via the reduction of both interlayer interaction strength and anisotropy, we again look to manipulate the spin magnitude on an isostructural triangular lattice compound. To further examine the behavior of TLMs, we look to recreate the spin substitution that proved successful in the $A_4B'B_2O_{12}$ family. To this end, we replace the effective spin-1/2 Co^{2+} ions with spin-5/2 Mn^{2+} ions. This will reduce the roles of quantum fluctuations and the large spin-5/2 is expected to behave as a classical spin. The triple perovskite structures of $Ba_3B'Nb_2O_9$ and $Ba_3B'Sb_2O_9$ show the flexibility for ion doping with B'^{2+} = Co, Ni, and Mn [69, 83, 88, 89, 90, 91, 92, 93, 94, 95]. The majority of these structures possess a 120 degree ordered ground structure and, under an applied field, change into the *uud* magnetization plateau, followed by the oblique phase before full polarization.

We have already seen in Section 4.2 that the addition of four addition non-magnetic and one vacant layer between the magnetic layers from $Ba_3CoSb_2O_9$ to $Ba_8CoNb_6O_{24}$ reduced the interlayer interaction J′ from $\sim$ 5% to a negligible contribution and the anisotropy from $\Delta \sim 0.9$ to the isotropic ($\Delta = 1$) case. This was accompanied by a minor change in intralayer Co–Co distances from 5.86 Å to 5.79 Å but a much more drastic change in interlayer Co–Co distances from 7.23 Å to 18.90 Å [83, 97]. For the Mn-containing compounds, we start with $Ba_3MnNb_2O_9$. This quasi-2D TLAF possesses weak easy-axis anisotropy. Upon application of magnetic field, as expected for these triple perovskites,

$Ba_3MnNb_2O_9$ undergoes an evolution from the 120 degree ordered ground state into the *uud*, oblique, and finally polarized phases. We look to examine the similarities and differences between the low spin (S-1/2) compounds of $Ba_3CoSb_2O_9$ and $Ba_8CoNb_6O_{24}$ with those of high spin (S-5/2) compounds of $Ba_3MnNb_2O_9$ and $Ba_8CoNb_6O_{24}$.

We prepared polycrystalline samples of $Ba_8MnNb_6O_{24}$ by the standard solid state reaction method. Stoichiometric amounts of $BaCO_3$, MnO, and Nb_2O_5 were ground in agate mortars, pressed into pellets, and annealed for 20 hours at temperatures of 1525 C and 1600 C using an inert argon atmosphere. Intermediate grinding was carried out between the two annealings.

The polycrystalline sample of $Ba_8MnNb_6O_{24}$ was shown to be a single phase of the space group *P-3m1* by Rietveld refinement of the NPD pattern measured at 10 K with a wavelength of $\lambda = 1.5405$ $\mathring{A}$, as shown in Figure 4.16 (b). The refined lattice parameters are $a = b =$ 5.8070(1) and $c = 18.9465(3)$ Å. Detailed structural parameters are presented in Table 4.6. This confirms the isostructural nature of $Ba_8MnNb_6O_{24}$ with $Ba_8CoNb_6O_{24}$, indicating six non-magnetic and one vacant layer between each layer of Mn^{2+} ions, as shown in Figure 4.16 (a). The intralayer Mn–Mn distance of 5.81 Å is comparable to those seen in the Co containing compounds. The large interlayer distance of 18.91 Å [97] in $Ba_8MnNb_6O_{24}$ ensures that the interlayer interactions are negligible.

Magnetic DC susceptibility for $Ba_8MnNb_6O_{24}$ is reported in Figure 4.17 and χ_{DC} shows no magnetic ordering down to 1.8 K. Linear Curie-Weiss fitting, shown in Figure 4.16 (a), of the inverse χ_{DC} from 100 - 350 K yields an effective magnetic moment of $\mu_{eff} = 6.04$ μ_B and a Cure-Weiss constant of $\theta_{CW} = -10.7$ K. The negative θ_{CW} is indicitave of an AFM exchange interaction and the obtained effective moment agrees well with the theoretically calculated value for spin-only *S*-5/2 of 5.93 μ_B [106]. DC magnetization data collected at $T =$ 0.6 K and shown in in Figure 4.17 (b) saturates above $\sim \mu_0 H_s \approx 22.5$ T with a saturation moment of 5.5 μ_B. There are no obvious valleys or peaks in the first derivative of χ_{DC} that would indicate possible spin state transitions. The saturation moment of 5.5 μ_B corresponds with a powder-averaged gyromagnetic ratio $g = 2.1$.

AC susceptibility for $Ba_8MnNb_6O_{24}$ is presented in Figure 4.18 and was used to measure to lower temperature magnetic properties down to 0.3 K. With no applied DC field, χ_{AC}

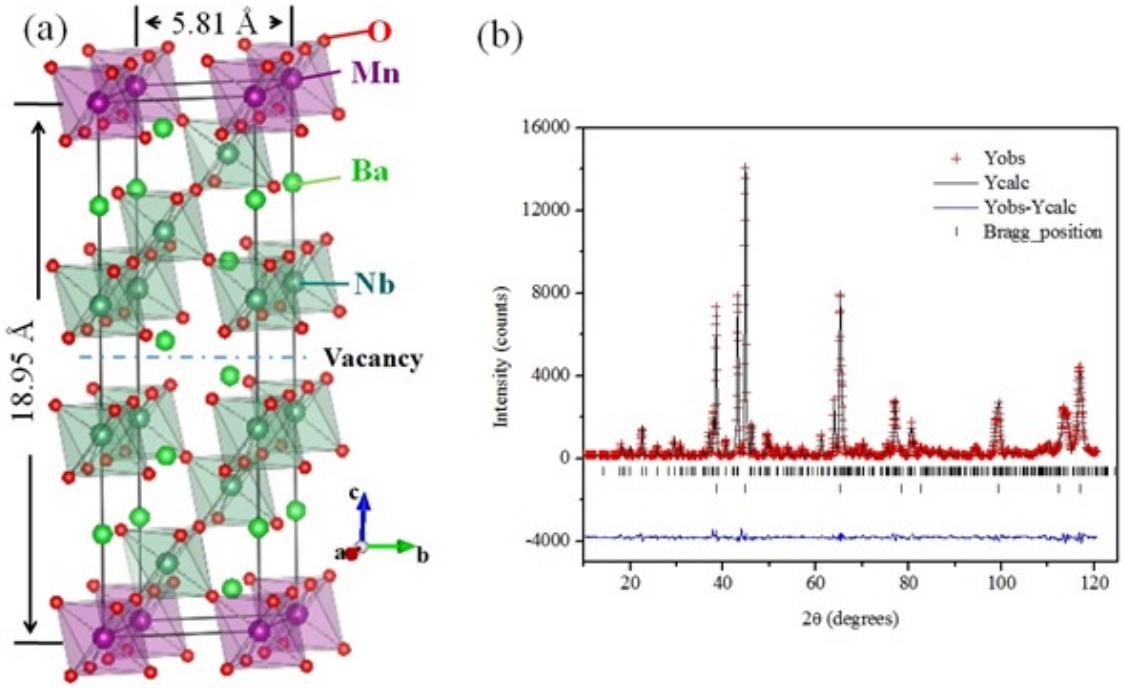

Figure 4.16: (a) Stacked layer structure of $Ba_8MnNb_6O_{24}$ of space group *P-3m1* with Mn^{2+} ions sitting on a triangular lattice. (b) Rietveld refinement of the neutron powder diffraction pattern measured at $T = 10$ K with $\lambda = 1.54$ Å. Red crosses are the measured intensity, the black line is the calculated intensity, and the blue line is the difference. Bragg Peak locations are indicated by tick marks with red indicating reflections from the sample and green indicating aluminum.

Table 4.6: Structural parameters for $Ba_8MnNb_6O_{24}$ at 10K (space group *P-3m1*) determined from refined XRD measurements.

Refinement	Atom	Site	x	y	z	Occupancy
$Ba_8MnNb_6O_{24}$ $\chi^2 = 2.21$ (a)	Ba1	2c	0	0	0.18732(84)	0.16666
	Ba2	2c	1/3	2/3	0.05867(120)	0.16666
	Ba3	2c	1/3	2/3	0.44997(89)	0.16666
	Ba4	2c	1/3	2/3	0.68171(92)	0.16666
	Mn	1a	0	0	0	0.08333
	Nb1	2c	0	0	0.38767(61)	0.16667
	Nb2	2d	1/3	2/3	0.25790(82)	0.16667
	Nb3	2d	1/3	2/3	0.87545(74)	0.16667
	O1	6i	0.17214(116)	0.82786(116)	0.30799(46)	0.50
	O2	6i	0.16375(92)	0.83615(92)	0.57010(49)	0.50
	O3	6i	0.16731(117)	0.83259(117)	0.93445(58)	0.50
	O4	6i	0.49493(118)	0.50497(118)	0.18831(31)	0.50
			$a = b = 5.80701(6)$ (Å), $c = 18.94654(29)$ (Å)			
			Overall B-factor = 0.156 (Å^2)			

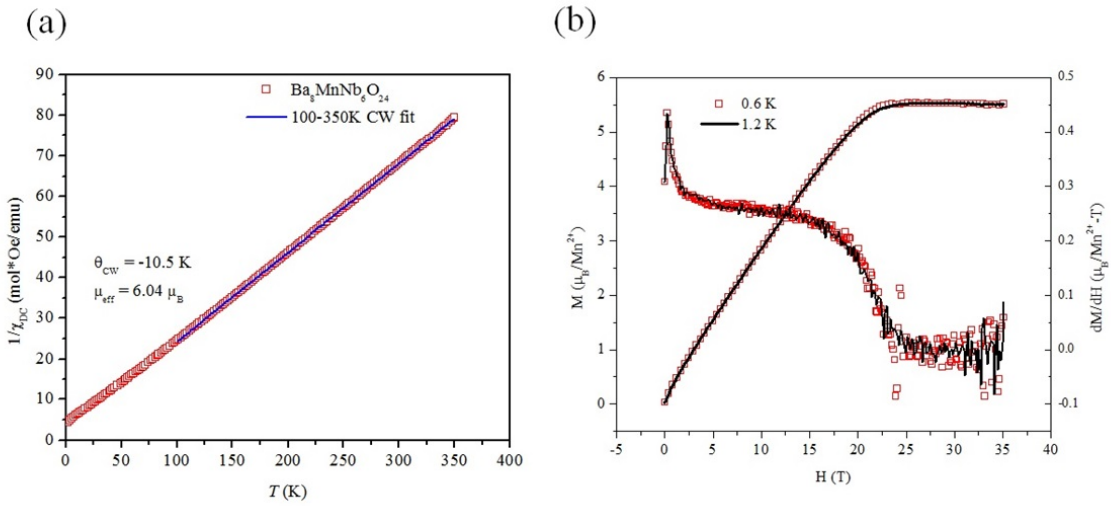

Figure 4.17: (a) DC susceptibility at a field of 0.5 T and Curie-Weiss linear fitting from 100 - 350 K. (b) High field magnetization up to 35 T showing a saturation of moments at $\sim$22T and saturation moment of 5.60 $\mu_{\mathrm{B}}/\mathrm{Mn}^{2+}$.

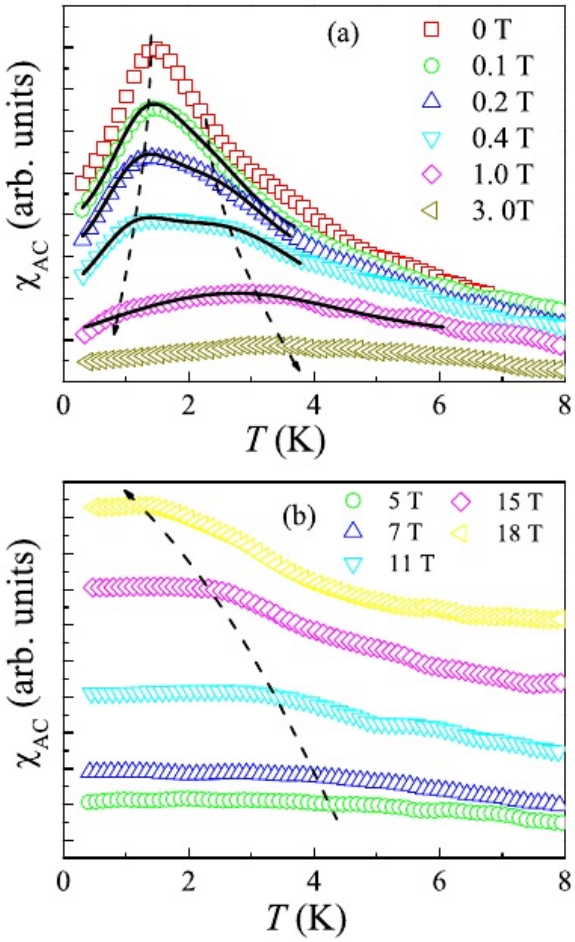

Figure 4.18: AC susceptibility for $Ba_8MnNb_6O_{24}$ under (a) low fields from zero to 3.0 T and (b) high fields of 5.0 - 18.0 T. Fitting of the susceptibility with two Gaussian peaks is shown with each peak defining a transition temperature. Lines provided to guide the eye.

has a sharp peak at 1.45 K that is indicative of magnetic LRO. Small DC applied magnetic field ($\sim$ 0.1 T) causes the peak to broaden such that it can be resolved by two Gaussian peaks. This shows a splitting of the single step transition at zero field into two transitions, at T_{N1} and at higher temperature T_{N2}. Upon increasing the applied DC field, the transition temperatures diverge with T_{N1} shifting to lower temperatures while T_{N2} shifts to higher temperatures, shown by the dashed arrows in Figure 4.18 (a). Upon increasing the applied field to 3.0 T and beyond, the low-temperature transition is no longer visible. This is most likely due to being shifted below 0.3 K, the lower limit of our AC susceptibility measurements. For applied fields larger than 3.0 T, T_{N2} reverses the previous trend and actually shifts to lower temperatures with further increases in DC field. A magnetic phase diagram has been presented in Figure 4.19 (a) for $Ba_8MnNb_6O_{24}$, constructed from the DC saturation field and the transition temperatures obtained from χ_{AC}.

Figure 4.20 presents the specific heat data of $Ba_8MnNb_6O_{24}$. C_p measurements were taken at zero field, 7 T, and 14 T. At zero field, there is a broad peak in C_p but no noticeable feature around $T_N = 1.45$ K where a peak is observed in χ_{AC}. There is also a sharp increase in C_p below 200 mK, likely due to the nuclear Schottky anomaly arising from the Nb ions. Upon increasing applied fields, there is a suppression of the broad peak. Magnetic contribution, C_m, to specific heat was isolated, as in Subsection 4.2.1, by subtracting an lattice contribution measured from non-magnetic $Ba_8ZnTa_6O_{24}$. The change in magnetic entropy, ΔS_m, was again calculated by integrating C_m/T with a lower bound of 200 mK to avoid the nuclear Schottky anomaly contribution. The small magnitude of C_p by 200 mK indicates the low-temperature contribution would be small. For AFM transition with S-1/2 ions, the expected ΔS_m is given by Rln(6) = 14.9 J/mol-K, where R is the gas constant. The obtained value from the data for all fields is $\sim$16 J/mol-K, a comparable value. The small discrepancy may be from the contribution of the nuclear Schottky anomaly persisting above 200 mK. The magnetic entropy releases at high temperature as 20 K, far above the zero field transition temperature of $T_N = 1.45$ K.

NPD taken at HB-2A is presented in Figure 4.21 and was measured at 0.3 K using a wavelength of $\lambda = 2.4127$ Å. Rietveld refinement of the magnetic Bragg reflections shows these reflections occur at at $Q = (n_1 + 1/3, n_2 + 1/3, n_3)$ where n_i: integer. The magnetic

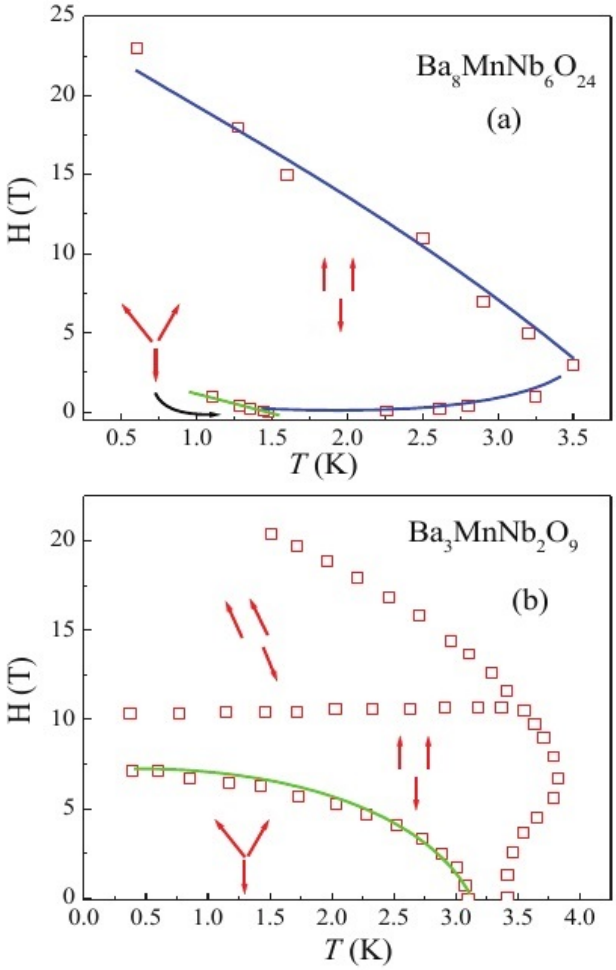

Figure 4.19: The magnetic phase diagram for (a) $Ba_8MnNb_6O_{24}$ and (b) $Ba_3MnNb_2O_9$ from Ref. [22] provided for comparison. The phases of $Ba_3MnNb_2O_9$ are represented as the canted 120 degree, *uud*, and oblique phases.

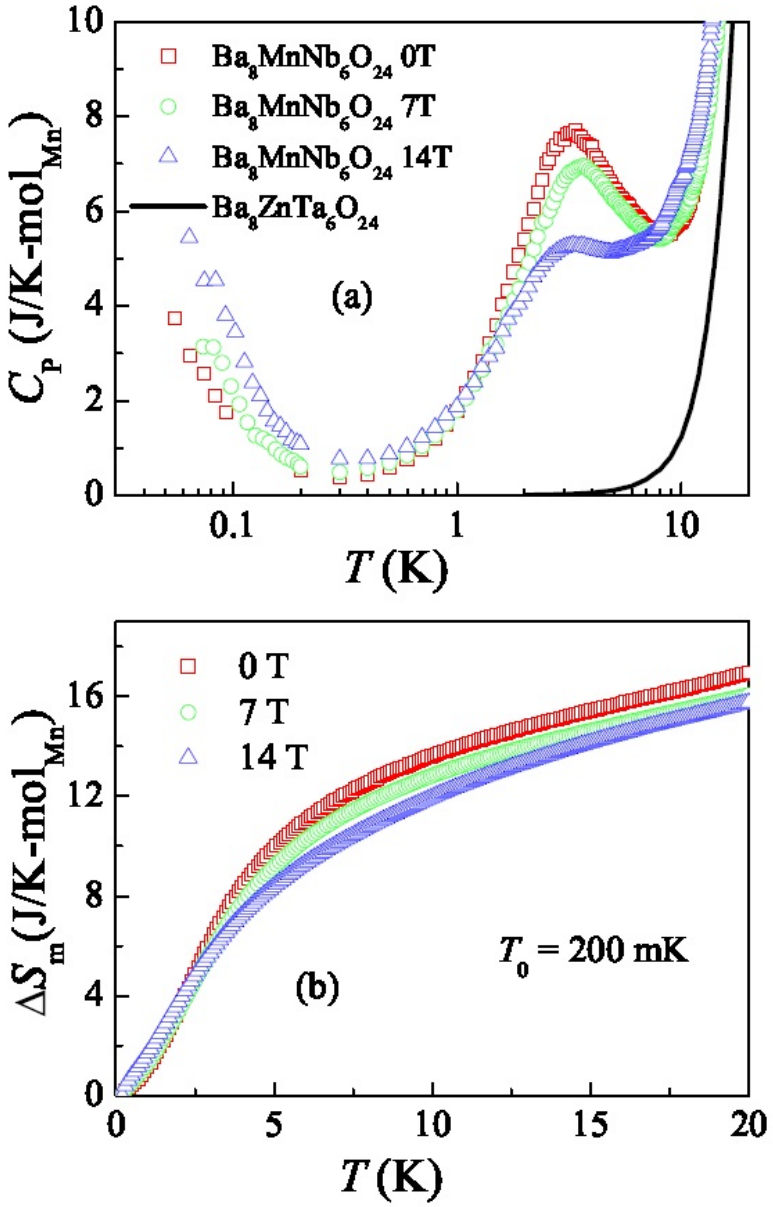

Figure 4.20: (a) Specific heat data of $Ba_8MnNb_6O_{24}$ under zero field, 7 T, and 14 T (red, green, and blue respectively) and $Ba_8ZnTa_6O_{24}$ (black line) for lattice contribution. (b) Magnetic entropy calculated from integral of C_p/T with the lattice contribution subtracted starting from 200 mK.

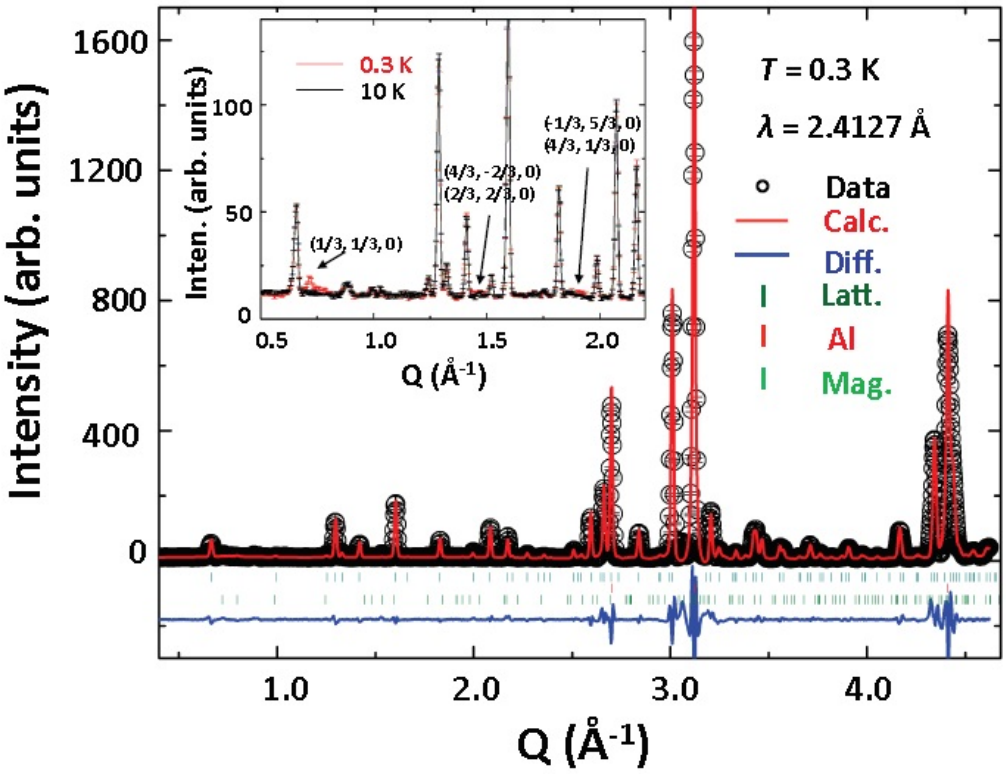

Figure 4.21: The Rietveld refinement of the neutron powder diffraction pattern measured at $T = 0.3$ K with $\lambda = 2.4127$ Å of $Ba_8MnNb_6O_{24}$. Black circles are the measured intensity, the red line is the calculated intensity, and the blue line is the difference. Bragg reflections are indicated by tick marks and coincide with the lattice, aluminum, and magnetic contributions from top to bottom. Inset: The difference between diffraction patterns at 0.3 and 10 K is highlighted to show the magnetic Bragg peak positions.

Bragg peaks are shown in more detail in the insert of Figure 4.21, where the magnetic contribution has been isolated by subtracting the 10.0 K pattern from the 0.3 K pattern. The refined magnetic structure is of the 120 degree structure (Figure 1.4) with the ordering in the *ab*-plane that has been observed in the other AFM members of the triangular lattices described in this Section. Adjacent layers show collinear FM ordering. The refined moment for each Mn^{2+} ion is 4.6(1) μ_B, smaller than the saturation moment of 5.5 μ_B from DC magnetization. Due to resolution limitations and exacerbated by the powder nature of the sample, the Rietveld refinement cannot distinguish between a 120 degree structure with the spins confined to the *ab*-plane or if there is canting of the moments along the *c*-axis, as would be expected for easy-axis anisotropy. Due to the presence of only a single zero-field magnetic transition, as revealed by χ_{AC}, we ascribe the anisotropy present in $Ba_8MnNb_6O_{24}$ to be easy-plane.

Inelastic neutron scattering for $Ba_8MnNb_6O_{24}$ was performed at 10 K, 4.0 K, 1.5 K, 0.4 K and 0.05 K, Figure 4.22 (a-e), respectively. The powder-averaged scattering intensity as a function of both momentum transfer Q and energy transfer E allows for an examination of the magnetic correlations upon lowering temperature, as carried out on $Ba_8CoNb_6O_{24}$. Even at the relatively high temperatures of 10 and 4.0 K, some broad features in the Q dependence of the magnetic signal have already started to form. These features, primarily located around $Q \approx 0.7$ Å^{-1}, suggest short-ranged spin correlations have already developed well above the long-range ordering temperature of T_N. Cooling down to $T = 1.5$ K, strong ridges of intensity emerge at $Q \approx 0.7$ Å^{-1} with further, but less intense, repetitions at 1.5 Å^{-1} and 2.0 Å^{-1}. The E dependence of scattering intensity reveals gapless excitations that extend up to 1.0 meV. Further decrease in temperature to 0.4 K and 0.05 K show no significant change in any of the features, confirming the onset of LRO around 1.5 K.

4.3.1 Discussion

Luwei Ge performed the modeling presented here to examine the dynamic magnetic correlations of the ordered state. For the large, classical spins of Mn^{2+}, linear spin-wave theory is used at $T = 0$ [105]. Here we stay with the nearest-neighbor Heisenberg AFM Hamiltonian of $\mathcal{H} = 1/2J\sum_{<i,j>} S_i \cdot S_j$ and the established 120 degree structure. Exchange

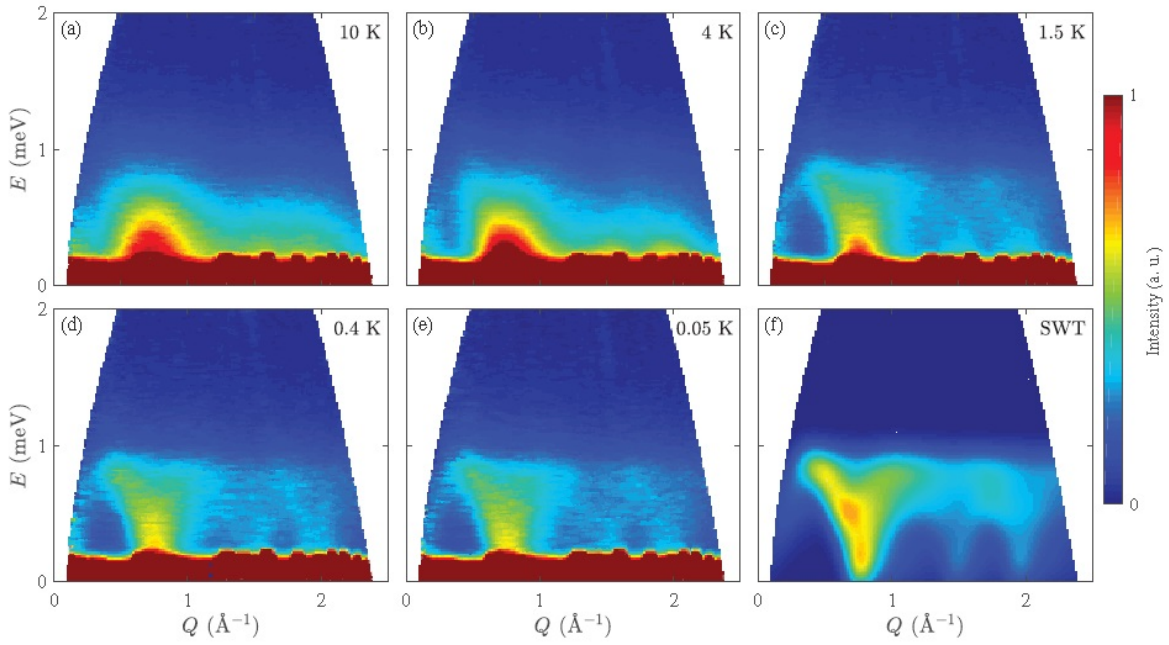

Figure 4.22: (a-e) The powder averaged inelastic neutron scattering spectra of $Ba_8MnNb_6O_{24}$ measured at 10 K, 4 K, 1.5 K, 0.4 K, and 0.05 K, respectively. (f) The neutron scattering intensity calculated for $J = 0.11$ meV using linear spin wave theory.

anisotropy is not considered here due to the powder averaging, as a contribution would be relatively small and cannot be accurately extracted from the INS data. As there is no indication for strong anisotropy, we stay with the isotropic model as in with $Ba_8CoNb_6O_{24}$. The best match between the INS spectrum measured at $T = 0.05$ K and the simulation was found using a nearest-neighbor exchange interaction of $J = 0.11$ meV (or 1.28 K), as shown in Figure 4.22 (e),(f). This value is consistent with the exchange interaction strength calculated from the Curie-Weiss temperature above, $J = 1.22$ K. The calculated spectrum, Figure 4.22 (f), reproduces the main features seen in the experimental data. Both the zone centers and bandwidths are properly reproduced. To further investigate Q-dependent features, the experimental and simulated data is shown in Figure 4.23 (a) and E-dependence is further investigated in the Q-integrated (Figure 4.23 (b)) cuts.

As noted previously, there is no feature in C_p that is indicative of LRO. However, there is a broad peak center around 4 K. As discussed in Section 4.2, small interlayer exchange interactions down to $J'/J = 2\times10^{-4}$ produce a sharp peak in C_p coinciding with the onset of LRO [99]. Further reduction of the interlayer exchange interaction resulted in the disappearance of the sharp peak in C_p leaving only the broad peak, similar to what is seen in the experimental data. This is strong confirmation of the practically ideal 2D nature of the magnetism in $Ba_8MnNb_6O_{24}$. This is a second case of reduction of the interlayer interactions by intercalating non-magnetic and vacant layers between the magnetic layers, also shown in $Ba_8CoNb_6O_{24}$. The broad peak at 4 K could indicate the onset of short ranged correlations above the onset of LRO. The INS spectra showed the onset of broad magnetic signals as high as 10 K, supporting the formation of short ranged correlations above T_N. The suppression of the broad peak under applied field is supportive of this, as applied fields polarize the short-ranged spins.

Despite the successful suppression of the interlayer interaction in $Ba_8MnNb_6O_{24}$ via materials engineering, there is still LRO into the 120 degree phase at an appreciable temperature of $T_N = 1.45$ K. This was confirmed by both χ_{AC} and NPD measurements. The logarithmic relation between T_N and either interlayer interaction or in the exchange anisotropy [4, 5, 6, 7, 8] indicates the likely presence of small anisotropy, as C_p shows no indication for interlayer interactions. For TLAFs possessing anisotropy, a two-stepped

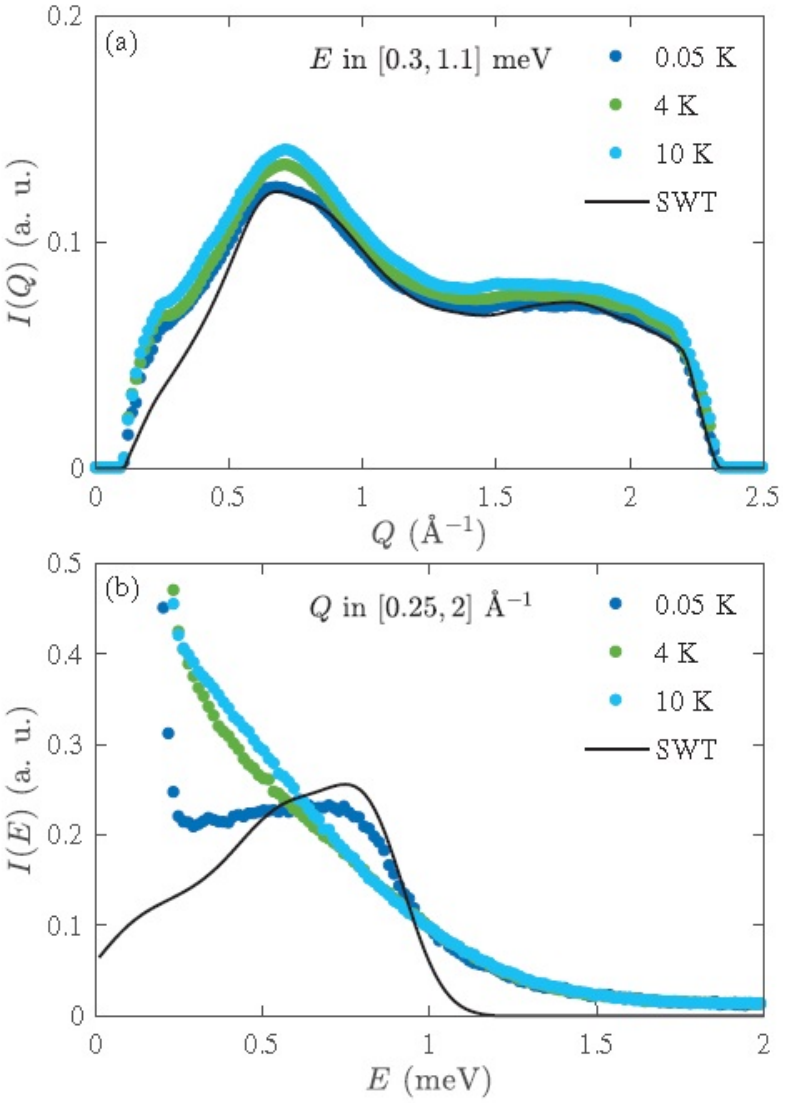

Figure 4.23: Comparisons between experiment (dots)and linear spin wave theory (black line) for $Ba_8MnNb_6O_{24}$ as energy-integrated ($0.3 \leq E \leq 1.1$ meV) and momentum-integrated ($0.25 \leq Q \leq 2$Å^{-1}) cuts, respectively.

transition is predicted for easy-axis anisotropy while a single-stepped transition is predicted for easy-plane anisotropy. Thus we attribute the anisotropy to be of the easy-plane nature.

To further explore the implications for the practically ideal 2D nature of $Ba_8MnNb_6O_{24}$, we compare to the quasi-2D compound of $Ba_3MnNb_2O_9$. To facilitate the discussion, the magnetic phase diagram of $Ba_3MnNb_2O_9$ as reported in Reference [22] is replotted in Figure 4.19 (b). There are three primary differences between the magnetic phase diagram. First, in $Ba_8MnNb_6O_{24}$ there is only a single-stepped instead of two-stepped transition at zero field. Secondly, there is no indication of the *uud* phase in $Ba_8MnNb_6O_{24}$. Thirdly, $Ba_8MnNb_6O_{24}$ evolves from the canted 120 degree structure at much lower fields than in $Ba_3MnNb_2O_9$.

For the zero field case, there is a two-stepped transition in $Ba_3MnNb_2O_9$ with $T_{N1} = 3.0$ K and $T_{N2} = 3.4$ K. This is indicative of the easy-axis anisotropy present that is the usual case for Mn^{2+} ions in an octahedral environment, as seen in other compounds such as $Rb_4Mn(MoO_4)_3$ [107]. However, this is not present in $Ba_8MnNb_6O_{24}$. For special cases, Mn^{2+} ions can display easy-plane anisotropy such as in $Ba_2La_2MnW_2O_{12}$ (see Subsection 4.1.3), which also possesses only a single-stepped transition. In that case, the competition between AFM Mn-O-O-Mn and FM Mn-O-W-O-Mn is a possible cause for this peculiar behavior. The main difference in $Ba_8MnNb_6O_{24}$ from $Ba_3MnNb_2O_9$ is the reduction of dimensionality and this may be the driving force behind the change in anisotropy. For the lack of evidence for *uud* phase, the exact nature of which requires further examination. While it is expected for the classical spins to not show a magnetization plateau at 1/3 magnetization in the *uud* phase, there is such a phase in $Ba_3MnNb_2O_9$. Whether this is due to reduced dimensionality or not is tricky, as the powder nature of the samples cannot be ignored as the powder average can sometimes smear phase boundaries. Single crystal studies are needed to determine if this is an intrinsic effect from reduced dimensionality or extrinsic from the polycrystalline nature. Additionally, we comment on the low magnetic field value at the boundary of the canted 120 degree in $Ba_8MnNb_6O_{24}$ compared to $Ba_3MnNb_2O_9$. At 1.0 K, a field of 1 T is sufficient to drive $Ba_8MnNb_6O_{24}$ out of the canted 120 degree phase while a field of 6 T is required to do the same in $Ba_3MnNb_2O_9$. This can be attributed to the reduced strength in nearest-neighbor exchange interaction J. The calculated $J = 1.22$ K for $Ba_8MnNb_6O_{24}$ from Curie-Weiss temperature is around 43.5% of the $J = 2.8$ K for $Ba_3MnNb_2O_9$.

Finally, we examine the effect of the increased spin of $S = 5/2$ in $Ba_8MnNb_6O_{24}$ from $S = 1/2$ in $Ba_8CoNb_6O_{24}$ and the reduction of the impact of quantum fluctuations. The two obvious differences are the onset of LRO in $Ba_8MnNb_6O_{24}$ observed at $T_N = 1.45$ K and the lack of high energy continuum in the INS spectrum. The lack of LRO in $Ba_8CoNb_6O_{24}$ is attributed to the strong quantum fluctuations and their role in the reduction of the spin anisotropy to approach a true 2D Heisenberg antiferromagnet. This results in only short-ranged magnetic ground state. The lack of high energy continuum shows a reduction in two-magnon scattering. The possible easy-plane anisotropy present in $Ba_8MnNb_6O_{24}$ is sufficient to drive the LRO seen in $Ba_8MnNb_6O_{24}$.

4.4 Discussion

The 2D triangular lattice magnets with close-packed perovskite stacking have shown the ability to host a multitude of magnetic ground states that can be examined via processes such as changing spin size, applying chemical pressure, and reducing dimensionality. For Co- and Ni-containing compounds of the $A_4B'B_2O_{12}$, the competition between the FM superexchange path along Co/Ni-O-W/Re-O-Co/Ni is sufficient to overcome the AFM superexchange path along Co/Ni-O-O-Co/Ni. This results in the onset of FM behavior in the Co compounds and an FM long-range ordered ground state in the Ni compound. For increasing the spin size to Mn in the $A_4B'B_2O_{12}$ family, the ground state becomes AFM in the 120 degree structure and is attributed to the AFM superexchange interaction exceeding the FM superexchange interaction. The Cu containing member shows no evidence for LRO, but further studies are required to reveal the nature of this lack of ordering and possible spin liquid behavior. Chemical pressure applied on the Co-containing members did not provide any simple relation, but the onset of FM behavior did shift in a non-trivial way under the application of chemical pressure.

Reduction of dimensionality for the S-1/2 Co triangular lattice via $Ba_8CoNb_6O_{24}$ suppresses the onset of LRO down below 60 mK. This is the realization of a practically ideal 2D isotropic Heisenberg TLM and allows for the exploration of the role of the strong quantum fluctuations in the dynamic magnetic correlations. This is useful in examining the need for

additional theoretical models such as SWT with $1/S$ correction as LSWT is insufficient to describe the two-magnon scattering observed in this material. The increased spin of S-5/2 coinciding with the reduction in dimensionality is realized in $Ba_8MnNb_6O_{24}$. The interlayer exchange interaction is suppressed to the zero limit, but weak easy-plane anisotropy is still sufficient to induce LRO into the 120 degree ground state. We have successfully demonstrated the strong effects from quasi-2D behavior and quantum fluctuations in low-spin frustrated systems.

Chapter 5

3d-Transition Metal Pnictide Double Helical Magnetic Structures

Determination of magnetic structures is ideally suited for neutron diffraction measurements as discussed in Chapter 2. One family of interest that would benefit from an in-depth study involving neutron scattering is the family of FeP, MnP, and CoP. These members are isostructural 3d-transition metal pnictides (3dTMPs) with MnP attracting the most previous research due to the presence of a superconducting phase under applied pressure [108]. MnP possesses two magnetic transitions, a high-temperature transition into an FM phase and a low-temperature transition into a double helical magnetic ground state. FeP has been previously studied by neutron diffraction and Mössbauer spectroscopy with differing results. A neutron diffraction experiment by Felcher et al. [109] revealed a double helical magnetic structure with two distinct sized magnetic moments while a Mössbauer study undertaken by Häggström and Narayanasamy proposes a bunched helical structure with possible modulation along the *ab* plane [36]. The magnetic ground state of CoP has not been previously reported. Thus, we examined the family of $Fe_{1-x}Mn_xP$ using a combination of neutron diffraction, χ_{DC}, and resistivity to explore the magnetic phases of this family of 3dTMPs. The results in this chapter are in pre-publication and I would like to acknowledge the contributions by Clarina dela Cruz, Qing Huang, Keith Taddei, Huibo Cao, Haidong Zhou, and Randy S. Fishman.

5.1 FeP, MnP, and CoP

Compounds of the manganese monophosphide (MnP) structure, Figure 5.1 (a), (belonging to the *Pnma* space group) have long attracted interest for their magnetic properties. MnP exhibits a ground state with a double helical magnetic structure [37, 110], where the spins rotate about the c axis over a period of 5 unit cells. The ground state of iron monophosphide (FeP) is a similar magnetic structure [109], however with different phase angles [109, 111]. Susceptibility measurements on single crystal samples show that FeP has one antiferromagnetic (AFM) transition at 119 K while MnP shows both an AFM transition at 62 K and a ferromagnetic (FM) transition at 296 K. Below the AFM transition, both FeP and MnP adopt a double helical structure with phase angles of 169° [109] and 16° [37, 110], respectively.

Double helical spin structures have often manifested large magneto-elastic coupling, with structural distortions in CrAs and MnAs [112] and novel pressure induced phases, including superconducting, in MnP [108]. However, there has not been any reported evidence for such strong coupling in FeP, nor is there any reported evidence for a structural distortion. Differing magnetic behaviors above the transition temperature are seen between these compounds, with CrAs being paramagnetic [38], MnP being ferromagnetic [37], and FeP being paramagnetic [109].

5.1.1 Single Crystal Diffraction

Single crystal neutron diffraction on FeP reveals a single domain crystal. Refinement of the nuclear peak intensities confirms that the crystal is of the space group *Pnma*. For refinement of magnetic peaks as performed by Felcher *et al.* [109], the Fe atoms were split into pairs of equivalent sites 1 and 3 and pairs of equivalent sites 2 and 4 (Figure 5.1 (a)). In this approach, equivalent sites were refined together, with the real and imaginary parts of the magnetic moment and the real and imaginary phase angles being refined. Sites 2 and 4 were allowed to rotate from sites 1 and 3. X-ray diffraction was used to examine the temperature dependence of the lattice constants. Results show an increase along the

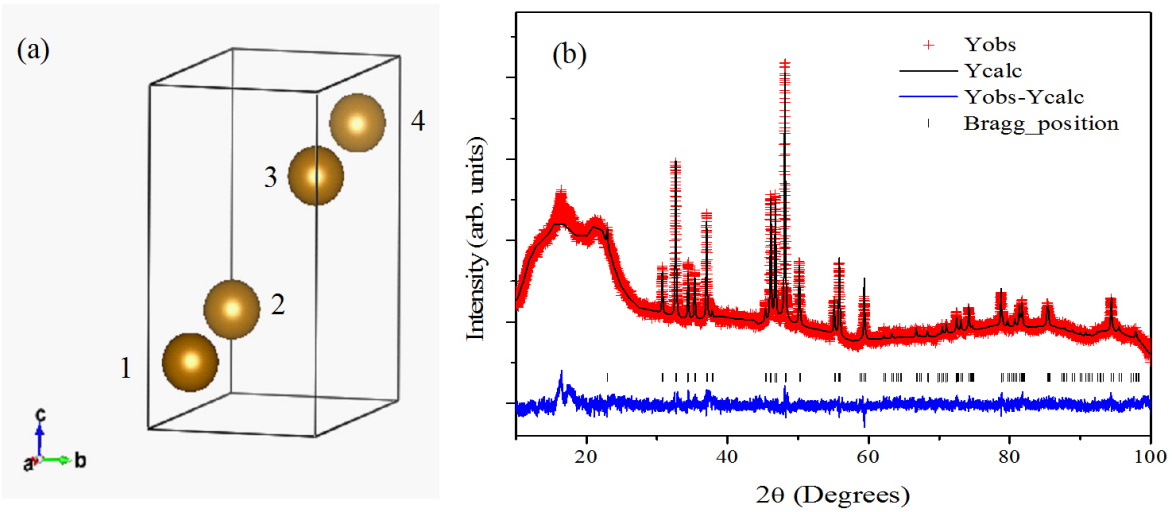

Figure 5.1: a) Crystalline structure of metal atoms of FeP, MnP, and CoP with the space group *Pnma*. Metal atoms are labeled for magnetic description. b) Rietveld refinement of single crystal FeP to show pure phase.

c parameter upon cooling below 125 K (Figure 5.2). This is evidence for the presence of magneto-elastic coupling in FeP.

Refinement of the magnetic peaks did not provide satisfactory fits using a simple double helical structure in the ab plane as proposed by Felcher et al. [109]. A Mössbauer study undertaken by Häggström and Narayanasamy proposes a bunched helical structure with possible modulation along the ab plane [36]. Our refinement provided a best fit using a modified elliptical helix with elongation along the b-axis and a maximum magnetic moment of 0.717 μ_B and a minimum of 0.245 μ_B, fitting results shown in Figure 5.3. Using separate magnetic moments for the differing Fe sites did not improve the fitting. The phase angle between adjacent Fe spins from site one to two is 173°, in near agreement with 168.8° from Felcher *et al.'s* neutron study. Our results did not indicate any bunching along the a axis, such as the presence of Bragg reflection of the third satellites, as reported by Häggström and Narayanasamy. Variations on the simple double-helical structure are shown in Figure 5.4.

The order parameter scan of the [0, 0, 4] peak is presented in Figure 5.5. It shows no nuclear contribution above 120 K, and below T_N shows a smooth increase without fully saturating down to 6 K. This confirms the onset of AFM LRO as only magnetic contributions are seen at [0, 0, 4]. The smooth nature of the order parameter indicates a second-order transition.

5.1.2 DC Susceptibility and Resistivity

DC susceptibility (χ_{DC}) measurements using an applied field of 1000 Oe, shown in Figure 5.6, upon a single crystal show a kink at 119 K both parallel and perpendicular to the a axis, but there is an additional feature at 61 K in χ_{DC} along the a axis. Resistance R measurements performed on single crystal FeP is presented in Figure 5.7 and shows a kink in R at 120 K.

χ_{DC} reveals different behavior along the a axis and bc plane. Along the bc-plane, there is one kink coinciding with the FM transition at 119 K. Along the a axis, there is a kink at 119 K as well as another feature at 59 K. The transition temperature coincides with a peak in $d\chi_{DC}/dT$, while the extra feature along the a axis is seen as a minimum in $d\chi_{DC}/dT$.

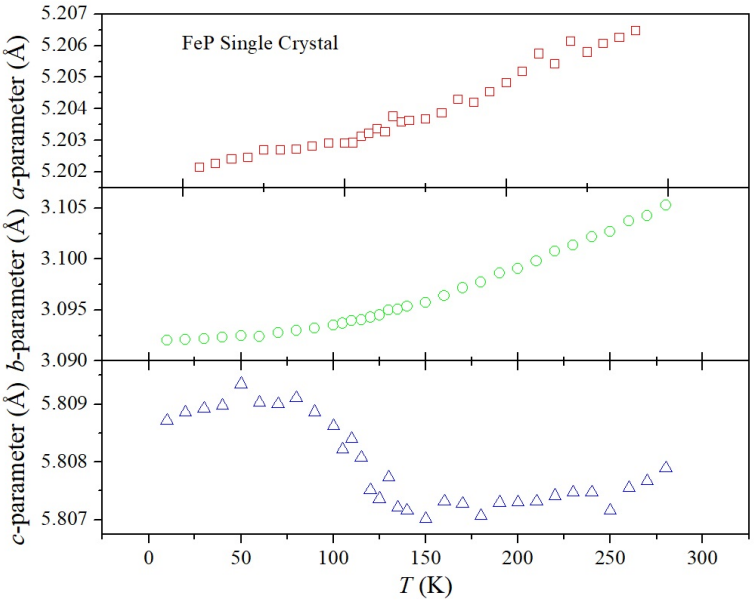

Figure 5.2: Temperature dependence of lattice parameters for single crystal FeP. There is a smooth decrease in the a and b parameters while there is an increase in the c parameter below 125 K. This increase in the c parameter is attributed to magneto-elastic coupling.

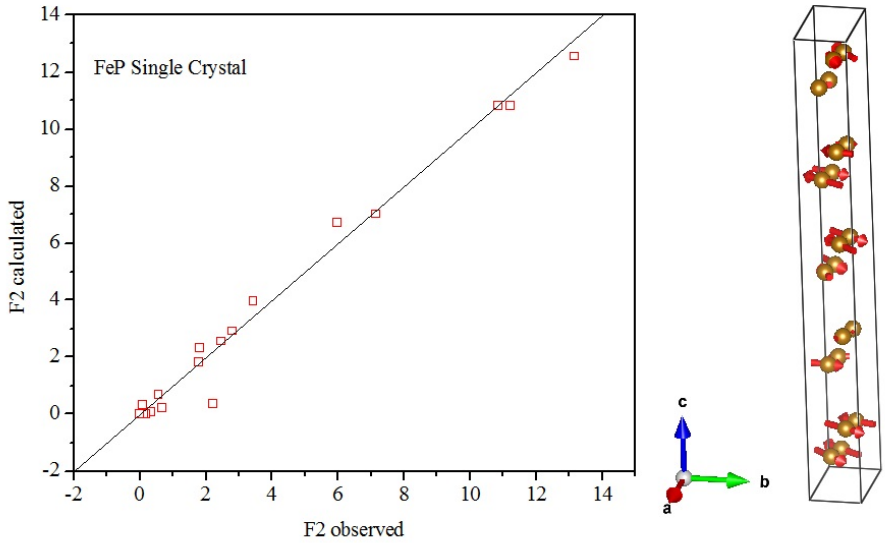

Figure 5.3: Fitting of our magnetic refinement using a non-collinear spin density wave structure in the *ab* plane. Maximum magnetic moments are 0.717 μ_B and minimum magnetic moments are 0.245 μ_B. The phase angle between adjacent (Sites 1 and 2 or 3 and 4) is 173°. The magnetic structure is plotted on the right and occurs over 5 nuclear cells.

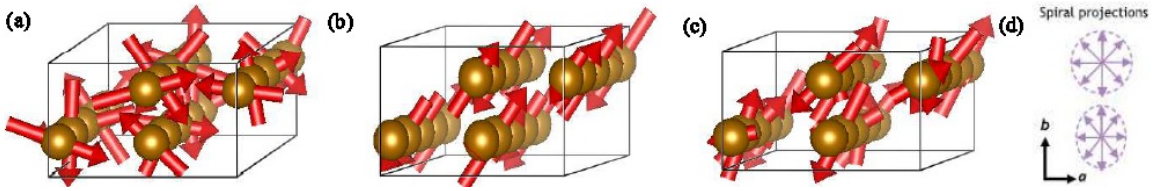

Figure 5.4: (a) Helical model with separate magnetic moments, as used by Felcher et al [109], fit to single crystal diffraction data with the moments confined to the ab plane and the propagation vector is k-vector of (0, 0, 0.2). One full magnetic cell (five nuclear unit cells) are displayed to show periodicity. (b) Linear spin density wave model fit to single crystal neutron scattering data. (c) Nonlinear spin density wave used to fit single crystal neutron diffraction, similar to the structure found in FeAs [39] using polarized neutrons. This provides the quantitatively and qualitatively best fit of our data. The maximum magnetic moment is $0.72\pm0.1\mu_B$ and the minimum moment is $0.245\pm0.06\mu_B$. The phase angle between adjacent (Sites 1 and 2 or 3 and 4) ions is 173°. (d) Projection of magnetic moments on the ab plane for both helical and non-collinear spin density wave magnetic structures.

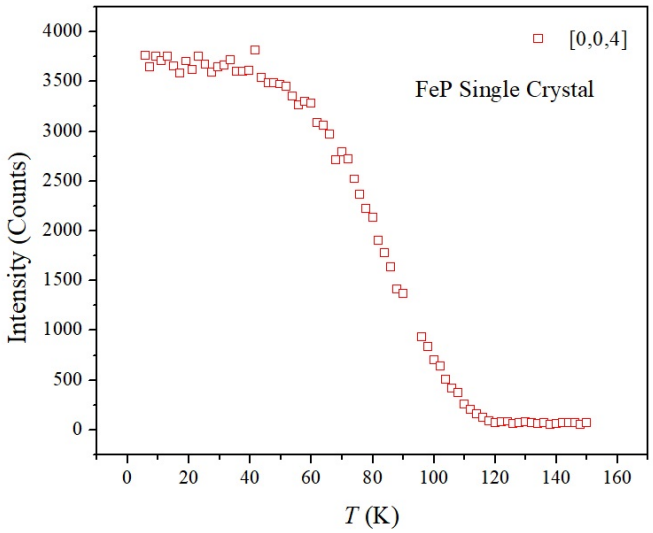

Figure 5.5: Order parameter scan of the [0, 0, 4] peak showing no nuclear contribution and a second order phase change below $T_{\mathrm{N}} = 119$ K.

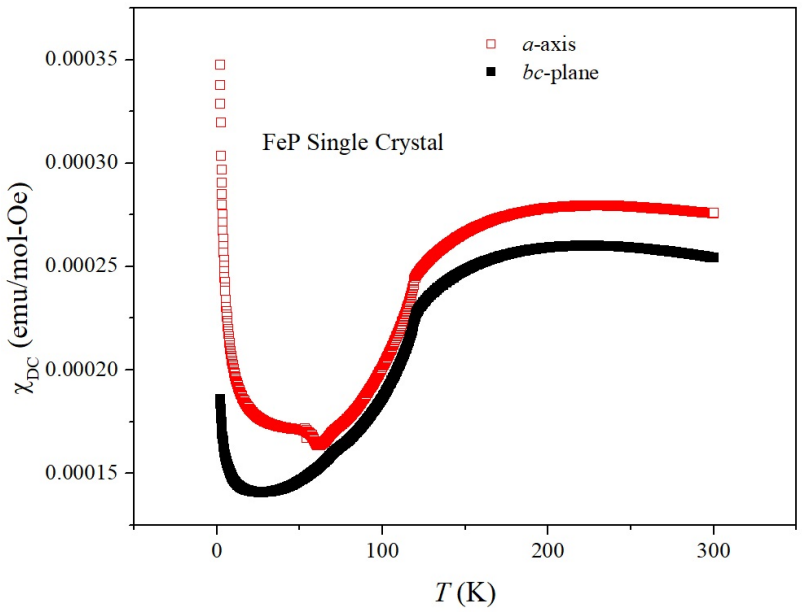

Figure 5.6: DC Susceptibility χ_{DC} for SC FeP along the a axis (red open boxes) and bc plane (black filled boxes). Both show a kink at $T_{\mathrm{N}} = 119$ K and χ_{DC} along the a axis also shows an additional feature at $T = 59$ K due to the presence of oxygen trapped in the sample.

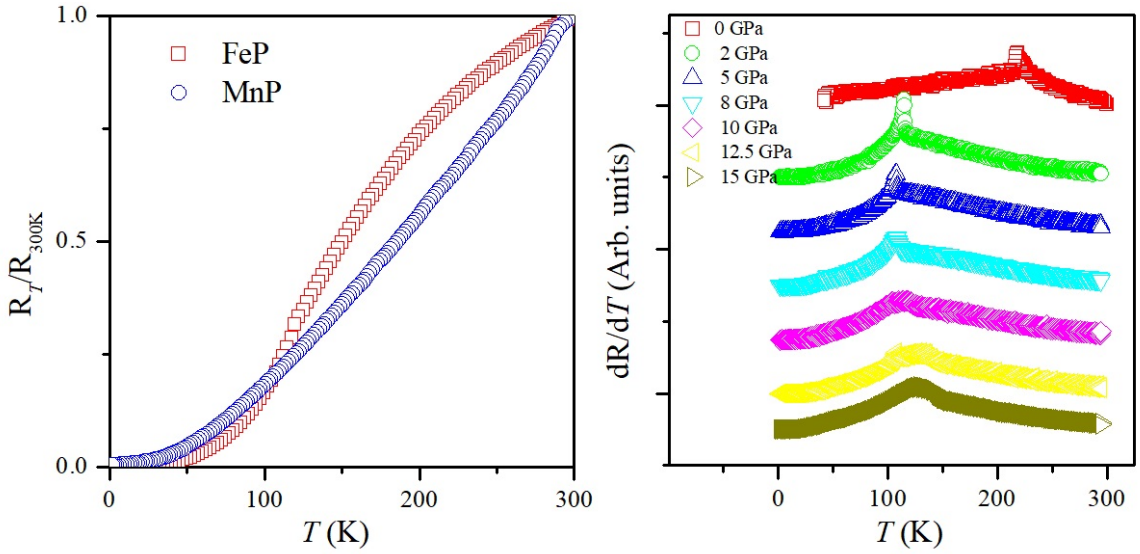

Figure 5.7: (a) Resistance of FeP and MnP single crystal samples, scaled to the resistance at $T = 300$K. (b) Derivative of resistance of FeP single crystal under varying pressures. Data sets are offset vertically for clarity.

The extra feature is attributed to the presence of trapped oxygen and has been noted in other measurements using the same instrument. Resistance R also shows a kink at 120 K, coinciding with the feature in χ_{DC}. Both of these features coincide with T_{N} and the onset of AFM order.

5.2 $Fe_{1-x}Mn_xP$

As discussed in Section 5.1, there is magneto-elastic coupling found in many double helical spin structure materials such as structural distortions in CrAs and MnAs [112] and the pressure induced superconducting phase in MnP [108]. With evidence for the presence of magneto-elastic coupling seen in the increase in c axis parameter upon lowering temperature below 125 K as seen in Figure 5.2. Following up on this, it is natural to examine the evolution of the magnetic structure between FeP and MnP using chemical pressure, creating the $Fe_{1-x}Mn_xP$ family. The radius of the magnetic ions will provide the chemical pressure between the isostructural end members, with the larger Mn^{2+} possessing the appropriately larger lattice constants. The evolution of the magnetic structure between FeP and MnP has not been previously investigated. Here, we look to examine the disappearance of the FM transition seen in MnP, as well as the evolution of the double helical magnetic ground state seen in both FeP and MnP.

5.2.1 X-ray Diffraction

XRD of the complete family of $Fe_{1-x}Mn_xP$ at room temperature shows single phase of the spacegroup $Pnma$ for all samples. Polycrystalline FeP has lattice parameters of $a = 5.1888(6)$ Å, $b = 3.0976(5)$ Å, and $c = 5.7888(6)$ Å with increasing parameters under doping to MnP with $a = 5.2543(4)$ Å, $b = 3.1702(3)$ Å, and $c = 5.9147(5)$ Å (Figure 5.8). No structural distortions are apparent. Lattice parameters are reported in Table 5.1. Refinements using two separate phases for FeP and MnP mixing did not improve the fittings. This further supports a single phase sample.

XRD measurements of the family of $Fe_{1-x}Mn_xP$ shows a smooth, nearly linear expansion of lattice parameters upon increasing x values (Figure 5.8). All refinements showing a single

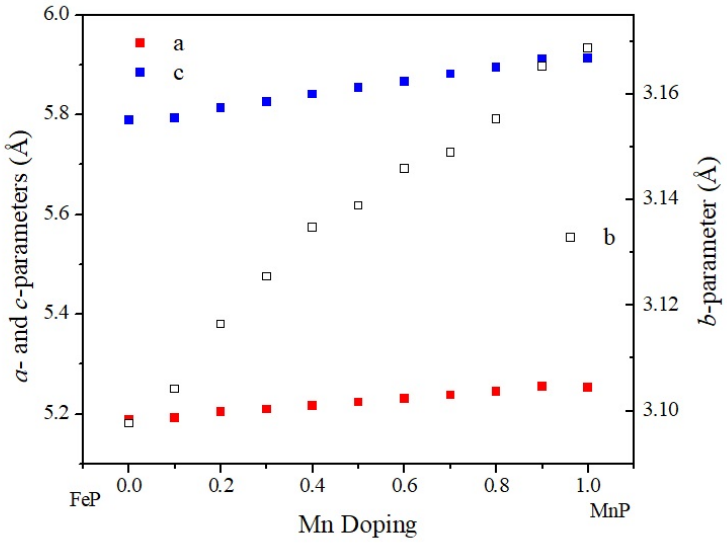

Figure 5.8: Lattice parameters of $Fe_{1-x}Mn_xP$ as a function of x. Upon replacing Fe with Mn, there is a smooth increase in all lattice parameters. This reinforces that all samples are isostructural with minimal impurities.

Table 5.1: Lattice parameters for polycrystalline $Fe_{1-x}Mn_xP$ at room temperature (space group *R-3mH*) determined from refined XRD measurements.

Composition	χ^2	a (Å)	b (Å)	c (Å)
FeP	2.66	5.18884(19)	3.09763(13)	5.78883(23)
$Fe_{0.9}Mn_{0.1}P$	1.17	5.19129(22)	3.10407(16)	5.79358(27)
$Fe_{0.8}Mn_{0.2}P$	1.85	5.20441(17)	3.11642(12)	5.81374(20)
$Fe_{0.7}Mn_{0.3}P$	4.19	5.20912(32)	3.12538(22)	5.82594(37)
$Fe_{0.6}Mn_{0.4}P$	1.64	5.21633(19)	3.13471(14)	5.84078(23)
$Fe_{0.5}Mn_{0.5}P$	4.99	5.22322(29)	3.13890(21)	5.85388(35)
$Fe_{0.4}Mn_{0.6}P$	1.93	5.22962(15)	3.14581(11)	5.86684(18)
$Fe_{0.3}Mn_{0.7}P$	7.32	5.23743(29)	3.14890(22)	5.88139(36)
$Fe_{0.2}Mn_{0.8}P$	4.14	5.24408(23)	3.15525(17)	5.89466(28)
$Fe_{0.1}Mn_{0.9}P$	1.30	5.25529(16)	3.16527(12)	5.91157(20)
MnP	9.34	5.25227(27)	3.16875(18)	5.91271(31)

phase of spacegroup *Pnma* and the smooth increase in lattice parameters on increasing x indicate that the doping does not produce any structural anomalies and that all members of the family are isostructural. This indicates that the doping provides chemical pressure that may affect the ground state.

5.2.2 DC Susceptibility and Resistivity

Resistivity (ρ) measurements were performed on all doped members of $Fe_{1-x}Mn_xP$ using pressed pellets cut into slabs of $3 \times 8 \times 1$ mm and are shown in Figure 5.9. While the magnitude of the resistivity is not easily described by doping concentration, all samples show at least one kink in ρ. χ_{DC} was performed on each sample and is reported in Figure 5.9. The magnitude of χ_{DC} increases significantly with Mn doping x. Two transitions are clearly apparent in MnP while only one is present in FeP. Further examination of the transitions under doping is covered below in Subsection 5.2.4.

Resistivity measurements were performed on all doped members of $Fe_{1-x}Mn_xP$. The magnitude of ρ under doping does not follow a simple pattern but is smallest for $Fe_{0.6}Mn_{0.4}P$ and largest for $Fe_{0.7}Mn_{0.3}P$. Each sample shows at least one kink in ρ that is sharp for large x and smooths out for smaller x. There is also a flattening of the resistivity at low temperatures for all samples, with some showing a minor increase at very low temperatures. This feature is inherent in the samples, and not related to the magnetic ordering.

The DC susceptibility measurements, shown in Figure 5.10 reveal one clear transition for FeP and two clear transitions for MnP. The first derivative $d\chi_{DC}/dT$ shows a sharp local maximum at the AFM transition for both FeP and MnP and a sharp local minimum at the FM transition of MnP. The sharp local maximum present in FeP continues up to $x = 0.9$, generally increasing in temperature with Mn doping. The low-temperature maximum from MnP decreases in both magnitude and temperature with lowering x and disappears for $x < 0.7$. The high-temperature local minimum from MnP is also present in $x = 0.9$ but disappears for $x \leq 0.8$. An additional local minimum occurs at $x = 0.9$ and survives down to $x = 0.5$. Whether this indicates another transition remains to be resolved with neutron studies. Additionally, there is a local maximum in $d\chi_{DC}/dT$ for $x = 0.5$ that is not

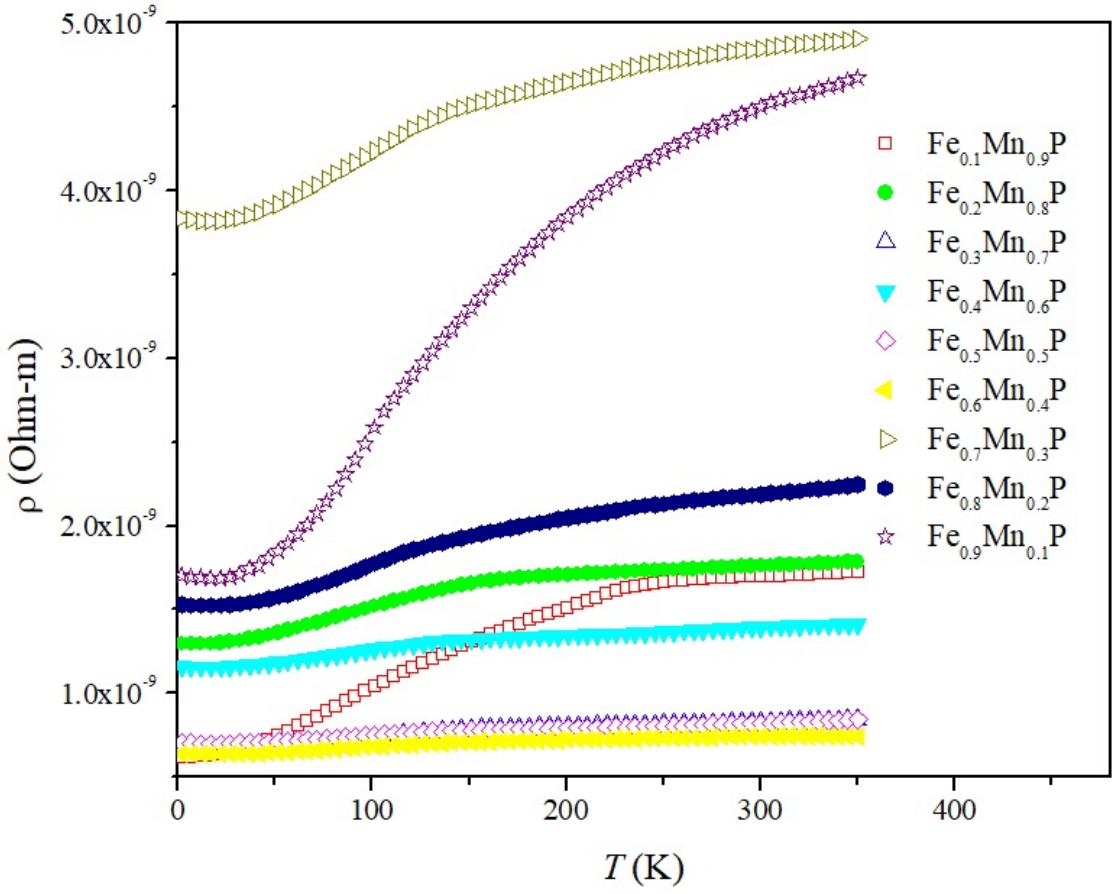

Figure 5.9: Resisitivity ρ of $Fe_{1-x}Mn_xP$. The magnitude is not controlled simply by doping x. Each sample shows one kink in ρ indicative of a magnetic transition.

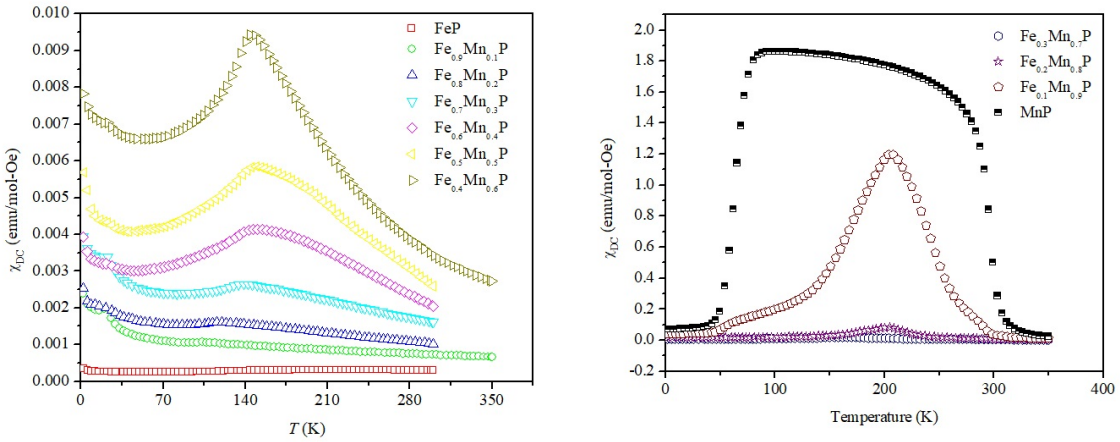

Figure 5.10: χ_{DC} measurements of $\mathrm{Fe}_{1-x}\mathrm{Mn}_x\mathrm{P}$ measured at 1000 Oe. The magnitude of χ_{DC} increases with increasing x.

attributed to either the FeP or MnP transition. Whether this indicates multiple steps in the ordering remains to be resolved.

5.2.3 Neutron Powder Diffraction

Neutron powder diffraction was measured on $Fe_{0.1}Mn_{0.9}P$ at temperatures of 5, 30, 100, 200, 270, and 300 K, reported in Figure 5.11. The difference in the diffraction patterns of 270 and 300 K reveals FM ordering of $Fe_{0.1}Mn_{0.9}P$, while the difference between 200 and 270K reveals FM ordering along differing peaks of $Fe_{0.1}Mn_{0.9}P$. Upon further cooling to 100 K, incommensurate AFM LRO develops centered at $2\theta = 2.45°$. Cooling to 30 K is accompanied by an increase in intensity in the incommensurate peak and the increased is centered on $2\theta = 2.35°$ as well as the development of another incommensurate peak centered at $2\theta = 3.20°$. Cooling to 5K reveals increases in the incommensurate signal centered at $2\theta = 2.75°$ and $3.55°$ as well as a distinct magnetic Bragg peak at $2\theta = 23.9°$. This reveals a complicated ordering process involving both FM and AFM transitions as seen in MnP, as well as further ordering steps not present in either end member. There are two separate incommensurate magnetic peaks that develop in $Fe_{0.1}Mn_{0.9}P$ with one centered near $2\theta = 2.6$ that develops upon cooling to 100 K, while further cooling below 50 K reveals another peak centered at $2\theta = 3.3$. The presence of two independent incommensurate peaks is consistent with a double helical model, with the onset of each helix occurring at a distinct temperature. More detailed neutron diffraction measurements have recently been taken at HB-2A on samples of $Fe_{0.2}Mn_{0.8}P$ and $Fe_{0.3}Mn_{0.7}P$. The data is still being analyzed, but there is a single k-vector AFM transition seen in $Fe_{0.2}Mn_{0.8}P$ under cooling while there is a similar two k-vector magnetic structure seen in $Fe_{0.3}Mn_{0.7}P$ as $Fe_{0.1}Mn_{0.9}P$. The lack of a second k-vector in $Fe_{0.2}Mn_{0.8}P$ is possibly due to the high k-vector occurring at $k \sim (0, 0, 0.11)$ so a lower ordering occurring at lower q-space (as seen in the other powder samples) may be outside of the q-range of HB-2A. The powder nature of the samples measured here cannot be discounted, as there is no multiple k-vector ordering reported in single crystal samples of MnP. Modeling this complex ordering behavior with doping is beyond the scope of my work and is something to be examined more thoroughly in the future. Smaller doping

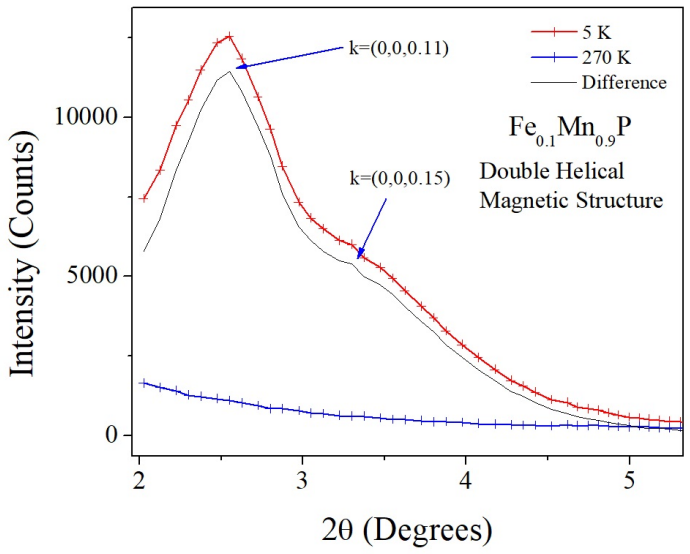

Figure 5.11: Neutron powder diffraction for $Fe_{0.1}Mn_{0.9}P$ taken at 5 and 270K. The difference shows LRO under cooling, indicating the feature in $d\chi_{DC}/dT$ indeed indicates AFM ordering. The incommensurate nature of the ordering is apparent from the extremely low Q values of the magnetic peaks.

steps are imperative to provide a more detailed description of magnetic behavior that would allow for a more nuanced conversation about the ordering processes.

5.2.4 Magnetic Phase Diagram

Using resistivity and χ_{DC} measurements, we propose a phase diagram for $Fe_{1-x}Mn_xP$. The kinks in ρ and local maxima and minima in $d\chi_{\mathrm{DC}}/dT$ are used to define boundary temperatures, as shown in Figure 5.12 (a). For FeP single crystal (Figure 5.7 (b)) and MnP single crystal resistance, the kinks in resistance coincide with the onset of AFM and FM long-range ordering, respectively. In χ_{DC}, for both SC FeP and MnP there is a sharp maximum in $d\chi_{\mathrm{DC}}/dT$ at the onset of AFM ordering while in MnP there is also a sharp minimum at the onset of AFM ordering. The overlap of transition temperatures found in ρ and χ_{DC} further supports the validity of the transition temperatures in the doped samples. For samples with $x \leq 0.8$, the kink in ρ coincides with a sharp peak in $d\chi_{\mathrm{DC}}/dT$ associated with the FeP AFM ordering. For $x = 0.9$, the kink in resistivity moves up to a local minima in $d\chi_{\mathrm{DC}}/dT$. However, these local minima appear lower in temperature and in addition to the MnP FM ordering transition. The results are summarized in Figure 5.12 (b). The complex nature of the magnetic phase diagram with high Mn doping points towards an accordingly complex model. The evolution of the singular k-vector, double helical AFM transition in FeP appears to split into separate helices with distinct k-vectors at high Mn doping. However, there is no evidence for this second k-vector helix in single crystal measurements. As a result, the polycrystalline nature of the sample needs examination. The exact disappearance of the FM transition seen in MnP also remains unclear. Further neutron diffraction measurements with smaller doping steps are needed to address these remaining challenges.

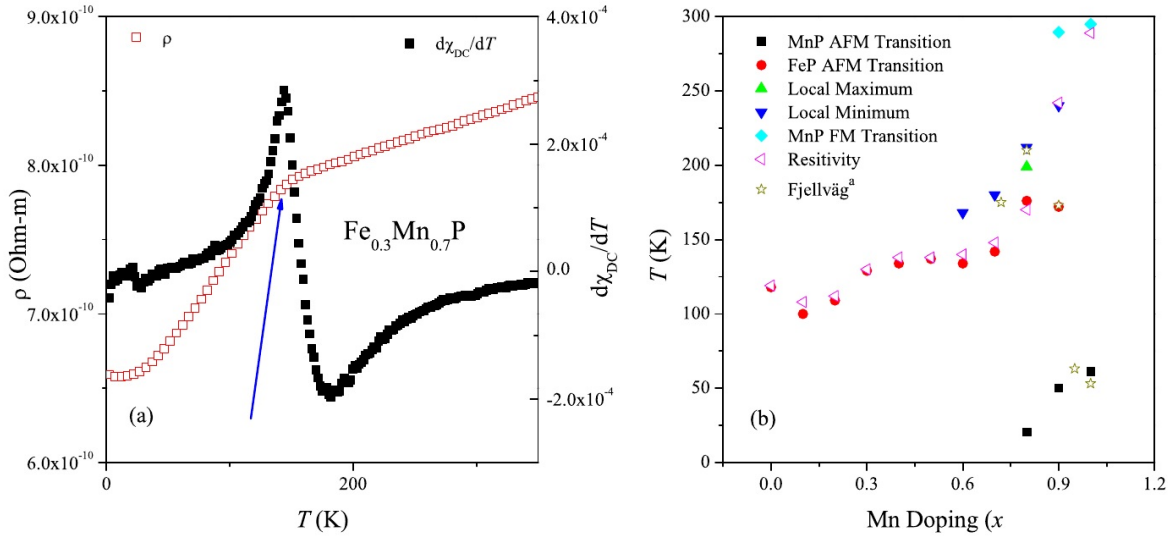

Figure 5.12: (a) Resistivity ρ and $d\chi_{\mathrm{DC}}/dT$ of $Fe_{0.3}Mn_{0.7}P$ to show transitions. Transitions are determined by kinks in ρ (arrow) and sharp local maxima and minima of $d\chi_{\mathrm{DC}}/dT$. (b) Magnetic phase diagram of $Fe_{1-x}Mn_xP$ determined from resistivity and $d\chi_{\mathrm{DC}}/dT$.

Chapter 6

Conclusion and Outlook

This dissertation focused on the material engineering of non-collinear magnetic structures. Neutron scattering techniques were used to reveal the magnetic ground structures of geometrically frustrated triangular magnets and 3d-transition metal pnictide double helical structures. Neutron scattering is an essential part of condensed matter physics due to their unique properties and availability of extreme sample environments. Results revealed by neutron scattering include a transition to an FM ground state in frustrated triangular systems induced by manipulating the spin size, reduction of interplane interactions by intercalation of non-magnetic layers, true-2D behavior in $Ba_8CoNb_6O_{24}$, a non-collinear spin density wave or bunched helical structure in SC FeP, and mutltiple k-vector ordering in doped double helical structure compounds.

An extensive look at geometrically frustrated triangular magnets of $Sr_4CoRe_2O_{12}$, $Sr_2La_2CoW_2O_{12}$, $Ba_2La_2CoW_2O_{12}$, $Ba_3LaCoReWO_{12}$, $Ba_4CoRe_2O_{12}$, $Ba_2La_2NiW_2O_{12}$, $Ba_2La_2MnW_2O_{12}$, $Ba_3CoNb_2O_6$, and $Ba_8CoNb_6O_{24}$ was carried out to examine the effects of spin size, chemical pressure, and interlayer interactions on the magnetic ground states. Comparison of $Ba_8CoNb_6O_{24}$ to $Ba_3CoNb_2O_6$ reasserts the role in interlayer interactions in stabilizing the 120 degree coplanar structure. By reducing to the interplane interactions to negligible values by introduction of four additional non magnetic and one vacant layer between each triangular layer of magnetic ions, $Ba_8CoNb_6O_{24}$ shows no ordering down to 60 mK and instead obeys an isotropic Heisenberg Hamiltonian. Comparison of the members of the $A_4B'B_2O_{12}$ family show that spin size plays an integral role in magnetic ground state.

Spin-3/2 compound $Ba_2La_2MnW_2O_{12}$ orders into the 120deg ground state while spin-1 $Ba_2La_2NiW_2O_{12}$ shows long ranged FM order and spin-1/2 cobalt containing members show FM behavior. Further neutron scattering to provide more precise atomic positions of the oxygen ions would provide superexchange pathway angles that may also modify the ground state.

The double helical magnetic structures of the 3d-transition metal pnictides FeP, MnP, CoP, and the family $Fe_{1-x}Mn_xP$ were thoroughly examined using neutron scattering and supplementary techniques. The double helical structure was shown to be robust under chemical substitution, but the ordering process evolved in a complex manner. MnP shows a single FM and single AFM transition, but under small Fe doping ($x = 0.8$, 0.9) shows a two-stepped AFM transition with an additional FM transition for $x = 0.9$. This extra AFM transition step corresponds to a distinct k-vector indicating that the two helixes have different periodicities. This complex behavior is similar to what is seen in axial-next-nearest-neighbor-Ising models and further study is required to determine the driving interactions of this unique ordering.

Looking forward, there is much that can be done both experimentally and theoretically to expand upon the research contained in this dissertation. From a materials synthesis side, triangular lattice magnets with tunable spin sizes and chemical pressure provide ideal frameworks for tuning near the quantum critical point. The crossover from AFM transitions at high spin to FM transitions at low spin indicate a proximity to such a critical point. Additionally, tuning of interlayer strengths by intercalating with nonmagnetic layers holds promise for bulk growths of samples with nearly ideal two-dimensional behaviors. For double helical structures, the presence of superconductivity in MnP crystals under pressure and contracting lattice constants under iron doping may still hold promise. A more thorough examination of doping with smaller step sizes near the suppression of one of the k-vectors for AFM ordering may reveal quantum criticality. Theoretically, the ideal isotropic Heisenberg Hamiltonian behavior of $Ba_8CoNb_6O_{24}$ revealed the need for nonlinear spin wave terms to describe the magnetic excitations. Further experimental data for two-dimensional quantum materials is needed to verify the theoretical modeling and predictions for frustrated systems.

In the double helical structures, much is left to be done to describe the driving interactions of the non-collinear ordering.

Neutron scattering techniques are vital and central to the understanding of new magnetic properties of emergent materials. The materials engineering of non-collinear magnetic structures reveals complex magnetic behavior ideally suited to neutron measurements and opens the opportunity for examining quantum critical points via chemical doping. We hope that this work can provide a basis for further experimentation and theoretical modeling on these promising materials.

Bibliography

[1] A. P. Ramirez, Annu. Rev. Mater. Sci. **24**, 453 (1994). 4

[2] L. Balents, Nature **464**, 199 (2010). 4, 7, 8

[3] J. E. Greedan, J. Mater. Chem. **11**, 37 (2000). 4, 6, 7

[4] K. Hirakawa, J. App. Phys. **53**, 1893 (1982). 4, 64, 78, 91

[5] A. Cuccoli, T. Roscilde, R. Vaia, and P. Werrucchi, Phys. Rev. Lett. **90**, 167205 (2003). 4, 64, 78, 91

[6] S. Miyashita and H. Kawamura, J. Phys. Soc. Jpn. **54**, 3385 (1985). 4, 64, 78, 91

[7] W. Stephan and B. W. Southern, Phys. Rev. B. **61**, 11514 (2000). 4, 64, 78, 91

[8] S. Fujimoto, Phys. Rev. B. **73**, 184401 (2006). 4, 64, 78, 91

[9] H. Tsujii, C. R. Rotundu, T. Ono, H. Tanaka, B. Andraka, K. Ingersent, and Y. Takano, Phys. Rev. B **76**, 060406 (2007). 7, 65

[10] W. -J. Hu, S.-S. Gong, W. Zhu, and D. N. Sheng, Phys. Rev. B **92**, 140403 (2015). 7

[11] P. W. Anderson, Mat. Res. Bul. **8**, 153 (1973). 7

[12] M. F. Collins and O. A. Petrenko, Can. J. Phys. **75**, 605 (1997). 7, 66

[13] A. V. Chubukov and D. I. Golosov, J. Phys.:Condens. Matter **3**, 69 (1991). 7

[14] O. A. Starykh, W. Jin, and A. V. Chubukov, Phys. Rev. Lett. **113**, 087204 (2014). 7

[15] H. D. Zhou, C. Xu, A. M. Hallas, H. J. Silverstein, C. R. Wiebe, I. Umegaki, J. Q. Yan, T. P. Murphy, J. -H. Park, Y. Qiu, J. R. D. Copley, J. S. Gardner, and Y. Takano, Phys. Rev. Lett. **109**, 267206 (2012). 7, 62, 65

[16] T. Susuki, N. Kurita, T. Tanaka, H. Nojiri, A. Matsuo, K. Kindo, and H. Tanaka, Phys. Rev. Lett. **110**, 267201 (2013). 7, 65, 66

[17] G. Quirion, M. Lapointe-Major, M. Poirier, J. A. Quilliam, Z. L. Dun, and H. D. Zhou, Phys. Rev. B **92**, 014414 (2015). 7

[18] G. Koutroulakis, T. Zhou, Y. Kamiya, J. D. Thompson, H. D. Zhou, C. D. Batista, and S. E. Brown, Phys. Rev. B **91**, 024410 (2015). 7, 65

[19] J. Ma, Y. Kamiya, T. Hong, H. B. Cao, G. Ehlers, W. Tian, C. D. Batista, Z. L. Dun, H. D. Zhou, and M. Matsuda, Phys. Rev. Lett. **116**, 087201 (2016). 7, 65, 79

[20] K. Yokota, N. Kurita, and H. Tanaka, Phys. Rev. B **90**, 014403 (2014). 7, 61, 62

[21] J. Hwang, E. S. Choi, F. Ye, C. R. Dela Cruz, Y. Xin, H. D. Zhou, and P. Schlottmann, Phys. Rev. Lett. **109**, 257205 (2012). 7, 62

[22] M. Lee, E. S. Choi, X. Huang, J. Ma, C. R. Dela Cruz, M. Matsuda, W. Tian, Z. L. Dun, S. Dong, and H. D. Zhou, Phys. Rev. B **90**, 224402 (2014). 7, 62, 86, 93

[23] H. Kadowaki, H. Kikuchi, and Y. Ajiro, J. Phys.: Condens. Matter **2**, 4485 (1990). 7

[24] K. Kimura, H. Nakamura, K. Ohgushi, and T. Kimura, Phys. Rev. B **78**, 140401 (2008). 7

[25] M. Kenzelmann, G. Lawes, A. B. Harris, G. Gasparovic, C. Broholm, A. P. Ramirez, G. A. Jorge, M. Jaime, S. Park, Q. Huang, A. Ya. Shapiro, and L. A. Demianets, Phys. Rev. Lett. **98**, 267205 (2007). 7

[26] A. B. Harris, Phys. Rev. B **76**, 054447 (2007). 7

[27] A. Möller, N. E. Amuneke, P. Daniel, B. Lorenz, C. R. dela Cruz, M. Gooch, and P. C. W. Chu, Phys. Rev. B **85**, 214422 (2012). 7, 62

[28] A. A. Tsirlin, A. Möller, B. Lorenz, Y. Skourski, and H. Rosner, Phys. Rev. B **85**, 014401 (2012). 7

[29] T. M. McQueen, P. W. Stephens, Q. Huang, T. Klimczuk, F. Ronning, and R. J. Cava, Phys. Rev. Lett. **101**, 166402 (2008). 10

[30] T. Jia, G. R. Zhang, Z. Zeng, and H. Q. Lin, Phys. Rev. B **80**, 045103 (2009). 10

[31] Y. Li, G. Chen, W. Tong, L. Pi, J. Liu, Z. Yang, X. Wang, and Q. Zhang, Phys. Rev. Lett. **115**, 167203 (2015). 10

[32] Y. Li, H. Liao, Z. Zhang, S. Li, F. Jin, L. Ling, L. Zhang, Y. Zou, L. Pi, Z. Yang, J. Wang, Z. Wu, and Q. Zhang, Scientific Reports **5**, 16419 (2015). 10

[33] Y. Shen, Y. D. Li, H. Wo, Y. Li, S. Shen, B. Pan, Q. Wang, H. C. Walker, P. Steffens, M. Boehm, Y. Hao, D. L. Quintero-Castro, L. W. Harriger, M. D. Frontzek, L. Hao, S. Meng, Q. Zhang, G. Chen, and J. Zhao, Nature **540**, 559 (2016). 10

[34] J. A. M. Paddison, M. Daum, Z. Dun, G. Ehlers, Y. Liu, M. B. Stone, H. D. Zhou, and M. Mourigal, Nature Physics **13**, 117 (2016). 10

[35] K. Motizuki, H. Ido, T. Itoh, and M. Morifuji, *Electronic Structure and Magnetism of 3d-Transition Metal Pnictides*, (Springer Science+Business Media, LLC, 2010). 10

[36] L. Häggström and A. Narayanasamy, J. Magn. and Magn. Mater. **30**, 249 (1982). 10, 96, 99

[37] G. P. Felcher, J. Appl. Phys. **37**, 1056 (1966). 10, 97

[38] H. Watanabe, N. Kazama, Y. Yamaguchi, and M. Ohashi, J. Appl. Phys. **40**, 1128 (1969). 10, 97

[39] E. E. Rodriguez, C. Stock, K. L. Krycka, C. F. Majkrzak, P. Zajdel, K. Kirshenbaum, N. P. Butch, S. R. Saha, J. Paglione, and M. A. Green, Phys. Rev. B **83**, 134438 (2011). 10, 102

[40] P. Schmidt, M. Binnewies, R. Glaum, and M. Schmidt, in *Advanced Topics on Crystal Growth*, edited by S. O. Ferreira (InTech, 2013), Chap. 9. 13

[41] R. Pynn, in *Neutron Applications in Earth, Energy and Environmental Sciences*, edited by L. Liang et al (Springer Science+Business Media, LLC, 2009), Chap. 2. 16, 18

[42] W. Friedrich, P. Knipping, and M. Laue, *Interferenz-Erscheinungen bei Rntgenstrahlen. Sitzungsberichte der K. Bayerische Akademie der Wissenschaften*, Mathematische-Physikalische Klasse, pp 303322 (1912). 19

[43] Taylor, Jon, O. Arnold, J. Bilheaux, A. Buts, S. Campbell, M. Doucet, N. Draper et al. *Mantid, A high performance framework for reduction and analysis of neutron scattering data*, Bulletin of the American Physical Society **57**, (2012). 20

[44] J. Rodriguez-Carvajal, Physica B **192**, 55 (1993). 20, 22, 24, 35

[45] C. M. Clark and B. L. Dutrow, *Single-crystal X-ray Diffraction*, 2018. *https://serc.carleton.edu/research_education/geochemsheets/techniques/SXD.html*. Accessed: 2018, 04, 08. 21

[46] HB-2A Neutron Powder Diffractometer Fact Sheet. *https://neutrons.ornl.gov/sites/default/files/Instrument_hb2a_0.pdf*. 25

[47] L. W. Finger, D. E. Cox, and A. P. Jephcoat, J. Appl. Cryst. **27**, 892-900 (1994). 26

[48] A. S. Wills, *SARAh- Representational Analysis*, [Software] (1999). 26

[49] C. Broholm, Y. Chen, M. Kenzelmann, C. P. Landee, K. Lefmann, Y. Qiu, D. H. Reich, C. Rischel, M. B. Stone, and M. M. Turnbull, *Spinons, Solitons, and Breathers in Spin-1/2 Chains*, 2004. *https://www.ncnr.nist.gov/AnnualReport/FY2003_html/RH13/*. Accessed: 2012, 02, 07. 30, 31

[50] M. Mourigal, M. Enderle, A. Kl opperpieper, J.-S. Caux, A. Stunault, and H. M. Rønnow, Nature Physics **9**, 435-442 (2013). 32, 64

[51] R. T. Azuah, L. R. Kneller, Y. Qiu, P. L. W. Tregenna-Piggott, C. M. Brown, J. R. D. Copley, and R. M. Dimeo, J. Res. Natl. Inst. Stan. Technol. **114**, 341 (2009). 31

[52] S. Blundell, in *Magnetism in Condensed Matter*, (Oxford University Press, 2014), Chap. 2. 35

[53] N. Elstner, R. R. P. Singh, and A. P. Young, Phys. Rev. Lett. **71**, 1629 (1993). 35, 72, 73

[54] Z. L. Dun, M. Lee, E. S. Choi, A. M. Hallas, C. R. Wiebe, J. S. Gardner, E. Arrighi, R. S. Freitas, A. M. Arevalo-Lopez, J. P. Attfield, H. D. Zhou, and J. G. Cheng, Phys. Rev. B **89**, 064401 (2014). 38

[55] R. Rawl, M. Lee, E. S. Choi, G. Li, K. W. Chen, R. Baumbach, C. R. Dela Cruz, J. Ma, and H. D. Zhou, Phys. Rev. B **95**, 174438 (2017). 41, 43, 46, 47, 48, 50, 51, 52, 54, 55, 57, 60, 63

[56] R. Rawl, L. Ge, H. Agrawal, Y. Kamiya, C. R. Dela Cruz, N. P. Butch, X. F. Sun, M. Lee, E. S. Choi, J. Oitma, C. D. Batista, M. Mourigal, H. D. Zhou, and J. Ma, Phys. Rev. B **95**, 060412(R) (2017). 41, 67, 68, 70, 71, 74, 76

[57] L. Katz and R. Ward, Inorg. Chem. **3**, 205 (1964). 42

[58] A. Maignan, W. Kobayashi, S. Hébert, G. Martinet, D. Pelloquin, N. Bellido, and Ch. Simon, Inorg. Chem. **47**, 8553 (2008). 42

[59] J. M. Longo, L. Katz, and R. Ward, Inorg. Chem. **4**, 235 (1965). 44

[60] H. J. Rother, A. Fadini, and S. Kemmler-Sack, Z. Anorg. Allg. Chem **463**, 137 (1980). 44

[61] S. Kemmler-Sack, Z. Anorg. Allg. Chem **461**, 142 (1980). 44

[62] Z. F. Li, J. L. Sun, L. P. You, Y. X. Wang, and J. H. Lin, J. Alloy. Compd. **379**, 117 (2004). 44

[63] W. Low, Phys. Rev. **109**, 256 (1958). 45

[64] F. Lloret, M. Julve, J. Cano, R. Ruiz-García, and E. Pardo, Inorg. Chim. Acta. **361**, 3432 (2008). 45

[65] P. W. Anderson, Phys. Rev. **79**, 350 (1950). 59

[66] J. B. Goodenough, Phys. Rev. **100**, 564 (1955). 59

[67] J. B. Goodenough, J. Phys. Chem. Solids **6**, 287 (1958). 59

[68] J. Kanamori, J. Phys. Chem. Solids **10**, 87 (1959). 59

[69] M. Lee, J. Hwang, E. S. Choi, J. Ma, C. R. Dela Cruz, M. Zhu, X. Ke, Z. L. Dun, and H. D. Zhou, Phys. Rev. B **89**, 104420 (2014). 62, 65, 69, 71, 79

[70] N. D. Mermin and H. Wagner, Phys. Rev. Lett. **17**, 1133 (1966). 64

[71] E. Lieb, T. Schultz, and D. Mattis, Ann. Phys. **16**, 407466 (1961). 64

[72] L. D. Faddeev and L. A. Takhtajan, Phys. Lett. A **85**, 375377 (1981). 64

[73] D. A. Tennant, T. G. Perring, R. A. Cowley, and S. E. Nagler, Phys. Rev. Lett. **70**, 40034006 (1993). 64

[74] L. Savary and L. Balents, arXiv:1601.03742 (2016). 64

[75] A. Banerjee, C. A. Bridges, J.-Q. Yan, A. A. Aczel, L. Li, M. B. Stone, G. E. Granroth, M. D. Lumsden, Y. Yiu, J. Knolle, S. Bhattacharjee, D. L. Kovrizhin, R. Moessner, D. A. Tennant, D. G. Mandrus, and S. E. Nagler, Nature Materials, doi:10.1038/nmat4604 (2016). 64

[76] Th. Jolicoeur and J. C. Le Guillou, Phys. Rev. B **40**, 2727 (1989). 64

[77] A. V. Chubukov, S. Sachdev, and T. Senthil, J. Phys: Cond. Matt. **6**, 8891 (1994). 64

[78] L. Capriotti, A. E. Trumper, and S. Sorella, Phys. Rev. Lett. **82**, 3899 (1999). 64

[79] W. H. Zheng, J. O. Fjærestad, R. R. P. Singh, R. H. McKenzie,and R. Coldea, Phys. Rev. B **74**, 224420 (2006). 64

[80] S. R. White and A. L. Chernyshev, Phys. Rev. Lett. **99**, 127004 (2007). 64

[81] A. L. Chernyshev and M. E. Zhitomirsky, Phys. Rev. B. **79**, 144416 (2009). 64

[82] R. Coldea, D. A. Tennant, R. A. Cowley, D. F. McMorrow, B. Dorner, and Z. Tylczynski, Phys. Rev. Lett. **79**, 151 (1997). 64

[83] Y. Doi, Y. Hinatsu, and K. Ohoyama, J. Phys. Condens. Matter **16**, 8923 (2004). 64, 65, 66, 79

[84] W.-J. Hu, S.-S. Gong, W. Zhu, and D. N. Sheng, Phys. Rev. B. **92**, 140403 (2015). 65

[85] Y. Shirata, H. Tanaka, A. Matsuo, and K. Kindo, Phys. Rev. Lett. **108**, 057205 (2012). 65

[86] N. A. Fortune, S. T. Hannahs, Y. Toshida, T. E. Sherline, T. Ono, H. Tanaka, and Y. Takano, Phys. Rev. Lett. **102**, 257201 (2009). 65

[87] E. A. Ghioldi, A. Mezio, L. O. Manuel, R. R. P. Singh, J. Oitmaa, and A. E. Trumper, Phys. Rev. B **91**, 134423 (2015). 65

[88] Y. Shirata, H. Tanaka, A. Matsuo, and K. Kindo, Phys. Rev. Lett. **108**, 057205 (2012). 65, 78, 79

[89] T. Susuki, N. Kurita, T. Tanaka, H. Nojiri, A. Matsuo, K. Kindo, and H. Tanaka, Phys. Rev. Lett. **110**, 267201 (2013). 65, 78, 79

[90] H. D. Zhou, Cenke Xu, A. M. Hallas, H. J. Silverstein, C. R. Wiebe, I. Umegaki, J. Q. Yan, T. P. murphy, J. H. Park, Y. Qiu, J. R. Copley, J. S. D. Gardner, and Y. Takano, Phys. Rev. Lett. **109**, 267206 (2012). 65, 78, 79

[91] Y. Shirata, H. Tanaka, T. Ono, A. Matsuo, K. Kindo, and Hiroki Nakano, J. Phys. Soc. Jpn. **80**, 093702 (2011). 65, 79

[92] Y. C. Sun, Z. W. Ouyang, M. Y. Ruan, Y. M. Guo, J. J. Cheng, Z. M. Tian, Z. C. Xia, G. H. Rao, J. Mag. Mag. Mater. **393**, 273 (2015). 65, 79

[93] K. Yokota, N. Kurita, and H. Tanaka, Phys. Rev. B. **90**, 014403 (2014). 65, 79

[94] J. Hwang, E. S. Choi, F. Ye, C. R. Dela Cruz, Y Xin, H. D. Zhou, and P. Schlottmann, Phys. Rev. Lett. **109**, 257205 (2012). 65, 79

[95] M. Lee, E. S. Choi, X. Huang, J. Ma, C. R. Dela Cruz, M. Matsuda, W. Tian, Z. L. Dun, S. Dong, and H. D. Zhou, Phys. Rev. B **90**, 224402(2014). 65, 79

[96] G. Quirion, M. Lapointe-Major, M. Poirier, J. A. Quiliam, Z. L. Dun, and H. D. Zhou, Phys. Rev. B **92**, 014414 (2015). 65

[97] P. Mallinson, M. Allix, J. Claridge, R. Ibberson, D. Iddles, T. Price, and M. Rosseinsky, Andew. Chem Int. Ed. **44**, 7733 (2005). 66, 79, 80

[98] R. Rawl, L. Ge, H. Agrawal, Y. Kamiya, C. R. Dela Cruz, N. P. Butch, X. F. Sun, M. Lee, E. S. Choi, J. Oitma, C. D. Batista, M. Mourigal, H. D. Zhou, and J. Ma, Phys. Rev. B **95**, 060412(R) (2017). [Supplemental material]. 66, 69, 72, 77

[99] P. Sengupta, A. Sandvik, R. Singh, Phys. Rev. B. **68**, 094423 (2003). 69, 73, 91

[100] N. Chandrasekharan and S. Vasudevan, Phys. Rev. B. **54**, 14903 (1996). 72

[101] H. Rosner, R. R. P. Singh, W. H. Zheng, J. Oitmaa, and W. E. Pickett, Phys. Rev. B. **67**, 014416 (2003). 72

[102] R. R. P. Singh and J. Oitmaa, Phys. Rev. B. **85**, 104406 (2012). 72

[103] J. Oitmaa, C. Hamer, and W. Zheng, Series Expansion Methods for Strongly Interacting Lattice Models, (University Press, Cambridge, 2006). 72

[104] M. Mourigal, W.T. Fuhrman, A. L. Chernyshev, and M. E. Zhitomirsky,Physical Review B **88**, 094407 (2013). 75, 76, 78

[105] S. Toth and B. Lake, Journal of Physics: Condensed Matter **27**, 166002 (2015). 75, 89

[106] G. A. Parks, and S. Akhtar, The American Mineralogist **53**, 406 (1968). 80

[107] R. Ishii, S. Tanaka, K. Onuma, Y. Nambu, M. Tokunaga, T. Sakakibara, N. Kawashima, Y. Maeno, C. Broholm, D. P. Gautreaux, J. Y. Chan, and S. Nakatsuji, Europhys. Lett. **94**, 17001 (2011). 93

[108] M. Matsuda, F. Ye, S. E. Dissanayake, J.-G. Cheng, S. Chi, J. Ma, H. D. Zhou, J.-Q. Yan, S. Kasamatsu, O. Sugino, T. Kato, K. Matsubayashi, T. Okada, and Y. Uwatoko, Phys. Rev. B **93**, 100405(R) (2016). 96, 97, 106

[109] G. P. Felcher, F. A. Smith, D. Bellavance, and A. Wold, Phys. Rev. B **3**, 3046 (1971). 96, 97, 99, 102

[110] J. B. Forsyth, S. J. Pickart, and P. J. Brown, Proc. Phys. Soc. **88**, 333 (1966). 97

[111] H. Fjellvåg, A. Kjekshus, and A. F. Andresen, Acta Chem. Scand. **A38**, 711 (1984). 97

[112] V. A. Chrenenko, L. Wee, P. G. McCormick, and R. Street, J. Appl. Phys. **85**, 7833 (1999). 97, 106

Vita

Ryan Rawl grew up in Tennessee and has always had a passion for science and music. He graduated from the University of Tennessee at Chattanooga with a B.S. in Physics and in Secondary Education. Ryan looks to continue to explore the boundaries of science and music in the coming years.